Single-shot quantitative interferometric microscopy for imaging high-speed dynamics

by

Baoliang Ge

Submitted to the Mechanical Engineering Department
in partial fulfillment of the requirements for the degree of

Doctor of Philosophy

at the

MASSACHUSETTS INSTITUTE OF TECHNOLOGY

May 2021

Author .....
Mechanical Engineering Department
May 7, 2021

Certified by .....
Peter T. C. So
Professor
Thesis Supervisor

Accepted by .....
Nicholas G. Hadjiconstantinou
Chairman, Department Committee on Graduate Theses

Single-shot quantitative interferometric microscopy for imaging high-speed dynamics

by

Baoliang Ge

Submitted to the Mechanical Engineering Department
on May 7, 2021, in partial fulfillment of the
requirements for the degree of
Doctor of Philosophy

Abstract

The observations of millisecond, micrometer-scale dynamical events are essential, especially in cell biology investigations, material science studies and the development of next-generation clinical diagnosis methods. For imaging these high-speed dynamics, we need optical microscopy methods having millisecond temporal resolution, submicron spatial resolution and the capability of quantitative imaging. However, current imaging techniques usually either could only offer qualitative imaging, or has low quantitative imaging speed due to the requirement of multiple measurements or scanning. Therefore, high-speed quantitative optical imaging techniques that could provide satisfactory imaging performance for the observations of millisecond, micrometer-scale dynamical events are still highly demanded.

In my PhD work, several single-shot quantitative imaging techniques are proposed based on off-axis interferomertic microscopy, to overcome limitations of current imaging techniques, driven by different specific motivations in biomedical researches and material inspections. Firstly, I presented the novel technique of single-shot quantitative amplitude and phase microscopy, which is motivated by the requirement of fast quantitative imaging of RBCs for the clinical diagnosis and drug screening of many diseases, such as malaria and sickle cell disease. Taking advantage of quantitative interferometric microscopy along with the engineering of the medium's optical properties, we realized the simultaneous measurements of RBCs' morphological, molecular and mechanical properties. The second novel imaging technique is for studying novel aniostropic materials (i.e., lyotropic chromonic liquid crystals (LCLCs)), especially the rheology of them, which needs the fast quantitative mapping of polarization parameters (i.e. retardance and orientation angle) of the light field transmitting through anisotropic materials. The polarization sensitive microscope is combined with off-axis shearing interferometry, realizing the single-shot quantitative imaging of LCLC flow with an imaging speed of over 500 frame per second (fps) for the first time. Finally, deep-learning single-shot optical diffraction tomography (DS-ODT), is proposed that fully exploits the potential of off-axis interferometric microscope, to push the imaging speed of 3D cell imaging. By illuminating the cell with four angles simultaneously,

and using innovative deep learning approach to extract the prior knowledge from a training dataset of $\sim$ 900 NIH/3T3 cells, we realized single-shot 3D cell imaging at a 3D imaging speed of over 10,000 fps, enhancing the throughput of 3D flow cytometer to over 5000 cells per second.
These technology advances open the horizons in which the single-shot quantitative interferometric microscopes could serve as powerful platforms in biological cell characterizations and anisotropic material (liquid crystals) inspections, benefiting from their unprecedented quantitative imaging speed. Furthermore, due to the increasingly needs for studying high-speed dynamics and developing novel microfluidic devices and cell characterizing methods, we can envision these techniques could find an even wider range of applications in biology, material science and clinical diagnosis.

Thesis committee:

- Prof. Peter T.C. So, Chair/Advisor, Professor of Mechanical and Biological Engineering
- Prof. George Barbastathis, Committee member, Professor of Mechanical Engineering
- Prof. Nicholas Fang, Committee member, Professor of Mechanical Engineering

Acknowledgments

Firstly, I would like to appreciate the guidance and help from my adviser, Prof. Peter So, who leads me to the area of biophotonics and offers me essential instructions on my research directions and PhD projects. I learned a lot from Peter's profound knowledge and abundant experience on biophotonics. His influence on me is not only limited to the PhD research projects, but his integrity, dedication and rigorousness also sets up the criteria of my future research, which will affect me in my whole life. Then I am thankful to prof. George Barbastathis, who is my thesis committee member and going to be postdoc adviser, giving me many suggestions about our collaboration project and guiding me to the area of computational imaging. Besides, I also gratitude to prof. Nicholas Fang, who offers me important suggestions on my research.

Beyond my thesis committee members, I also appreciate my collaborators during my PhD life. Firstly I want to thank Prof. Renjie Zhou in CUHK, who was a postdoc of Laser Biomedical Research Center (LBRC). He is not only my collaborator, but also my friend. He gave me detailed and comprehensive guidance when he was in LBRC, including teaching me experimental skills and discussing the conceptual ideas with me. Besides, I also give my gratitude to Dr. Mo Deng from Prof. Barbastathis' lab and Yanping He from Prof. Renjie Zhou's lab for their great efforts and contribution to the deep learning single-shot ODT project. Then I would like to express many thanks to prof. Irmgard Bischofberger, her student Qing Zhang from MIT mechanical engineering department and Prof. Rui Zhang from HKUST for our collaboration project about the studies of DSCG flow with PSIM. This is a wonderful research which could not be accomplished without their efforts.

I thank to all the members in LBRC and So lab for all the support during my doctorate studies. I want to mention some of my seniors, Dr. Vijay Raj Singh, Dr. Sungsam Kang, Dr. Jeon Woong Kang, Dr. Poorya Hosseni, Dr. Di Jin for their sincere help and valuable lessons. Especially Dr. Zahid Yaqoob, thank you for your kind suggestions and substantial help during my pursuing of PhD degree. Our lab

assistants in both centers, Sossy Megerdichian and Christine Brooks, have been very kind and helpful over all these years, thank you and I am going to greatly miss you. Furthermore, I thank to our lab manager at LBRC, Luis Galindo who offers me help pursing experiment instruments and technical support.

I also would like to express my gratitude to MIT, the great university which offers the platform to pursuing knowledge and meeting fantastic people. The experience studying here offered me invaluable treasure which will benefit me in my future life and career. MIT treats students as family members, and the atmosphere here encourages us to pursue our dreams. During the pandemic, MIT community takes careful measures to keep students and staff safe. I would like to thank Mechanical engineering department for the great courses it offered, extending my vision to broader area. I think the most important lesson I learned from here is that we should not constrain ourselves in a specific area, and the exchange of knowledge between different disciplines will give birth to more interesting ideas. Besides, I would like to thank Ms. Leslie Regan in particular, who used to be the administrator in Mechanical engineering department, offerred me substantial help during my studies in MechE department. During my pursuing of PhD degree, I thank to my parents, who constantly give me unconditional love and support. They are always my backup force, encouraging me to pursue my dream. I thank to all my friends who offer me help and kind words when I undergo difficulties during my PhD life. The last but not least, I would like to thank to my fiancee, Dr. Ziling Wu, who company with me and support me all the time. I feel so lucky to meet you and to be with you, and I can never achieve so much without your encouragements and understandings.

Baoliang Ge

April 2021

Contents

List of Figures

List of Tables

Chapter 1

Introduction

This chapter briefly introduces the motivations of my PhD work on developing quantitative, single shot, label-free, imaging methods for studying millisecond dynamical events in cell biology and material inspections. An outline of this thesis will also be presented.

1.1 Imaging of millisecond, micrometer-scale dynamical events

Fast dynamical events are ubiquitous in nature, ranging from rapid transient phenomena, such as chemical reaction and phase transitions, to protein dynamics in living cells [1]. In particular, the dynamical events that happen on millisecond time-scale and micrometer length scales, are of great significance in the investigations of cell biology and material science. For example, in the action potential between human neurons, it takes almost 1 ms for a neuron to fire an impulse and return to rest, while the diameter of the axons is usually at a size of several microns. Neuron action potentials have been intensively investigated with a variety of approaches [2], from which people obtained insightful fundamentals in neural science. Furthermore, many of the dynamics occurring in cell membrane are also happening on similar time and length scales [3, 4]. Importantly, the thermal fluctuations of red blood cells' (RBCs)

membranes are related to the biomechanical parameters (i.e. bending modulus, shear modulus, etc) which could suggest new insights into the etiology of a number of human diseases [3]. For many biotechnology applications, high throughput image cytometry is important, in which the large-scale cell characterization requires resolving cellular structures within a few milliseconds when the specimen is transported by flow through the observation volume [5, 6].

Similar dynamic events are also attracting increasingly attention in the studies of material science. Liquid crystals (LCs), for instance, have a characteristic response time in millisecond level to electrical voltages [7]. Furthermore, as the emergence of novel LCs that could be served as an alternative to traditional isotropic fluids in microfluidic, better understanding of their rheological properties becomes critical [8]. From previous studies, we know that the LC molecules' conformation and orientation will deform under pressure flow in microfluidic channels, forming patterns with feature size in micrometer level [9, 10]. In the meanwhile, the patterns of LC molecules' conformation and orientation also evolve in milliseconds under medium flow rates ($\sim 1\mu l/min$). The quantification of the characteristic length and time of nematic LCs' conformations will reveal more insightful knowledge about LCs' rheology, but are still challenging to achieve.

The measurement and analysis of the aforementioned dynamical events requires a high-speed imaging apparatus with millisecond temporal resolution and the resolving capacity in micrometer. Fluorescence optical microscopy [11] is a conventional choice, however, the limitation of it is also obvious. Photobleaching and phototoxicity are not avoidable in fluorescence microscopy, and sample preparation processes often perturb specimen states, while fluorescence can often offer high molecular specificity [12]. Therefore, developing novel imaging instruments that can provide with high-speed, quantitative and label-free images without much loss in spatial resolution is central for studying fast dynamic events.

1.2 Quantitative label-free imaging

Interferometric (or holographic) microscopy has been developed to be one of the most powerful label-free imaging techniques that can address dynamical events on the millisecond and micrometer scales. This class of methods performs interferometric measurements on microscopic images, which enables quantitative mapping of different intrinsic biomarkers (i.e. phase delay, polarization parameters and refractive index (RI)) and has been shown to be an excellent imaging tool for long-time, large-scale cell analysis [12]. Interferometric microscopy that is typically implemented in wide-field imaging geometry, which can reach higher imaging speed over a large field-of-view. In this section, I briefly introduce the principles underlying the three quantitative label-free imaging techniques that I worked on in this thesis, i.e. quantitative phase imaging (QPI), quantitative polarization imaging, and optical diffraction tomography (ODT).

1.2.1 Quantitative phase imaging (QPI)

Quantitative phase imaging (QPI) [12, 13] is one of the most broadly used label-free imaging tools, for example, it can be applied to the imaging of cell migration [14], cell growth [15], red blood cell dynamics [3, 16] and semiconductor wafer inspection [17], etc. In QPI, the imaging contrast, which is defined as how clearly a subject of interest is distinguished from the background, is provided by the optical path length difference altered by either specimen index distribution or specimen morphology. However, since optical detectors are only responsible to light intensity contrast, weak phase objects like thin cells are nearly invisible in microscopes. In 1930s, Zernike invented a technique capable of imaging phase objects with high contrast without labeling, by adding a $\pi/2$ phase shift to the incident field when imaging weak phase objects. The resultant interference between the scattered field from the object and the background results in an amplitude modulation. This imaging technique is called phase-contrast microscopy. This simple modulation enables the visualization of live, unlabelled cells and other transparent objects in detail. Today, phase microscope is broadly used in

most cell biology laboratories.

However, even if phase contrast microscopy is a powerful tool for imaging live cells and transparent objects, its images are not quantitative. To overcome this shortage, one straightforward approach is combining microscopy and holography (or interferometry), with which we can perform highly sensitive measurements of the thickness and refractive index of biological specimens, much like in metrology [18].

Full-field QPI techniques that can be divided into two major groups. The first group is based on phase shifting geometry, where the full-field QPI can be realized by the combination of temporal phase shifting [19, 20]. The time delay of the reference is controlled, and the corresponding intensity images are recorded and formulated as following:

$$I(x,y) = I_0 + I_1(x,y) + 2\sqrt{I_0 I_1(x,y)}\cos\left[\omega\tau + \phi(x,y)\right], \tag{1.1}$$

where I_0 and I_1 are the intensity maps of the reference field and the object field, ω is the angular frequency of the optical field and τ is the time delay between the two waves. In general, the phase shifting can be controlled at the following values $\omega\tau = 0, \pi/2, \pi, 3\pi/2$, and the phase delay of the sample can be retrieved with the following formula:

$$\phi = arg(I_0 - I_\pi, I_{3\pi/2} - I_\pi) \tag{1.2}$$

The other group of full-field QPI is based on off-axis holography that exploits the spatial modulation rather than temporal modulation to realize phase retrieval [21–23]. Here the intensity on CCD/CMOS cameras can be expressed as:

$$I(x,y) = I_0 + I_1(x,y) + 2\sqrt{I_0 I_1(x,y)}\cos\left[\alpha x + \phi(x,y)\right], \tag{1.3}$$

where I_0 and I_1 are the intensity maps of the reference field and the object field, α is the spatial frequency determined by the off-axis angle θ, and we have the relation $\alpha = 2\pi\sin\theta/\lambda$, where λ is the wavelength of light.The cross-term which contains the phase information can be isolated on Fourier domain. After filtering with a sideband frequency filter, and an inverse Fourier transform, we can extract the cross term and

retrieve the phase map.

One of the advantages of off-axis QPI is that it can realize single-shot quantitative imaging, which allows for high-speed imaging. However, this boost in temporal bandwidth has a trade-off in spatial bandwidth. As a result, both methods are used broadly; the optimal choice depends on the demand of the specific application.

1.2.2 Quantitative polarization imaging

Polarization light microscopes are indispensible tools to image and analyze optically anisotropic materials, without the use of exogenous labeling (dye, fluorescence or stain) or destructive electron microscopes [24]. In biological specimens or liquid crystal materials, the specimen structural anisotropy is often reflected in refractive index anisotropy. This refractive index difference is termed birefringence, that can be readily measured by light. For many birefringent materials, the underlying molecular order often gives the light transmitting through the specimen two orthogonal optical axes, where the refractive index along one axis is different with the refractive index along the other axis and can expressed as following:

$$\delta n = n_{||} - n_{\perp} \tag{1.4}$$

where $n_{||}$ and $n_{\perp}$ are the refractive indices of the two orthogonal optical axes. The two components of the incident light along the two orthogonal optical axes are in-phase when entering the specimen, retarding at different rate due to the existence of birefringence (δn), exiting the specimen out-of-phase. The optical path length difference of the two light components are termed retardance, and can be calculated with the following formula when the path length is l:

$$\Delta = \delta n \cdot l \tag{1.5}$$

In other references [25], we can also use the phase difference to define the retardance $\Delta = (2\pi/\lambda)\delta n \cdot l$.

Another important polarization parameter is the angle between the long axis of the anisotropic molecules or fibers and the pre-determined x axis that usually indicates the orientation of anisotropic molecules or fibers . This angle is termed orientation angle, and denoted by φ. In real polarization imaging, restricted by the diffraction-limit resolution, the measured orientation angle φ is averaged within the diffraction-limit spot in $x-y$ plane and also along z-direction. From the orientation angle φ, we can learn the distributions of the in-plane orientation's distribution of the observed fibers, polymers in biological tissues, or liquid crystal molecules.

Therefore, birefringence (δn), retardance (Δ) and the orientation angle of the slow axis (φ) are the major sources of the contrast of polarization light microscopy. We can also realize the quantitative polarization imaging of these polarization parameters with polarization-sensitive optical apparatus, and the detailed method can be seen in ref. [24] that works by using a pair of cross polarizer and analyzer. However, the mechanical rotation of these optical components are slow and many high numerical aperture optics will cause polarization measurement errors across the field of view.

To overcome the mentioned limitations of traditional polarization light microscopy, R. Oldenbourg proposed a novel quantitative polarization imaging approach, which is termed LC-Polscope [26–28]. LC-polscope is still based on the use of cross-polarizers, however, the specimen is illuminated with nearly circularly polarized light and the traditional compensator is replaced by liquid crystal based universal compensators. The segmented compensator reduces previous polarization imaging artifacts from high numerical aperture optics. The polarization parameter retrieval algorithm is quite similar to the phase-shifting holographic imaging. We alter the voltages applied to the two LC compensators to change the polarization states of the illumination lights, and take the intensity measurements on the CCD or CMOS camera correspondingly. The two LC based compensators are placed at an angle of 45°, and their phase retardance are denoted as α and β, respectively. Then the polarization states of the

illumination angle are set to be the following combinations:

$$\begin{aligned}
\Sigma_0 &= (\alpha = 90^\circ, \beta = 180^\circ), \\
\Sigma_1 &= (\alpha = 90^\circ - \chi, \beta = 180^\circ), \\
\Sigma_2 &= (\alpha = 90^\circ + \chi, \beta = 180^\circ), \\
\Sigma_3 &= (\alpha = 90^\circ, \beta = 180^\circ - \chi), \\
\Sigma_4 &= (\alpha = 90^\circ, \beta = 180^\circ + \chi).
\end{aligned} \tag{1.6}$$

where χ is a swing applied to the two LC retarders, which are quite small. The corresponding intensity measurements are I_0, I_1, I_2, I_3 and I_4, respectively. We firstly define two intermediate results A and B:

$$\begin{aligned}
A &= \frac{I_1 - I_2}{I_1 + I_2 - 2I_0} \tan\frac{\chi}{2}, \\
B &= \frac{I_1 + I_2 - 2I_3}{I_1 + I_2 - 2I_0} \tan\frac{\chi}{2}.
\end{aligned} \tag{1.7}$$

From here we find expression for the retardance Δ and orientation angle φ:

$$\begin{aligned}
&\Delta = arctan[(A^2 + B^2)^{1/2}], if I_1 + I_2 - 2I_0 \leq 0 \\
&\Delta = 180^\circ - arctan[(A^2 + B^2)^{1/2}], if I_1 + I_2 - 2I_0 < 0 \\
&\varphi = \frac{1}{2} arctan\left(\frac{A}{B}\right).
\end{aligned} \tag{1.8}$$

The LC-Polscope has greatly improved the accuracy, sensitivity, and speed of polarization imaging by introducing electro-optical LC universal compensators [24, 26, 28]. These improvements make LC-Polscope a powerful tool for determining the orientation of crystal edges in material characterization [29] and in studying biological processes such as microtubule reorganization during cell mitosis [30, 31]. However, LC-Polscope's imaging speed is still restricted by the requirement of making multiple measurements to reconstruct the retardance and orientation angle maps.

1.2.3 Optical diffraction tomography (ODT)

Even if QPI has been successfully applied to many research areas such as cell biology studies and material inspections, the fact that phase is a product of thickness and average RI can potentially result in inaccurate interpretations of QPI data when imaging complex 3-D objects [12, 32]. For acquiring more accurate morphological information, the imaging technique that can quantitatively reconstruct the 3D structures of specimen is highly desired, which pushed the emergence of depth-resolved [33–35] or tomographic version of QPI [36–38], optical diffraction tomography (ODT). Over the decades, a multitude of ODT techniques have been proposed for 3D imaging of cells by quantitatively mapping their refractive index (RI) distributions. These techniques could be separated into two main groups, the first one is based on depth-scanning scheme, exploiting the low-coherence of illumination light to provide depth resolving [39–41]; the other group is based on angle-scanning scheme, which reconstructs the 3D RI map from multiple projected optical fields [36, 42–45]. For both ODT categories, the 3D imaging could be realized by solving an inverse scattering problem, which is governed by the inhomogeneous Helmholtz equation as following:

$$\nabla^2 U(\mathbf{r},\omega) + n_0^2\beta_0^2 U(\mathbf{r},\omega) = -\beta_0^2\chi(\mathbf{r})U(\mathbf{r},\omega), \tag{1.9}$$

where U is the total optical field that could be interpreted as the sum of the incident and scattered fields, $U = U_0 + U_s$. $\mathbf{r}$ is the spatial coordinate, while ω is the angular frequency of the incident light. n_0 is the background refractive index, and the wave number $\beta_0 = \omega/c$. The scattering potential $\chi = n^2(\mathbf{r}) - n_0^2$ is what we want to solve for the inverse scattering problem for reconstructing the 3-D structure of the sample. Inhomogeneous Helmholtz equation describes the behaviors of optical waves scattered by an object, and the solution of it takes account of both the scattering and diffraction of the optical fields [32, 36, 42, 44].

However, since Eqn. (1.9) is nonlinear, directly retrieving the scattering potential from it is difficult. Thus, it is necessary to make reasonable assumptions and approximations. The first-order Born approximation is the most straightforward one we can

adopt when the scattered field is much weaker than the incident field ($U_s << U_0$). In this case, we can use U_0 to substitute the total U in the right hand side of Eqn. (1.9), and the proper modeling of the incident field U_0 is critical for solving the inverse scattering problem. Since we usually use spatially coherent illumination in ODT, we can assume the incident field is a plane wave, which could be described as:

$$U_0(\mathbf{r}) = A(\omega)e^{i\mathbf{k_i}\cdot\mathbf{r}}, \tag{1.10}$$

where $\mathbf{k_i} = \beta_0 n_0 \hat{\mathbf{k}}_\mathbf{i} = \beta_0 n_0(k_{xi}, k_{yi}, k_{zi})$ is the incident wave vector and $\hat{\mathbf{k}}_\mathbf{i}$ is the direction unit vector with $\mathbf{k_i} = (\hat{k_{xi}}, \hat{k_{yi}}, \hat{k_{zi}})$. $A(\omega)$ is the amplitude of the incident light, which is frequency (wavelength) dependent.

For ODT in depth-scanning scheme, the normal incident light is usually adopted where the incident wave vector could be written as $\mathbf{k_i} = \beta_0 n_0(0, 0, 1)$, while its amplitude $A(\omega)$ is a function of wavelength. Plug this expression of incident light to Eqn. (1.9), then the derived scattering field in Fourier domain can be expressed as:

$$U_s(\mathbf{k}_\perp, z; \omega) = -i\beta_0^2 A(\omega)e^{i\gamma z}\chi(\mathbf{k}_\perp, \gamma - \beta)/2\gamma, \tag{1.11}$$

where A is the spectral amplitude of the incident field; $\gamma = \sqrt{n_0^2\beta_0^2 - k_\perp^2}$ and $\mathbf{k}_\perp = (k_x, k_y)$. After applying 2D inverse Fourier transform, the expression for the solved scattering potential could be written as:

$$\chi(\mathbf{k}_\perp - \beta\mathbf{k}_\perp; k_z)|_{k_z=\gamma-\beta\hat{k_i},\hat{z}} = -\frac{2\gamma}{\beta_0^2(\omega)A(\omega)}e^{-i\gamma z}U_s(\mathbf{k}_\perp, z; \omega), \tag{1.12}$$

where $k_z = \gamma - \beta\hat{k_i}$, $\hat{z} = \sqrt{\omega^2/c^2 - k_\perp^2} - n\omega/c\cos\theta$, and θ is the scattering angle. Usually, in ODT based on depth-scanning, even if the low coherence of the illumination could reduce the speckle noise, the scanning of the sample stage along z-direction is quite time-consuming. Besides, due to the short temporal coherence of the light source, the depth-scanning ODT usually adopts phase-shifting QPI system to realize optical field measurement, such as white-light diffraction tomography [39], or gradient light interference microscopy (GLIM) [40, 41], which also hinders fast imaging.

On the other hand, for angle-scanning ODT, the incident field U_0 could be epi-illuminated, however, its frequency is usually singular for implementing off-axis interferometry [32]. In this case, the incident light could be formularized as $U_0 = e^{i\mathbf{k_i}\cdot\mathbf{r}}$. Plug it back to Eqn. (1.9)and applying first-order Born approximation, the scattered field is solved in the transverse Fourier space for a particular focal plane z:

$$U_s(k_x, k_y; z) = \frac{e^{\pm iqz}}{q}\chi(k_x - k_{xi}, k_y - k_{yi}, \pm q - k_{zi}) \tag{1.13}$$

where $+q$ represents the forward scattered field and $-q$ represents the backward scattered field; k_x and k_y represent the scattered field transverse spatial frequencies; and $q = \sqrt{\beta^2 - k_x^2 - k_y^2}$ is the axial spatial frequency projection of the scattered field. The inverse scattering solution in the object domain is therefore give by:

$$\chi(U, V, W) = \frac{q}{e^{\pm iqz}}U_s(k_x, k_y; z), \tag{1.14}$$

where $U = k_x - k_{xi}$, $V = k_y - k_{yi}$, and $W = \pm q - k_{zi}$. Since the angle-scanning ODT systems are using transmission geometry, we only take the forward $(+q)$ solution. Besides, the measurement is usually performed at the imaging plane, thus, the expression of the scattering potential could be further simplified as $\chi(U, V, W) = q \cdot \Im_{2D}[U_s(k_x, k_y; z = 0)]$, where $\Im_{2D}$ represents the 2D Fourier transform. According to this equation, each measurement of $U_s(x, y; z = 0)$ could be mapped to a particular spherical surface on the Ewald sphere in (U, V, W) space. Changing the illumination angles (k_{xi}, k_{yi}) and mapping the corresponding scatted field into the Ewald sphere, we can eventually recover the 3D spatial frequency of the specimen. After a 3D inverse Fourier transform, the 3D object function in the real space is recovered, thereafter we can reconstruct the 3D RI map. However, limited by the angle-scanning ODT's system, the central low frequency (in U and V) region can not be recovered, which is called the missing cone problem [44].

Other than the depth-scanning and angle-scanning ODT, we can also realize optical diffraction tomography by rotating the sample [46]. In this ODT group, researchers can realize sample rotation with a mechanical rotating stage, or using the flow in mi-

crofluidic channel to make the imaged cells tumbling. However, like depth-scanning ODT, most of the proposed sample rotation method is either difficult to realize or time-consuming. Alternatively, changing the illumination angles with scanning hardware, such as galvoscanner or digital micromirror device (DMD) [32, 47], is quite straightforward to realize. Besides, the emerging high-speed DMD and CMOS camera, could be adopted to angle-scanning ODT for boosting the 3-D imaging speed. Therefore, we adopted the angle-scanning ODT as the foundation for realizing single-shot quantitative 3D label-free imaging.

1.3 Thesis outline

Following the brief introduction in Chapter 1 about the recent progress of quantitative label-free optical imaging techniques, I discussed my PhD work focusing on the development of novel single-shot quantitative optical imaging techniques which could provide with high-speed imaging of fast dynamics in the following chapters. In Chapter 2, I discussed my work about measuring the RBC's morphological, molecular and mechanical parameters simultaneously with label-free quantitative microscopy, which utilized diffraction phase microscopy (DPM) and the engineering of medium's physical properties (extinction coefficient κ_m). In Chapter 3, single-shot quantitative polarization microscopy is discussed which is based on the combination of circular polarization illumination and off-axis shearing interferometry. This novel imaging method is motivated by the study of fast liquid crystal flow in microfluidic channel, where the high speed quantitative imaging methods are missing. In Chapter 4, I introduced the single-shot 3D cell imaging technique (deep-learning single-shot optical diffraction tomography (DS-ODT)) which takes the advantages of angle-multiplexed ODT and deep learning approach. By incorporating with high-speed hardwares (CMOS camera), DS-ODT can push the 3D imaging speed to over 10,000 frame per second, which will potentially advance the field of imaging cytometer. Finally, I summarized the contents of this thesis in Chapter 5, and comment on the future research directions which are built on the effort made by my PhD work.

Chapter 2

Single-shot quantitative amplitude and phase imaging

In this chapter, I introduced my PhD work about realizing the simultaneous measurement of morphological, molecular, and mechanical parameters of RBCs by taking the advantage of QPI while engineering the physical properties of the medium (extinction coefficient κ_m and refractive index n_m). It is envisioned that our method will have impact on clinical diagnosis and drug screening for some blood diseases, such as sickle cell disease and malaria.

2.1 The modeling of RBC biomechanical parameters with quantitative phase imaging (QPI)

The quantification of live red blood cells' (RBCs') biomechanical parameters provides sensitive probes of their structures in nanoscale and new insights of the etiology of a number of human diseases [4, 48, 49]. To study the rheology of live cells, a number of techniques have been exploited to quantify the bending and shear moduli of RBC membranes in static conditions, such as micropipette aspiration [50], electric field deformation [51] and optical tweezers [49]. However, many of these techniques are relatively slow and may not be amendable to quantify the properties of a large population

of cells. Recently, quantitative phase imaging (QPI) approaches based on quantifying thermally driven nanoscale fluctuation of RBC membrane have emerged [3]. Either for resolving complex rheology, or for monitoring dynamic events, QPI is the perfect imaging tool for studying RBCs, since mature RBCs lack nuclei and other internal structures, having a spatially uniform refractive index. Thus, the phase delay of the light field transmitting through RBCs directly results from the morphological changes of membranes.

However, quantifying these thermally driven motions on the nanometer scale is experimentally challenging especially when high speed imaging is required. Among QPI approaches, diffraction phase microscopy (DPM) is commonly used that exploits the near common-path geometry to minimize the influence of mechanical vibration during phase measurements allowing highly stable, high sensitivity, time-lapse video imaging of RBC membrane fluctuations [23]. The cell thickness map ($h(x, y, t)$) could be directly obtained from the mesured phase delay map ($\phi(x, y, t)$):

$$h(x, y, t) = (\lambda/2\pi\Delta n)\phi(x, y, t), \tag{2.1}$$

where λ is the illumination wavelength, Δn is the refractive index difference between the cell plasma and the medium $\Delta n = n_c - n_m$. After the temporal evolution of cell thickness ($h(x, y, t)$) is obtained, we can first calculate the equilibrium shape of the cell, which is $\bar{h}(x, y) = \langle h(x, y, t)\rangle_t$. The displacement of membrane's shape from the equilibrium shape at position (x, y) at time t is defined as $\Delta h(x, y, t)$. For the height-height correlation fucntion $\bar{C}(d, \omega)$, where ω denotes angular temporal frequency. The spatial and temporal Fourier transform is applied to convert the cell displacement map $\Delta h(x, y, t)$ into $\Delta h(q_x, q_y, \omega)$, where q_x, q_y are the components of wavevector in the plane of the membrane. Then the spatial correlation function was obtained as:

$$\bar{C}(d, \omega) = \int |\Delta h(q_x, q_y, \omega)|^2 \exp\left[i(q_x x + q_y y)\right] d^2\mathbf{q} \tag{2.2}$$

where we assume azimuthal symmetry and using $d = \sqrt{x^2 + y^2}$. In ref. [3], a physical model is developed to relate the mechanical parameters of the membrane (i. e. the

shear μ, the area K_A and bending κ moduli) and the viscosities of the cytosol η_c and the surrounding solvent η_s and the radius of the sphere R. The viscosities are fixed to all datasets ($\eta_s = 1.2mPa \cdot s$, $\eta_s = 5.5mPa \cdot s$), according to the relations between the human body temperature and viscosities between the RBC's membrane in ref. [52, 53]. Besides, R is set to be the averaged radius of RBCs directly from the data. Thereafter, the biomechanical parameters of the membrane (the shear μ, the area K_A and bending κ moduli) can be extracted by fitting the theory to the measured correlation functions ($\bar{C}(d, \omega)$). The biomechanical parameters of human RBCs under different shapes (DC, normal shape; EC, speculated shape; SC, nearly spherical) are all able to be extracted with this method, according to ref. [3].

2.2 Instantaneous Phase and Amplitude Microscopy (iPAM) with absorptive medium (Acid Blue 9)

2.2.1 From QPI to iPAM

QPI is a powerful tool to extract the morphological and mechanical properties of red blood cells (RBCs), that have been shown to be important for clinical diagnosis and drug screening of sickle cell diseases and malaria [4, 54, 55]. However, current QPI techniques are still unable to determine the hemoglobin (Hb) concentration in a single cell basis, which is one of the most critical parameters in characterizing the physiological or pathological states of these RBCs. Furthermore, the extraction of biomechanical parameters from membrane's thermal fluctuations with QPI relies on the intracellular viscosity that is quantified via Hb concentration. Besides, QPI needs cell refractive index, n_{cell}, to be quantitative. Without hemoglobin concentration on the single cell basis, we can only previously measure the average Hb concentration to estimate the n_{cell} on a populational level. Therefore, even if QPI is a powerful tool to measure the phase delay caused by RBCs, without quantifying hemoglobin concentration on a single cell level, it can only realize quantitative imaging on the

populational level.

To address this limitation of QPI, we quantitatively image the cell morphology and hemoglobin concentration of RBCs from a single frame interferogram with DPM system, based on a new imaging technique taking advantage of both amplitude and phase of the light field scattered by the RBCs, which is termed instantaneous Phase and Amplitude Microscopy (iPAM). A comprehensive theoretical framework is developed to calculate cell thickness (L) and hemoglobin concentration (c_{Hb}) from the amplitude and phase maps in single cell level. The effect of illumination wavelength has been studied via a theoretical simulation providing the optimal extinction coefficient and refractive index of medium (κ_m, n_m) for this approach. With iPAM, we can truly realize single cell measurement of the morphological, mechanical and molecular parameters of RBCs, which open the avenues for measuring biophysical properties of RBCs in clinical diagnosis and drug screening.

2.2.2 Optical imaging apparatus

We use diffraction phase microscope (DPM) as our optical imaging apparatus for iPAM due to its common-path and off-axis features [23]. Common-path interferometric microscopy entails samples and reference beams side-by-side to ensure the stability required for measuring nanometer motions of biological samples whereas off-axis interferometry is used to acquire single-shot interferograms beneficial for studying fast dynamics of biological systems. In the context of RBCs, these two features make DPM an excellent candidate for measuring rapid thermal fluctuations of the red cell membrane [3]. As shown in Fig. 2-3, using supercontinuum source and an acousto-optic tunable filter, we are able to select any wavelength in the visible range for the sample illumination. The collimated beam on the sample is imaged to a diffraction grating (80 LP/mm) at the microscope image plane (IP1) through an imaging objective (Olympus Ach 40X, NA=0.65) and tube lens (L=16cm). The diffraction grating is conjugated to the camera plane of the microscope (IP2) and generates multiple copies of the field of view. At the Fourier plane, where these copies are separated, a low-pass spatial filter is applied to the non-diffracted order (0^{th}) to create a reference

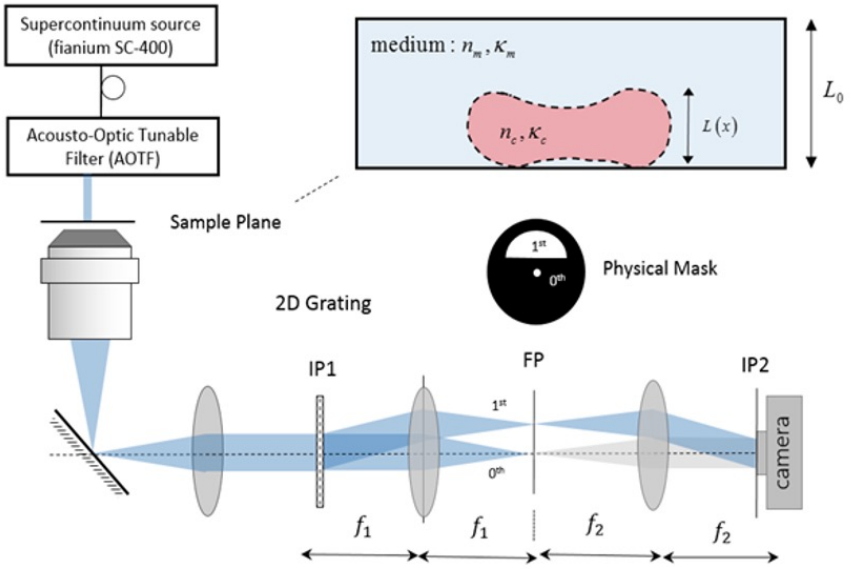

Figure 2-1: **Diffraction phase microscope setup and configuration.** The sample is illuminated with a single illumination color one at a time produced by a supercontinuum source and an acousto-optic tunable filter. The diffraction grating at the image plane of the microscope (IP1) generates multiple copies of the field of view In the Fourier Plane (FP), a physical mask is used to allow only the zeroth and the first order beams to pass through. In addition, the zeroth order beam is spatially filtered (cleaned) by a pinhole to form a plane wave serving as a reference beam. The reference and sample beam interfere at the camera plane (CP) to form the fringe pattern from which phase and amplitude of the sample can be extracted.

beam, but none is applied to the diffracted beam (1^{st} order) which becomes the intact sample beam. The interference of the sample and reference beam subsequently creates fringe patterns on the camera. One can isolate the sample information through a Hilbert transform and obtain amplitude and phase of the optical wave front passed through the sample as explained in more details in the theoretical framework section.

2.2.3 The theoretical framework of iPAM

From the interferogram captured by our aforementioned DPM system, we can not only retrieve the phase delay caused by the RBCs, but also mapping the amplitude

that is caused by the absorption of hemoglobin present in RBCs' cytosol. Since RBCs have simple structures that do not contain nuclei and other organelles, we can assume that the light transmitted through the cell body (not the boundaries) is single scattered. Therefore, our mathematical framework is built based on the principle of geometric optics. For DPM, the incident light transmitting through the sample is separated into multiple orders by a diffraction grating, where only the first order and the zeroth order passes through the Fourier plane, as shown in Fig. 2-1. The beam of the first order can be described as:

$$E_{+1} = \eta E_0 \exp\left[-kL(\kappa_c - \kappa_m)\right] \exp\left[-kL_0\kappa_m\right] \exp\left[i(k_0 x + kL(n_c - n_m) + kL_0 n_m)\right], \tag{2.3}$$

where η denotes the transmission coefficient of the diffraction grating, and the E_0 is the electric field magnitude of the illumination light. k,L and L_0 are the wave-vector of the illumination field, height of the RBC and the thickness of the cell that contains the medium. To describe the intrinsic properties of the sample and the medium, we use κ_c, κ_m, n_c, and n_m to denote the extinction coefficients and refraction indexes of sample and medium, respectively. Here, $k_0 x$ describes how much is the beam tilted away from the optical axis, where x indicates the direction where the beam is titling, while $k_0 = ksin\beta$, and β is the titling angle.

For the 0^{th} order, we filter out the high spatial frequency component and take it as the reference beam, which can be described as:

$$E_{ref} = E_\alpha \exp\left[i\alpha\right] \exp\left[-kL_0\kappa_m\right] \exp\left[ikL_0 n_m\right], \tag{2.4}$$

where E_α is the amplitude of the reference beam, while α is the residual phase which comes from the halo effect [56].

The interferogram we captured from the camera is the interference of these two beams,

which is written as:

$$\begin{aligned} I &= E_{ref}^2 + E_{+1}^2 + \langle E_{ref} E_{+1}^* \rangle + \langle E_{+1} E_{ref}^* \rangle \\ &= \exp(-2kL_0\kappa_m)[E_\alpha^2 + \eta^2 E_0^2 \exp(-2kL(\kappa_c - \kappa_m)) \\ &+ 2\eta E_0 \exp(-kL(\kappa_c - \kappa_m)) \cos(k_0 x + kL(n_c - n_m) - \alpha)] \end{aligned} \tag{2.5}$$

Then with the algorithm of digital holography, we can retrieve the electric field of the sample beam, which is the Eqn. (2.3). However, to normalize the amplitude and phase maps and also eliminate the halo effect, we need to capture another image of the background, which does not contain any sample. The interferogram of the background can be written as:

$$I_{bg} = \exp(-2kL_0\kappa_m)[E_\alpha^2 + \eta^2 E_0^2 + 2\eta E_0 \cos(k_0 x - \alpha)] \tag{2.6}$$

The complex field we acquired is actually the ratio of the two complex fields we retrieved from Eqn.(2.5) and Eqn.(2.6). The amplitude and phase of it are shown below:

$$\begin{aligned} E &= E_1 / E_{bg} = \exp(-kL(\kappa_c - \kappa_m)) \\ \phi &= \phi_1 - \phi_{bg} = kL(n_c - n_m) \end{aligned} \tag{2.7}$$

To simplify the calculation, we introduce optical absorption, which is the negative logarithm of the amplitude:

$$\rho = -\log(E) = kL(\kappa_c - \kappa_m) \tag{2.8}$$

We can treat the cytosol of red blood cells as the solution of hemoglobin, and its refraction index (n_c) and extinction coefficient (κ_c) are modified by the concentration of hemoglobin(c_{Hb}). Their relations can be written as:

$$\begin{aligned} \kappa_c &= \kappa_w(1 + \gamma c_{Hb}) \\ n_c &= n_w(1 + \beta c_{Hb}) \end{aligned} \tag{2.9}$$

where γ is the extinction coefficient increment of hemoglobin, while β is the refractive index increment. Also, κ_w and n_w are the extinction coefficient and refraction index of water. We can obtain β and γ as a function of wavelengths from the refs [57, 58]. Therefore, the parameters n_c and κ_c are known to us. Plugging Eqn. (2.9) into Eqn. (2.7)&(2.8), we can have the matrix form of iPAM retrieval algorithm, which can be described as:

$$\begin{pmatrix} \rho \\ \phi \end{pmatrix} = k \begin{pmatrix} \kappa_w - \kappa_m & \kappa_w \gamma \\ n_w - n_m & n_w \beta \end{pmatrix} \begin{pmatrix} L \\ L c_{Hb} \end{pmatrix} \tag{2.10}$$

In this way, we built up a linear relationship between the measured optical absorption ρ, the phase ϕ and cell thickness L and its multiplication with cell hemoglobin concentration $L \cdot c_{Hb}$. Then we can retrieve the height of the RBC (L) and the concentration of the hemoglobin (c_{Hb}) by inverting the matrix in Eqn. (2.10), that is:

$$\begin{pmatrix} a \\ b \end{pmatrix} = \frac{1}{k} \begin{pmatrix} \kappa_w - \kappa_m & \kappa_w \gamma \\ n_w - n_m & n_w \beta \end{pmatrix}^{-1} \begin{pmatrix} \rho \\ \phi \end{pmatrix} \tag{2.11}$$

Then the unknowns we demand are:

$$\begin{aligned} L &= a \\ c_{Hb} &= b/a \end{aligned} \tag{2.12}$$

Therefore, the general formula for retrieving the cell height L and hemoglobin concentration c_{Hb} could be expressed as the following,

$$\begin{aligned} c_{Hb} &= \frac{(\kappa_w - \kappa_m)\phi - (n_w - n_m)\rho}{n_w \beta \rho - \kappa_w \gamma \phi}, \\ L &= \frac{\kappa_w \gamma \phi - n_w \beta \rho}{k[n_w \beta(\kappa_m - \kappa_w) + \kappa_m \gamma (n_w - n_m)]}. \end{aligned} \tag{2.13}$$

When retrieving the cell height L and the distribution of the hemoglobin c_{Hb} of the RBCs from the measured amplitude and phase maps with iPAM algorithm described in Eqn. (2.13), this system of linear equation has solution if and only if the determinant of the matrix in Eqn. (2.10) is non-zero. Therefore, either the extinc-

tion coefficient or RI (κ_m, n_m) of the medium cannot be the same as those of water (κ_w, n_w). Based on this principle, there are two strategies to create the image contrast for retrieving L and c_{Hb} (generating the differences between the parameters of our medium and water): one is increasing the refractive index difference between the RI of the medium n_m and water n_w; the other is to increase the extinction coefficient of the medium κ_m with absorptive medium (water is almost transparent within most of the spectrum $\kappa_w \approx 0$).

In our previous work, we adopted the first strategy and used various proportions of a commercial density gradient medium ($OptiPrep^{TM}$, Sigma-Aldrich) and phosphate buffer saline (Sigma-Aldrich). The refractive index of medium at 1.3993 is obtained by diluting the gradient medium by approximately 60% phosphate buffer saline. Therefore, the refractive index mismatch between water and medium is approximately 0.0659 at 589 nm. However, the solvent we used for improving the refractive index of the medium also increases the medium viscosity, which suppresses the fluctuation of the RBCs' membranes resulting in higher noise in monitoring thermal fluctuations. Therefore, we obtained the morphological and molecular information, but failed to extract the mechanical information of the RBCs. A possible alternative is adopting the second strategy, where we take the advantage of the medium's high extinction coefficient to calculate L and c_{Hb}. On the other hand, since there are many absorbers that can be dissolved without increasing medium viscosity and hence minimizing effect on the thermal fluctuation of the cell membrane, from which the biomechanical parameters of RBCs are derived.

Here we use Acid Blue 9 (AB9) [59, 60] as our absorptive medium to measure the morphology (cell height L), molecular (hemoglobin concentration c_{Hb}) and mechanical (thermal fluctuations of cell membrane) information of RBCs with iPAM. From the absorption spectrum of AB9 shown in Fig. 2-4 (a), we can see that its absorption peak is located at the wavelength of $\sim 630nm$, where the RBCs are almost transparent (absorption of hemoglobin is almost zero, as shown in Fig. 2-4 (c)). Therefore, the image contrast of the optical field's amplitude $E = \exp(-kL(\kappa_c - \kappa_m))$ is maximized so that we can improve the measurement sensitivity of iPAM. The detailed

sensitivity analysis will be elaborated in the next section.

The extinction coefficient of the AB9 solution κ_m could be determined by measuring the optical absorption of AB9 solution A_m with spectrophotometer, and calculated with the following equation:

$$\kappa_m = \kappa_w + \frac{\log(10) A_m}{2kL_0} \tag{2.14}$$

where A_m is the absorbance of the AB9 solution, k is the wave number and L_0 is the thickness of the cell which contains the AB9 solution. Then we can roughly determine the refraction index of the AB9 solution with Kramers-Kronig [61] relation:

$$n_m(\omega) = 1 + P \int_{-\infty}^{\infty} \frac{\kappa_m(\omega') d\omega'}{\pi(\omega' - \omega)} \tag{2.15}$$

where ω is the frequency of light, $\kappa_m(\omega)$ is the extinction coefficient at frequency ω. P is the Cauchy principle value. In the real experiments, we usually measure the refraction index of the medium at one specific wavelength (589 nm), then determine the spectrum of $n_m(\omega)$ with Eqn. (2.14) and the spectrum of $\kappa_m(\omega)$.

After determining the extinction coefficient and refractive index of the Acid Blue 9 solution (κ_m, n_m), we can return to Eqn. (2.13) to retrieve the cell thickness L and hemoglobin concentration c_{Hb} we are interested. However, other conditions, such as illumination wavelengths, should also be considered since they can also affect the measurement sensitivity. In the following sections, I will introduce our method to determine the optimal illumination wavelength based on the modeling and simulation of measurement sensitivities.

2.2.4 Modeling and simulation of measurement sensitivities

Detection sensitivity is critical to all the optical imaging apparatus since it determines the measurement accuracy and reliability. For iPAM, it is important to have sufficiently sensitive for cell thickness and Hb concentration mappings to deduce the mechanical parameters and pathological states of RBCs. According to the theoretical

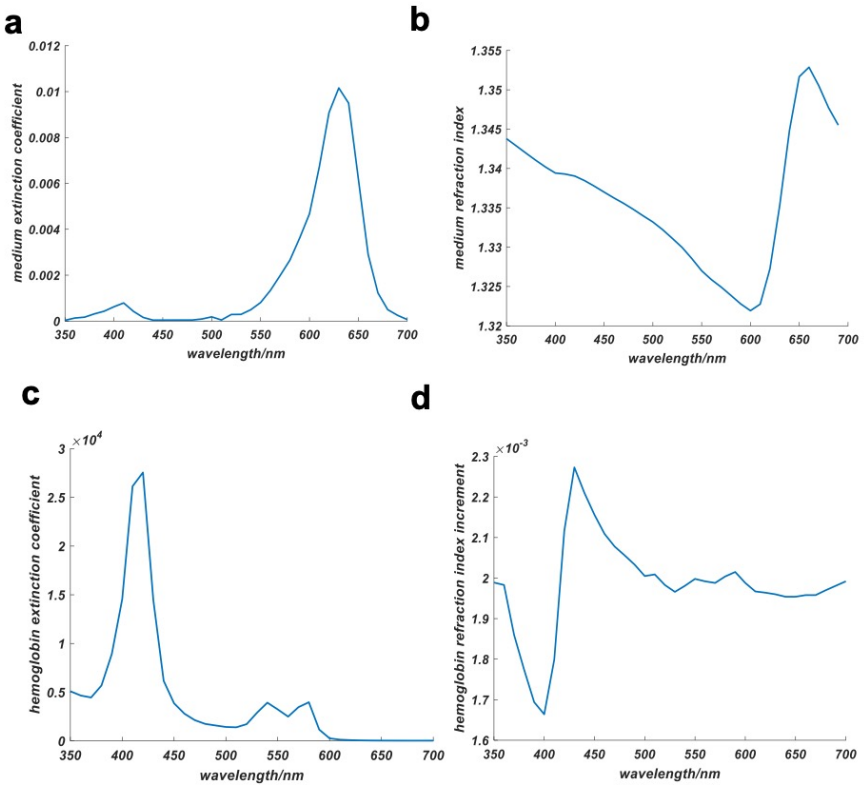

Figure 2-2: **Comparison of extinction coefficient and refractive index of acid blue 9 and hemoglobin.** a. the extinction coefficient (κ_m) of acid clue 9 (AB9) solution with concentration of $7.69g/dL$; b. the refraction index of AB9 solution with the same concentration calculated with Kramers-Kronig relation; c. the extinction coefficient increment γ, and d. the refractive index increment β of hemoglobin in RBC's cytosol, where we know that $\kappa_c = \kappa_w(1 + \gamma c_{Hb})$ and $n_c = n_w(1 + \beta c_{Hb})$.

principles of iPAM, the sensitivity of retrieved parameters is directly related to the detection sensitivity of amplitude and phase. Since we adopt DPM based on near common-path off-axis interferometry that minimizes the influence of mechanical vibration, the sensitivity of amplitude/phase are mostly determined by photon shot noise. As we know, photon shot noise is originated from the Poisson random process of the photons arriving the photon detector, and the uncertainty of intensity δI is proportional to the inverse of the square root of mean photon number N. In iPAM, N is related to both the cellular absorption and the absorption of medium, which could be expressed as $N \sim N_0 \exp\left[-k(\kappa_m L_0 - (\kappa_m - \kappa_x)L)\right]$, where L is the RBC thickness, L_0 is the thickness of cell containing the medium and N_0 is the full well depth of the photon detector (the pixel of CMOS camera).

Additionally, since we are using off-axis interferometry for phase retrieval, the uncertainty of the phase measurement ($\delta\phi$) is related to the contrast of fringes that could be quantitatively manifested by the measured amplitude (E). According to our derivation which is elaborated in Appendix A, we have the expressions for the detection uncertainty of amplitude (δE) and phase ($\delta\phi$):

$$\begin{aligned} \delta E &= \frac{1}{\sqrt{N}} \\ \delta\phi &= \frac{1}{E}\frac{1}{\sqrt{N}} \end{aligned} \tag{2.16}$$

Since we are using the optical absorption(ρ) in iPAM theoretical framework, we should then propagate the uncertainty to the optical absorption and phase.

$$\begin{aligned} \delta\rho &= \left|-\frac{1}{E}\right| \frac{1}{\sqrt{N}} = \frac{1}{E}\frac{1}{\sqrt{N}} \\ \delta\phi &= \frac{1}{E}\frac{1}{\sqrt{N}} \end{aligned} \tag{2.17}$$

In the practice of iPAM, we need to take an image on a uniform background to calibrate our measurements to eliminate the influence of background noise (titling of the optics, defocus, etc). Then the calibrated measurement could be expressed as following:

$$\begin{aligned} \rho &= \rho_1 - \rho_{bg} \\ \phi &= \phi_1 - \phi_{bg} \end{aligned} \tag{2.18}$$

Therefore, the uncertainties of the retrieved optical absorption and phase are:

$$\begin{aligned} \delta\rho &= \sqrt{\delta^2\rho_1 + \delta^2\rho_{bg}} = \sqrt{\frac{1}{E^2N} + \frac{1}{N'}} \\ \delta\phi &= \sqrt{\delta^2\phi_1 + \delta^2\phi_{bg}} = \sqrt{\frac{1}{E^2N} + \frac{1}{N'}} \end{aligned} \tag{2.19}$$

where $N' \sim \exp\left(-2kL_0\kappa_m\right)$, which is the photon number detected after the absorption of the background medium. Then we can determine the uncertainties of the retrieved parameters via the error propagation per the mathematical frame of iPAM algorithm

described in Eqn. (2.11):

$$\begin{pmatrix} \delta L \\ \delta(Lc_{Hb}) \end{pmatrix} = \left| \frac{1}{k} \begin{pmatrix} \kappa_w - \kappa_m & \kappa_w \gamma \\ n_w - n_m & n_w \beta \end{pmatrix}^{-1} \begin{pmatrix} \rho \\ \phi \end{pmatrix} \right| \tag{2.20}$$

while the uncertainty of the retrieved hemoglobin concentration is:

$$\delta c_{Hb} = \frac{1}{L} \sqrt{\delta^2(Lc_{Hb}) + c_{Hb}^2 \delta^2 L} \tag{2.21}$$

Now we have formula that can describe the relation between the uncertainty of measurements $(\delta L, \delta c_{Hb})$ and the experiment parameters $(\kappa_m, n_m, L_0, \gamma, \beta)$; based on this relation, we can design a simulation from which we can select the experiment parameters optimizing the measurement sensitivity.

Firstly, we use our simulation to determine the optimal illumination wavelength. Since κ_m, n_m, γ and β are all functions of wavelength λ as we showed in previous sections, the uncertainty of retrieved cell height and hemoglobin concentration (δL, δc_{Hb}) are also wavelength dependent. To determine the relation between the measurement sensitivity of L and c_{Hb} and the illumination wavelength λ, we implemented a simulation based on the theoretical analysis of iPAM's measurement sensitivity using physiologically valid parameters: medium with refractive index of 1.356, a RBC thicknes of $2.5\mu m$, and the hemoglobin concentration of $33g \cdot dL^{-1}$. The simulated results are shown in Fig. 2-5 (a)&(b), from which we can find the lowest uncertainty is located in the range of $630 - 660$ nm. Therefore we choose an illumination wavelength of $\sim$ 650nm to measure the cell height L and hemoglobin concentration c_{Hb} of RBCs with high sensitivity.

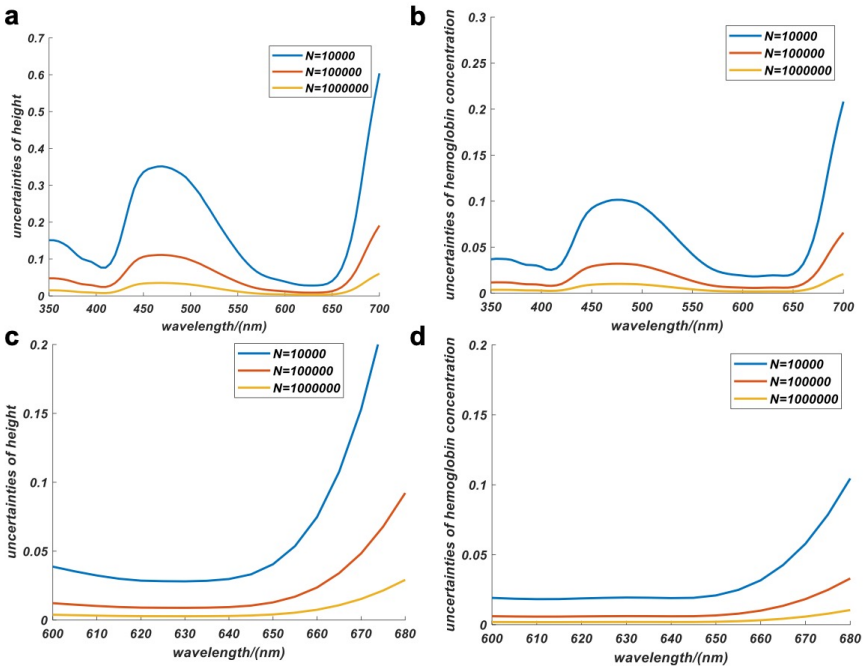

Figure 2-3: **Comparison of extinction coefficient and refractive index of acid blue 9 and hemoglobin.** The uncertainties of retrieved a. cell height δL and b. hemoglobin concentration δc_{Hb} on the dependence of wavelength λ. c & d are the curves of a & b zoomed in the range of $600 - 680$ nm. The blue, red and orange curves show the measurement uncertainty under full well depth of $N = 10,000, 100,000, 1000,000$.

2.3 Experiment validations

2.3.1 Measurement of cell height L and hemoglobin concentration c_{Hb}

To further validate the basic principles of our imaging approach, we performed experiments imaging healthy human RBCs using our iPAM method with acid blue 9 (AB9) as medium. We adopted diffraction phase microscope (DPM) as our optical imaging instrument, in which we use supercontinumm laser (Fianium SC-400) as our light source. An acousto-optic tunable filter (AOTF) is exploited to choose the center illumination wavelength, and the output light beam has a bandwidth of $\sim 8nm$. In this way, we can freely choose the optimal illumination wavelength to maximize our measurement sensitivity; furthermore, the speckle noise was also suppressed since

the spectrum band of our illumination light source is relatively large. Based on our theoretical and simulated analysis of the measurement sensitivity discussed in last session, we choose the illumination wavelength to be 650 nm.

After considerations for the light source and optical instrument, we carefully chose the parameters of the medium for imaging the RBCs. We use the combination of Phosphate-buffered saline (PBS), Bovine serum albumin (BSA) and acid blue 9 (AB9) as the medium to contain the human RBC sample. The human RBCs come from Research Blood Components, LLC. PBS and BSA are used to adjust the osmotic pressure of the medium and keep the RBCs in a healthy state, while AB9 provides with the absorptive agents. The concentration of AB9 also requires carefully selection to balance the interferometric fringe contrast and the sensitivity for measuring amplitude/phase, since high concentration of AB9 in the solution will improve amplitude difference in and out of cells, however, the image intensity will become low due to the high absorption, which means the shot noise will increase and wash out signals. Here we chose the concentration of AB9 to be $7.69g \cdot dL^{-1}$. In this case, the extinction coefficient of the medium is $\kappa_m \sim 0.0105$, and the refractive index of the medium is $n_m \sim 1.349$ according to our calculation based on Kramers-Kronig relation (we firstly measure the solution's RI at 589nm with a refractmeter, then fit the curve calculated by K-K relation to determine the RI at 650 nm). Furthermore, we used spacers to maintain the interval between the two coverslips to be $\sim 10\mu m$, which will also avoid having a too thick absorptive medium causes resulting in insufficient photons reaching the photon detectors.

The preliminary experiment results of imaging human RBC using iPAM method with absorptive medium is shown in Fig. 2-4. The amplitude E and phase ϕ are retrieved from the captured interferogram with digital holography algorithm, and then feed to the iPAM algorithm to output the cell height L and hemoglobin concentration c_{Hb} maps. It worth noting that we took a time-lapsed video with our high-speed CMOS camera at an imaging speed of 250 fps, therefore, all of the retrieved parameters (E, ϕ, L, c_{Hb}) are time-lapse video, and we only show the first frame.

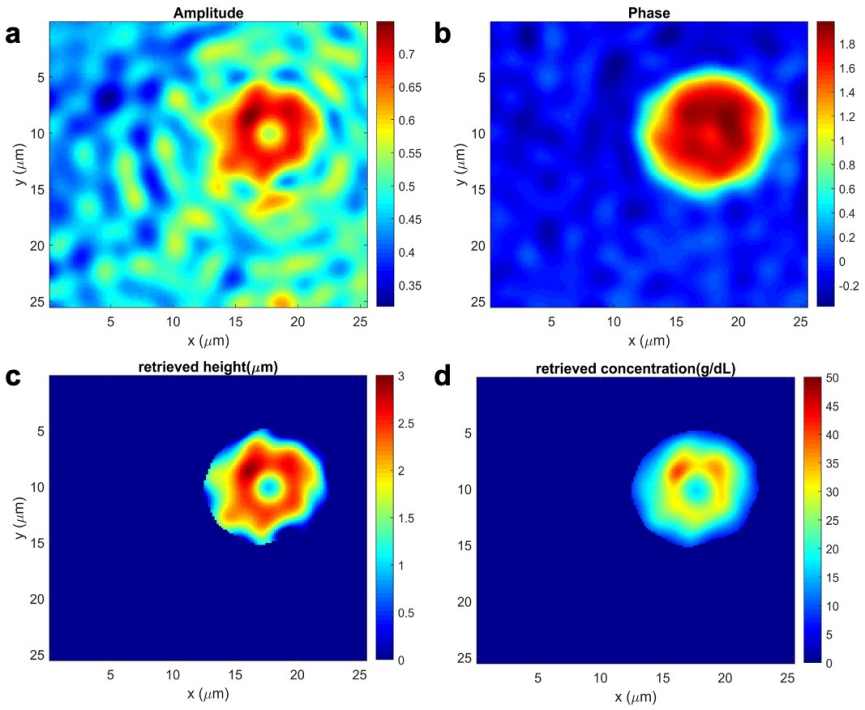

Figure 2-4: **The experimental results of iPAM with AB9 as a dye under the illumination light of 650 nm.** (a) the amplitude map; (b) the phase map; (c) the retrieved height map(the pixels whose phase value is smaller than 0.5 is thresholded); (d) the retrieved hemoglobin concentration map(the pixels whose phase value is smaller than 0.5 is thresholded).

2.3.2 Measurement of membrane fluctuation and retrieval of biomechanical parameters

From the retrieved time-lapse video of cell height L, we can determine the equilibrium shape of the RBC and also the fluctuations of the cell membrane, as shown in Fig. 2-5 (a). As we discussed before, the absorptive dye (AB9) will not significantly increase the medium viscosity, therefore, the thermal fluctuation of the cell membrane is still high enough to be detectable with DPM, which is highly sensitive to phase fluctuation (only limited by shot noise), and the retrieved membrane fluctuation is quite reliable. Then we applied the physical model proposed in ref. [3,4] to extract the biomechanical parameters: bending (κ) and shear (μ) moduli, from the membrane fluctuation data. In this way, we can extract the morphological, molecular and mechanical properties of the RBCs simultaneously. We calculated the parameters of ~ 20 cells and showed

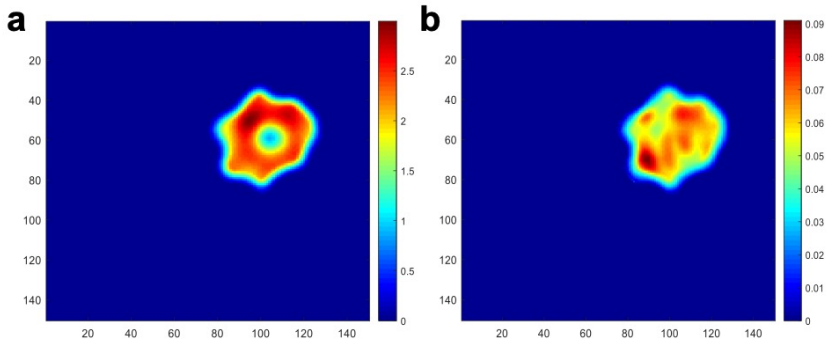

Figure 2-5: **The analysis of RBC membrane's temporal fluctuation.** (a) the equilibrium shape of the imaged RBC; (b) the averaged fluctuation of the membrane. The unit of the colorbar is μm.

the results with a scatter plot in Fig. 2-6 (d)&(e). However, the retrieved shear modulus μ is larger than the values shown in ref. [3, 4] The reason for that is partly because the acid blue 9 may alter the osmotic pressure of the medium, which we did not consider when we prepared the medium.

2.4 Conclusions & Discussions

In this work, we have developed a novel platform that provides accurate measurement of the morphology along with molecular specific information of RBCs, and also biomechanical information of the RBCs' membranes through label-free interferometric measurements. We achieve this goal by acquiring a single interferogram, development of a comprehensive theoretical framework, and systematic simulations accounting for sample and instrument parameters. In theory, extending the experimental measurements and theoretical framework to more illumination wavelengths can provide molecular specific information of proteins and the cell morphology. Particularly, the adoption of absorptive medium (acid blue 9) provides the possibility of measuring the cell morphology and molecular specific information without losing the cell membrane biomechanics, which is retrieved from cell membrane thermal fluctuation. These quantitative parameters retrieved from the captured interferograms open the avenue for data mining for biomarkers useful in clinical studies. After refining

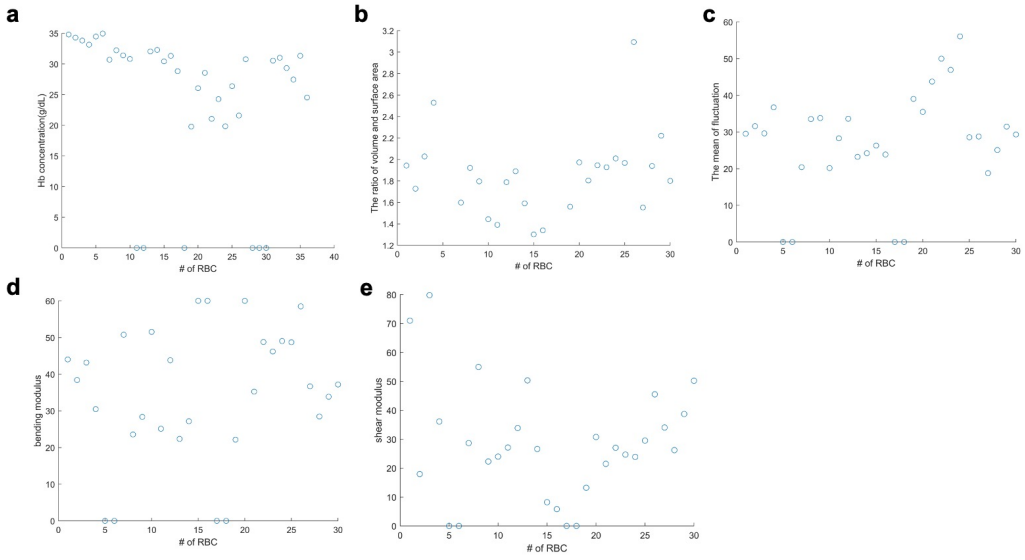

Figure 2-6: **The scatter plot of the imaged RBCs' morphological, molecular and mechanical parameters.** The scatter plot of the imaged $\sim$ 20 RBCs' (a) hemoglobin concentration; (b) volume to surface area ratio (μm);(c) mean fluctuation (μm); (d) bending modulus ($\times k_B T$); (e) shear modulus ($\mu N \cdot m^{-1}$).

the medium's osmotic pressure and extend the throughput by incorporating with a flow cytometer, we envision that our method will provide a powerful imaging tool for clinical studies in the future.

Chapter 3

Single-shot quantitative polarization imaging

In this chapter, novel single-shot quantitative imaging methods are proposed for extracting retardance and orientation angle of the transmitted light that can be related to the mean orientational direction of the liquid crystal molecules. As a demonstration, the flow of disodium cromoglycate (DSCG) in microfluidic channels was measured with speed of ~ 500 fps limited only by camera frame rate. Furthermore, the spatial distribution and the temporal evolution of DSCG flow's retardance patterns are quantitatively analyzed based on our imaging results.

3.1 Liquid crystal flows in microfluidic channels

3.1.1 Rheology of lyotropic chromonic liquid crystals (LCLCs)

Lyotropic chromonic liquid crystals (LCLCs) are aqueous dispersions of organic disk-like molecules that self-assemble into cylindrical aggregates, which form nematic and columnar liquid crystal phases beyond a certain concentration [62–67]. These materials have gained increasing attention in both fundamental and applied research over the past decade, due to their distinct structural properties and bio-compatiblility [65, 68–75]. Used as a replacement for isotropic fluids in microfluidic devices, nematic

LCLCs have opened paths for controlling assembly and dynamics of biological systems [74, 76–80].

Nematic liquid crystals form topological defects under flow, which gives rise to complex dynamical structures that have been extensively studied in thermotropic liquid crystals (TLCs) and liquid crystal polymers (LCPs) [9, 81–90]. Most nematic thermotropic liquid crystals are shear-aligned nematics, in which the director evolves towards an equilibrium polar angle. Defects nucleate beyond a critical Erickson number due to the irreconcilable alignment of directors from surface anchoring and from the shear-alignment in the bulk flow [83, 91–93]. With an increase in shear rate, the defect type can transition from π-walls, to ordered disclinations and to a disordered chaotic regime [94]. Liquid crystal polymers are typically tumbling nematics characterized by a non-zero viscous torque for any direction of the director. Their tumbling characteristics facilitates the nucleation of singular topological defects [82, 95, 96]. Moreover, the molecular rotational relaxation times of LCPs are longer than those of TLCs, and they can exceed the time scales induced by the shear rate. As a result, the rheological behavior of LCPs is governed not only by the spatial gradients of the director field from the Frank elasticity, but also by distortions in the distribution function set by the order parameter [97–101]. With increasing shear rate, topological defects have been shown to transition from disclinations, to rolling cells or periodic orientation patterns, to worm-like patterns or chaotic textures [84, 85, 100]. Recent efforts have aimed to tune and control the defect structures by understanding the relation between the selection of topological defect types and the flow field of TLCs. Strategies to do so include tuning the geometry of microfluidic channels, nucleating defect loops through the introduction of isotropic phases or designing inhomogeneities in the surface anchoring [102–106].

Topological defects occurring in the flow of nematic LCLCs have so far received much more limited attention [107, 108]. At rest, LCLCs exhibit unique properties distinct from those of TLCs and LCPs [62, 63, 65–67, 107]. For example, LCLCs have significant elastic anisotropy compared to TLCs; in particular, the twist elastic constant, K_2, is much smaller than the bend and splay elastic constants, K_1 and K_3. The

resulting relative ease with which twist deformations can occur can lead to a spontaneous symmetry breaking and the emergence of chiral structures in static LCLCs under spatial confinement, despite the achiral nature of the molecules [65, 109–114]. When driven out of equilibrium by an imposed flow, the average director field of LCLCs has been reported to align predominantly along the shear direction under strong shear but to reorient to an alignment perpendicular to the shear direction below a critical shear rate [115–119]. The tumbling nature of this liquid crystal leads to a high sensitivity to shear rate. At shear rates $\dot{\gamma} < 1\ s^{-1}$, the director realigns perpendicular to the flow direction, adapting a log rolling state. For intermediate shear rates, $1\ s^{-1} < \dot{\gamma} < 10\ s^{-1}$, polydomain textures form due to the nucleation of pure twist and mixed wedge-twist disclination loops. Above $\dot{\gamma} > 10\ s^{-1}$, the disclination loops gradually transform into periodic stripes in which the director is predominantly along the flow direction [107].

3.1.2 Quantitative polarization microscopy for imaging the liquid crystal flow

Polarization light microscopes have been used for observing and studying LC systems for over a century since the oriented liquid crystal molecules results in birefringent scattering light. Currently, there are several commonly used polarization-resolved imaging techniques for visualizing LCs flows. For label-free approaches, the most common ones are polarization optical microscopy [24] and LC-Polscope [27, 31]. Conventional polarization optical microscopes (POMs) based on crossing a polarizer and an analyzer before and after the specimen enables high-contrast images that are related to both birefringence and orientation angle of liquid crystal molecules revealing flow-rate dependent LC conformational profiles [94]. However, this approach is not quantitative as the optical signal is related to both the retardance and orientation angle of the LC molecules and cannot distinguish between them. In order to resolve these contributions, multiple orientation of polarizer and analyzer are needed [27]. The LC-Polscope techniques, developed by Oldenbourg and co-workers has greatly

improved the accuracy, sensitivity, and speed this approach by replacing mechanical polarization optics with faster electro-optical LC universal compensators [24, 26, 28]. LC-Polscope has been used in determining the orientation of crystal edges in material characterization [29] and in studying biological processes such as microtubule reorganization during cell mitosis [30, 31]. LC-Polscope has been applied to study LC flow [107] but the imaging speed is restricted by the requirement of making multiple measurements to reconstruct the retardance and orientation angle maps. Fluorescence polarization-resolved microscopy has also been widely used to characterize LC conformations [120, 121]. This approach is based on doping LC with anisometric fluorescent dye molecules that reports on surrounding LC directional field [120, 122]. However, fluorescence approach suffers from a number of shortcomings. The addition of fluorescence sensor may affect LC behavior unless doping concentration is very low. Conversely, the imaging speed and length of observation time is limited by the concentration and photobleaching of these fluorescent sensors. While implementing fluorescent approach with confocal detection enable mapping of LC direction field in 3D, raster scanning approach further limits imaging speed to a few frames per second [122].

3.2 Single-shot quantitative polarization microscopes

3.2.1 Quantitative Polarization Interference Microscopy (QPIM)

Developing another label-free approach, such as the next generation LC-Polscope that can realize quantitative and simultaneous measurements of retardance and orientation angle, will potentially give us more insights of fast dynamic events in liquid crystal systems. Specifically, we combine polarization microscopy with quantitative phase imaging (QPI) [12], in which the scattered optical complex field is retrieved with the implementation of interferometry. With an off-axis QPI system, one can obtain both amplitude and phase information in a single snapshot image [123]. Incorporating QPI into polarization microscopy, one can reduce the number of measurements for quanti-

tative retrieval of polarization parameters, as shown in previous works [25, 124, 125]. While these works represented important advances, they still require multiple measurements to retrieve the polarization parameters. This limitation was overcome when we first introduced a single-shot quantitative polarization imaging technique by utilizing shearing interferometry and a novel retrieval algorithm [126], which is termed Quantitative Polarization Interference Microscopy (QPIM).

The experiment setup for QPIM is shown in Figure 3-1, where a fiber-coupled single-mode 633 nm He-Ne laser is used as the illumination source. After the fiber, the laser beam is collimated with a diameter of approximately 5 mm. A circular polarizer is used to convert the collimated laser beam into right-handed circular polarization before illuminating the sample. After transmitting through the sample, the beam is then collected by an objective lens (Olympus, 4X, numerical aperture (NA) = 0.16). A Wollaston prism (WP10P, Thorlabs), placed at the intermediate image plane, decomposes the sample beam into horizontally and vertically polarized beams (oscillating along x- and y-axes, respectively). These two beams (i.e., the ordinary beam and extraordinary beams) are symmetrically separated along the optical axis with a separation angle of 19.69 degree at the wavelength of 633 nm (the separation angle originates from Thorlabs' specification literature of the Wollaston prisms). A cross section of the Wollaston prism for illustrating its working principle is shown as an inset figure, where we have defined the x-y-z coordinate system. Next, the two beams pass through a 4f system and impinge on a linear polarizer (LP) before interfering on a complementarymetal–oxide–semiconductor (CMOS) camera (Pointgrey, FL3-U3-13Y3M-C; full frame 1024×1280 pixels; pixel size $4.8 \times 4.8 \mu m$) at the final image plane, closely after the LP. For intensity matching, the transmission axis of the linear polarizer is set at 45 degree with respect to the x-y plane. The measurement involves recording fringe patterns (i.e., an interferogram), which is then used to retrieve the complex fields with a Fourier transform method [21]. After a plane wave transmits through a transparent anisotropic sample, the spatial variation of the birefringence properties will mostly induce a change in the wavefront of the illumination wave. Therefore, compared with light intensity, the complex field reveals more information

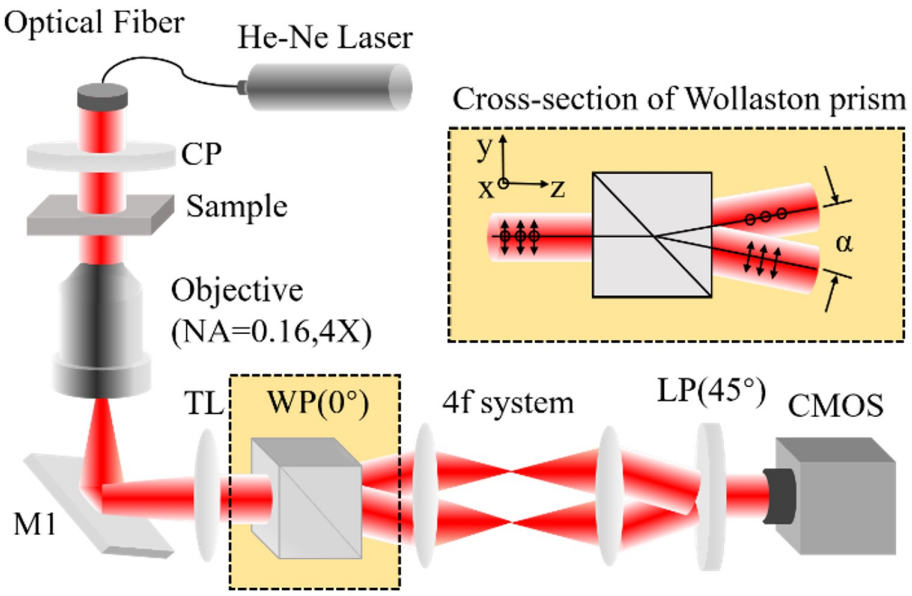

Figure 3-1: **Quantitative polarization interference microscope.** CP, circular polarizer; TL, tube lens; M1, silver mirror; WP, Wollaston prism; LP, linear polarizer. The transmission axis of the LP is set at 45 degrees in the x-y plane. The inset figure shows the cross-section of the Wollaston prism; the circles indicate the polarization along the x-axis and bidirectional arrows represent the polarization along the y-axis. For the selected Wollaston prism, the divergence angle is 19.69 degrees for 633 nm light. The focal length of the tube lens is 200 mm, and the focal lengths of the two lenses used in 4f system are both 150 mm.

of the sample, such as sample thickness and birefringence distributions. Conventional polarization microscopes give qualitative sample information as they only measure the modified intensity maps [24, 29]. In order to recover the polarization parameters (i.e., retardance and orientation angle) in a quantitative fashion, multiple intensity measurements and a complex system are currently deployed. Interferometric microscopy such as QPM allows us to retrieve the complex scattered field from the sample in a single shot. Integrating polarization-sensitive optical elements in an interferometric microscope will enable us to retrieve the birefringence information from the complex electric field due to the interference of the ordinary and the extraordinary sample beams. The retardance and the orientation angle distributions are coupled in the real and the imaginary parts (or amplitude and phase) of the transmitted field.

After a Fourier transform of the interferogram, we obtained the 0^{th} order (i.e., direct

current (DC) term), $+1^{st}$ order and -1^{st} order terms. The $+1^{st}$ (or the -1^{st}) order term gives the complex electric field, $U(x, y)$:

$$U(x, y) = B(x, y) + iC(x, y) \tag{3.1}$$

where $B(x, y)$ and $C(x, y)$ are the real and the imaginary parts of the retrieved electric field. After the formulation, the retardance distribution of the sample, $\Delta(x, y)$, can be recovered as

$$\Delta(x, y) = \cos^{-1}\left[\frac{-2C(x, y)}{A(x, y)}\right] \tag{3.2}$$

where $A(x, y)$ is the intensity of the 0^{th} order term. Furthermore, the orientation angle distribution, $\varphi(x, y)$, can be calculated as

$$\varphi(x, y) = \frac{1}{2}\cos^{-1}\left[\frac{2B(x, y)}{\sqrt{A^2(x, y) - 4C^2(x, y)}}\right] \tag{3.3}$$

However, the Wollaston prism used in this technique severely limits the image field-of-view (FOV) to less than $10 \times 360\mu m^2$. Further, the use of Wollaston prisms requires using low numerical aperture objectives reducing spatial resolution. Finally, the retardance/orientation retrieval algorithm amplifies the measurement noise and deteriorates the imaging sensitivity.

3.2.2 Polarized Shearing Interferometric Microscopy (PSIM)

Given the shortcomings of QPIM, we subsequently developed Polarized Shearing Interference Microscopy (PSIM) that overcomes all these past limitations. In PSIM, we utilize the diffraction grating (with polarizer sheets on Fourier plane) instead of Wollaston prism, which allows large FOV and high-resolution imaging (up to $360 \times 360\mu m^2$). Importantly, a new polarization parameter retrieval algorithm was developed that avoids noise amplification and greatly improves sensitivity. Furthermore, the introduction of supercontinuum laser source significantly reduces image speckle noise and the use of CMOS image and improves acquisition speed. These improvements of PSIM allow us, for the first time, to quantitatively flow induce pattern

formation lyotropic chromonic liquid crystal disodium cromoglycate (DSCG) inside a microfluidic channel at flow rate of over 1 $\mu l/min$ by imaging at over 500 fps.

The system design of polarized shearing interferometric microscopy (PSIM) is shown in Figure 3-2. A supercontinuum laser (Fianium SC-400) is coupled to a single-mode optical fiber to output a broadband, spatially uniform laser beam, which is collimated and transmits through a bandpass filter (centered at 633 nm and the bandwidth is 10 nm). A linear polarizer (LP1) and a quarter wave plate (QWP1) are crossed at an angle of 45 degrees to generate a circularly polarized illumination. The scattered light is collected by an objective (Olympus, NA = 0.3, 10X), and collimated by a tube lens (TL). The beam, which bears the polarization information of the sample, transmits through another quarter wave plate (QWP2), and then are separated into multiple orders by a 100 line-pair per millimeter diffraction grating. The grating is positioned at the conjugated plane of the sample plane. A 4f system is positioned after the diffraction grating to relay the beams. On the Fourier plane, a mask is made to only let the $+1^{st}$ order and -1^{st} order beams pass. Two polarizer sheets are placed on the mask: For the $+1$ order, the direction of the polarization sheet is 45° to the slow axis of QWP2, for the -1^{st} order, the direction of the polarization sheet is -45° to the slow axis of QWP2. Another linear polarizer (LP2) with polarization direction 45 degrees to the polarizer sheets is placed in front of the camera to generate the interference. The interferogram is recorded by a CMOS camera (Optronics, CP80-4-M-500; full frame 2304×1720 pixels; pixel size 7×7 μm^2), whose full well depth is 20000 electrons, and maximum frame rate is 506 frames per second. We use the algorithm of digital holography to quantitatively retrieve the 2D polarization parameters retardance and orientation angle of birefringent samples. The interferogram of a crystalized Orange II fiber acquired with PSIM is shown in Figure 3-3(a), where the fringes appear in the region with high birefringent signals. We perform a two-dimensional Fourier transform to the interferogram, as shown in Figure 3-3(b), which reveals three orders on the Fourier domain (-1^{st}, 0^{th}, $+1^{st}$ order). By extracting the $+1^{st}$ order and shift it to the center, we extract the amplitude E and the phase ϕ. The 0^{th} order gives access to the amplitude of the DC term A. The retardance Δ can

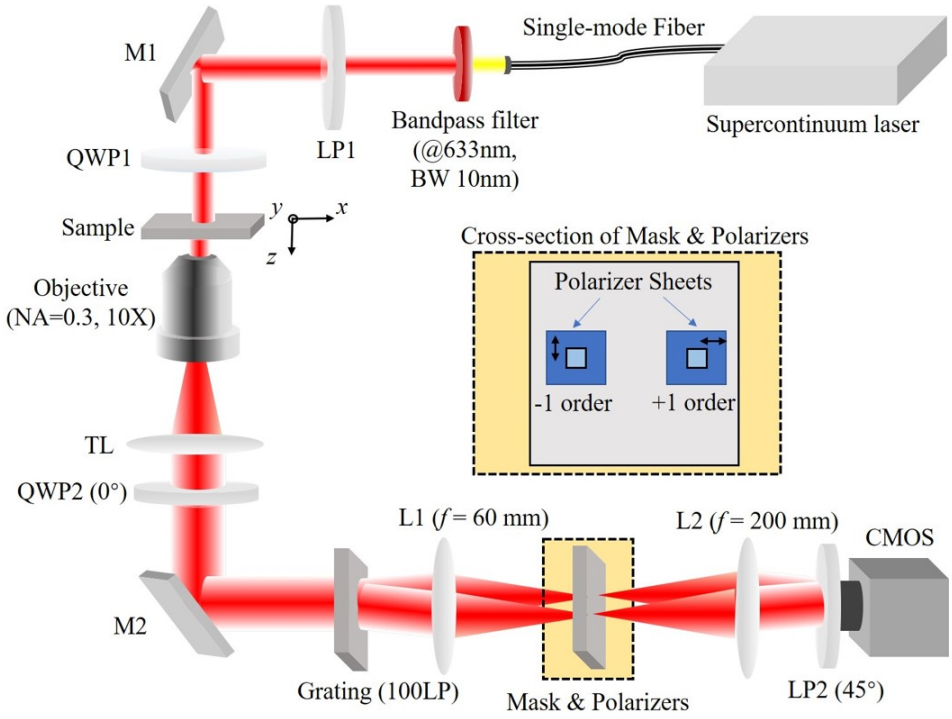

Figure 3-2: **The system design of polarized shearing interferometric microscopy (PSIM).** LP1, LP2, linear polarizers; M1, M2, mirrors; QWP1, QWP2, quarter wave plates; TL, tube lens; L1, L2, lenses. The z axis is the direction of the optical axis, and the xy plane is the sample plane. The zoomed region denotes the location of the masks and polarizer sheets on the Fourier plane.

be calculated as:

$$\Delta = \sin^{-1}\left(\frac{2E}{A}\right) \tag{3.4}$$

and the distribution of the orientation angle φ is calculated as:

$$\varphi = \frac{1}{2}\phi \tag{3.5}$$

The retardance Δ and the orientation angle φ distributions are decoupled into the measured amplitude E and the measured phase ϕ , and shown in Figs. 3-3 (c) and (d), respectively. The derivation of the polarization parameter retrieval and the preparation of the Orange II samples are elaborated in the following part.

With polarized shearing interference microscopy (PSIM), we can extract the retardance map from the amplitude of the retrieved complex field, and the orientation

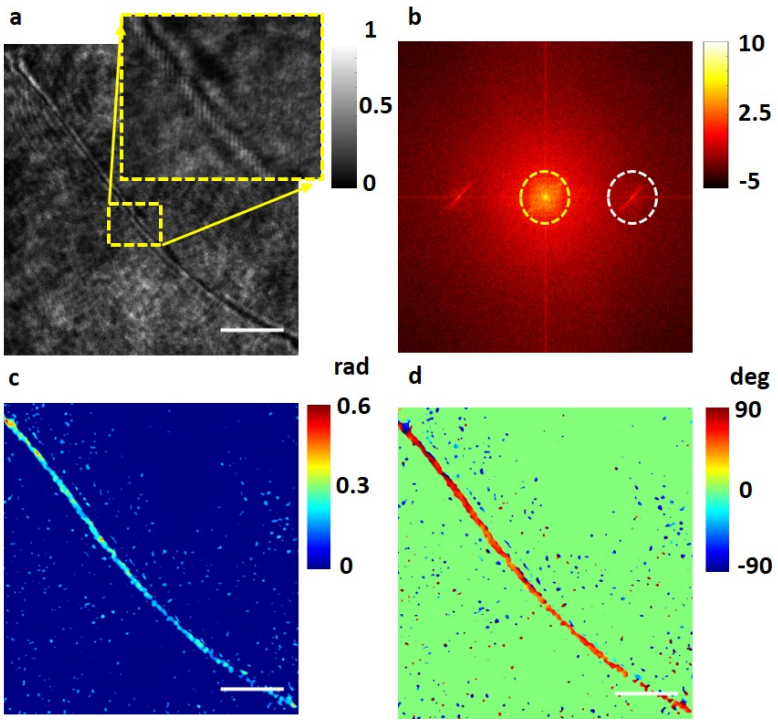

Figure 3-3: **Demonstration of the polarization parameter retrieval algorithm.** (a) The interferogram of crystal fiber sample. The fiber region with high birefringence signal is zoomed in. (b) The logarithm map of the Fourier domain of (a), where 0^{th} and $+1^{st}$ orders are labeled with yellow and red dashed circles, respectively. (c) The quantitative map of the retardance distribution. (d) The quantitative map of the orientation angle distribution. The scale bar denotes 20 μm.

angle from the phase. Here, we will derive and theoretically verify our algorithm with Jones calculus. We start with the Jones matrix of the sample:

$$\begin{aligned} J_{sample} &= \begin{pmatrix} \cos\varphi & \sin\varphi \\ -\sin\varphi & \cos\varphi \end{pmatrix} \begin{pmatrix} e^{i\phi_e} & 0 \\ 0 & e^{i\phi_o} \end{pmatrix} \begin{pmatrix} \cos\varphi & -\sin\varphi \\ \sin\varphi & \cos\varphi \end{pmatrix} \\ &= \begin{pmatrix} e^{j\phi_e}\cos^2\varphi + e^{j\phi_o}\sin^2\varphi & -(e^{i\phi_e} - e^{i\phi_o})\sin\varphi\cos\varphi \\ -(e^{i\phi_e} - e^{i\phi_o})\sin\varphi\cos\varphi & e^{i\phi_e}\sin^2\varphi + e^{i\phi_o}\cos^2\varphi \end{pmatrix} \end{aligned} \tag{3.6}$$

where ϕ_e is the phase delay in the extraordinary axis of the birefringent sample, while ϕ_o is the phase delay in the ordinary axis, and φ is teh orientation angle. The retadance Δ is the difference between the phase delays along extraordinary and ordinary axes, i.e. $\Delta = \phi_e - \phi_o$. All parameters included in Eqn. (3) is 2D maps,

and the Cartesian coordinates (x, y) are omitted here.

In PSIM, we utilize a linear polarizer (LP1) and a quarter wave plate (QWP1) to generate a left-handed circular polarization illumination:

$$\mathbf{E}_{in} = \frac{1}{\sqrt{2}} \begin{pmatrix} 1 \\ i \end{pmatrix} \tag{3.7}$$

After the beam transmitted through the sample, the scatted light will be collected by an objective, and then pass through another quarter wave plate (QWP2). We can write down the output field at this status as:

$$\begin{aligned} E_{out} &= \frac{1}{\sqrt{2}} \begin{pmatrix} 1 & 0 \\ 0 & i \end{pmatrix} J_{sample} \mathbf{E}_{in} \\ &= \frac{1}{2} \begin{pmatrix} e^{i\phi_e}(\cos^2\varphi - i\sin\varphi\cos\varphi) + e^{i\phi_o}(\sin^2\varphi + i\sin\varphi\cos\varphi) \\ e^{i\phi_e}(-\sin^2\varphi - i\sin\varphi\cos\varphi) + e^{i\phi_o}(-\cos^2\varphi + i\sin\varphi\cos\varphi) \end{pmatrix} \end{aligned} \tag{3.8}$$

Then the light is separated by a diffraction grating, and we take the $+1$ and -1 order of the light. Here if we put a polarizer whose orientation direction is 45 degree to the slow axis of QWP2, we will get the output field as:

$$\begin{aligned} \mathbf{E}_{out,45^\circ} &= \frac{1}{2}(e^{i\phi_e} - e^{i\phi_o}) \exp(-i2\varphi) \\ &= \sin\frac{\Delta}{2} \exp\left[i\left(\frac{\phi_e + \phi_o}{2} - 2\varphi + \frac{\pi}{2}\right)\right] \end{aligned} \tag{3.9}$$

We can see that the retardance is only contained in the amplitude part and the orientation angle is contained in the phase part. However, the average phase delay($\frac{\phi_e+\phi_o}{2}$) is still there. Now, we consider about the output electric field when the orientation angle of the linear polarizer (LP2) is -45 degree to the slow axis of QWP2:

$$\begin{aligned} \mathbf{E}_{out,-45^\circ} &= \frac{1}{2}(e^{i\phi_e} + e^{i\phi_o}) \\ &= \cos\frac{\Delta}{2} \exp\left[i\left(\frac{\phi_e + \phi_o}{2}\right)\right] \end{aligned} \tag{3.10}$$

The orientation angle contained in the phase part is disappeared if we rotated the linear polarizer for 90 degree. In PSIM, we use two polarizers on the Fourier plane to generate these two output fields simultaneously: one is in the +1 order, and the other is in the −1 order. That is:

$$\mathbf{E}_{+1} = \sin\frac{\Delta}{2}\exp\left[i\left(\frac{\phi_e+\phi_o}{2} - 2\varphi + \frac{\pi}{2} + \frac{kx}{2}\right)\right] \tag{3.11}$$

and

$$\mathbf{E}_{-1} = \cos\frac{\Delta}{2}\exp\left[i\left(\frac{\phi_e+\phi_o}{2} - \frac{kx}{2}\right)\right] \tag{3.12}$$

kx denotes the spatial modulation(fringes) caused by the separation of the diffraction grating. Finally, we placed another polarizer with orientation 45 degree to both of the polarizers on the Fourier plane. Then we can obtain the interferogram obtained on the CMOS camera:

$$\begin{aligned} I &= \langle(\mathbf{E}_{+1}+\mathbf{E}_{-1})(\mathbf{E}_{+1}+\mathbf{E}_{-1})^*\rangle \\ &= |\mathbf{E}_{+1}|^2 + |\mathbf{E}_{-1}|^2 + \left\langle\mathbf{E}_{+1}\mathbf{E}_{-1}^*\right\rangle + \left\langle\mathbf{E}_{+1}^*\mathbf{E}_{-1}\right\rangle \\ &= \sin^2\frac{\Delta}{2} + \cos^2\frac{\Delta}{2} + 2\sin\frac{\Delta}{2}\cos\frac{\Delta}{2} \\ &\cos\left[\left(\frac{\phi_e+\phi_o}{2} - 2\varphi + \frac{\pi}{2}\right) - \left(\frac{\phi_e+\phi_o}{2}\right) + kx\right] \\ &= 1 + \sin\Delta\sin\left(2\varphi + kx\right) \end{aligned} \tag{3.13}$$

Now it is clear that by retrieving the complex field in the AC term, we can easily calculate the retardance and orientation angle distribution, that is, the formula has been presented in Eqns. (3.4) and (3.5).

3.2.3 Experiment validations

Firstly, we measured the retardance and orientation angle of a quarter wave plate at 532 nm to validate our methodology. As shown in Fig. 3-4 (a), we rotate the fast axis of the quarter wave plate and take the interferograms at every 10 degrees. For each interferogram, we mapped the retardance and orientation angle distributions on

a per pixel basis and then average them over all the field of view. All the retardance and orientation angle mappings are calibrated with the quarter wave plate at a wavelength of 633 nm, with the methods we elaborated in Method section. The averaged retardance and orientation angle, along with their standard deviations over the field-of-view, are shown in Figs. 3-4 (c) and (e) as functions of rotation angle. The nominal values of the retardance and orientation angle for the waveplate are also shown as comparison. For the retardance, the actual value of a zero-order 532 nm QWP is 1.32 rad, and the mean value of all the measured averaged retardance of all the rotation angle is 1.34 ± 0.01 rad, while 0.01 rad is the standard deviation of the averaged retardance values. The averaged spatial standard deviation of retardance value is 0.04 rad as shown with errorbars in Fig. 3-4 (c), which result from the speckle noise or nonuiformity of the background. We believe this value indicates the spatial sensitivity of PSIM system. The orientation angle should track physical rotation angle of the waveplate and is included in Fig. 3-4 (d) as comparison. For processing these PSIM images, Goldstein unwrap algorithm was used to extend the period of the orientation angle from 90° to 180° [127]. The standard deviation of the differences between the measured values and the actual values is 2.57 degree, while the precision of the rotation stage (Thorlabs, OCT-XYR1/M) is 1 degree. The spatial standard deviation of the retrieved orientation angle is 4.84 degree, which is also originated from the spatial sensitivity of PSIM system.

To further validate of this instrument, the retardance and orientation angle of bovine tendon specimen were measured at different rotation angles, which are shown in Figs. 3-4 (b), (e) and (f). The bovine tendons are sliced into specimen with thickness of $5\mu m$, sandwiched between a glass slide and a coverslip, then fixed on the rotation stage (Thorlabs, OCT-XYR1/M) with clippers. The bovine tendons contains abundant collagen fibers which have high birefringent signals; in the meanwhile, the orientation of the fibers are relatively uniform, except for some undulations, so that they can be treated as ideal target to validate the measurement accuracy and imaging performance of PSIM when imaging anisotropic sample with complex structures. In Fig. 3-4 (b), the retrieved retardance maps of the bovine tendon sample are demon-

strated at the rotation angles of 0°, 10°, 20° and 30°. At the same time, a specific region of 100×100 pixels is chosen from the entire field-of-view (1200×1200 pixels), which is tracked when we rotated the sample from 0° to 80° at an increment of 10°. The spatially averaged values and standard deviations of retardance and orientation angle in this tracked region are shown in Figs. 3-4 (e) and (f), as functions on the dependence of rotation angles. For retardance, the mean and standard deviation of the averaged retardance values over all the rotation angles are 0.73 rad and 0.04 rad, respectively, which indicates that the mean retardance does not change so much when we rotate the sample stage. In the meanwhile, the spatial standard deviation of the retardance value has a much larger value 0.11, partly result from the fiberous structure of the collagen which have some fluctuations of retardance over space. For orientation angle, the mean error between the averaged orientation angles and rotation angles is 3.49 degree, which indicates the orientation angle measurement with PSIM is convincing. The large spatial standard deviation of orientation angle (18.19 degree), however, due to the undulation of fiber orientations which is nothing to do with system errors.

3.2.4 Analysis of measurement sensitivity

Here we used a quarter wave plate at 532 nm as our sample to test the temporal sensitivity of PSIM. We captured a video of interferograms at a frame rate of 506 fps, and retrieved the retardance and orientation angle maps of each frame with our polarization retrieval algorithm. Then we picked one pixel in the Field-of-View (FoV), and demonstrated its retardance and orientation angle values' variations on the dependence of time in Figs. 3-5 (a) and (b). Meanwhile, we performed the Fourier transform of the temporal sequences of retrieved retardance and orientation angle, and showed the spectrums in Figs. 3-5(b) and (d). The standard deviation of the amplitude and phase sequences over time is 1.56×10^{-2} and 4.60×10^{-3}, respectively. The full well depth of each pixel is 20000. According to the conclusions in ref. [128], the uncertainty of the measured retardance value is 7.10×10^{-3}, while the uncertainty for orientation angle measurement is 3.60×10^{-3}. Therefore, we validated that the

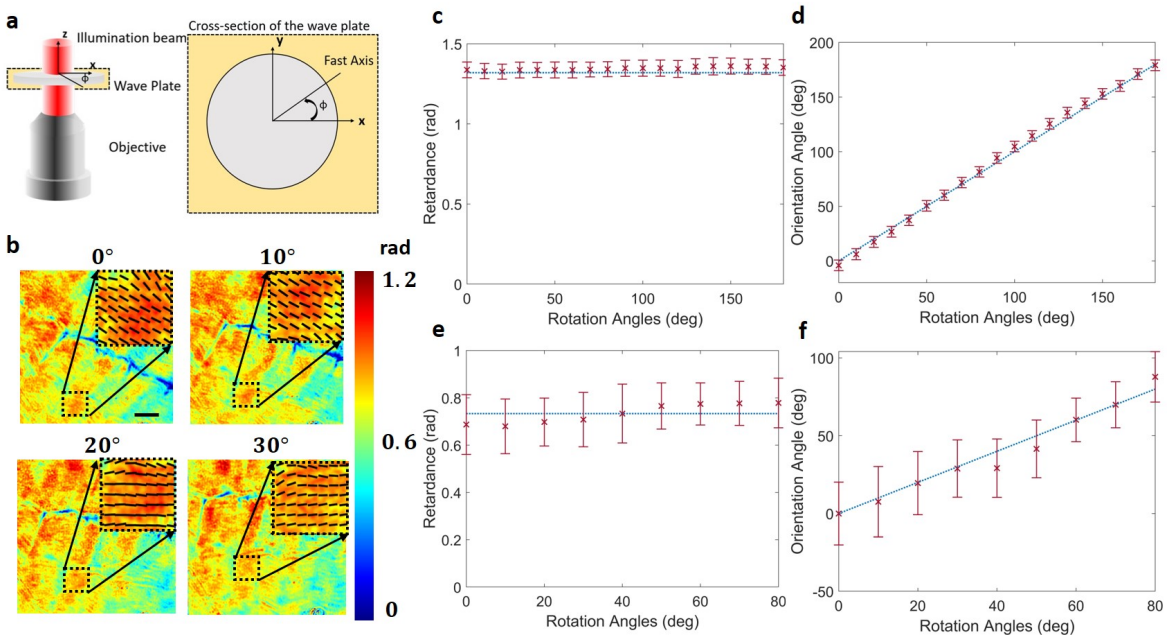

Figure 3-4: **The validation of PSIM imaging concept.** (a) The scheme of the wave plate rotation. ϕ is the angle of the rotation, and we recorded the interferogram every 10 degree. (b), the retrieved retardance map of the bovine tendon specimen when the rotation angle is 0, 10, 20 and 30 degree, respectively. The retrieved orientation angle in the black dashed box region is demonstrated with quiver plots, as embedded in each subfigure; (c)&(d), the quantitative evaluation of the retrieved retardance, and the orientation angle of rotating QWP at 532 nm. The purple cross denote the averaged values, and the error bars show the standard deviations over the field of view. Meanwhile, the blue dashed lines in (c), (d) show the actual value of retardance (1.32 rad), and the values of rotation angles, respectively. The averaged (e) retardance and (f) orientation angle, along with the standard deviation in the region we are interested in (b), are plotted as a function of rotation angles. The scale bar denotes $20\mu m$.

experimental results accord with the theoretical analysis we described before, while the slight deviation may come from some environmental perturbations.

Spatial sensitivity is another important criteria to judge the imaging quality. For quantitative phase imaging system, people usually use light sources with long coherence lengths. Highly coherent light sources will introduce speckle noise in images, which will decrease spatial sensitivity, and degrade imaging quality. In this section, we used a quarter wave plate at 532 nm as our sample to test the spatial sensitivity for our system. Using a supercontinuum laser (Fianium CS400) as our light source, we let the broadband light source to transmit through a band-pass filter (centered at

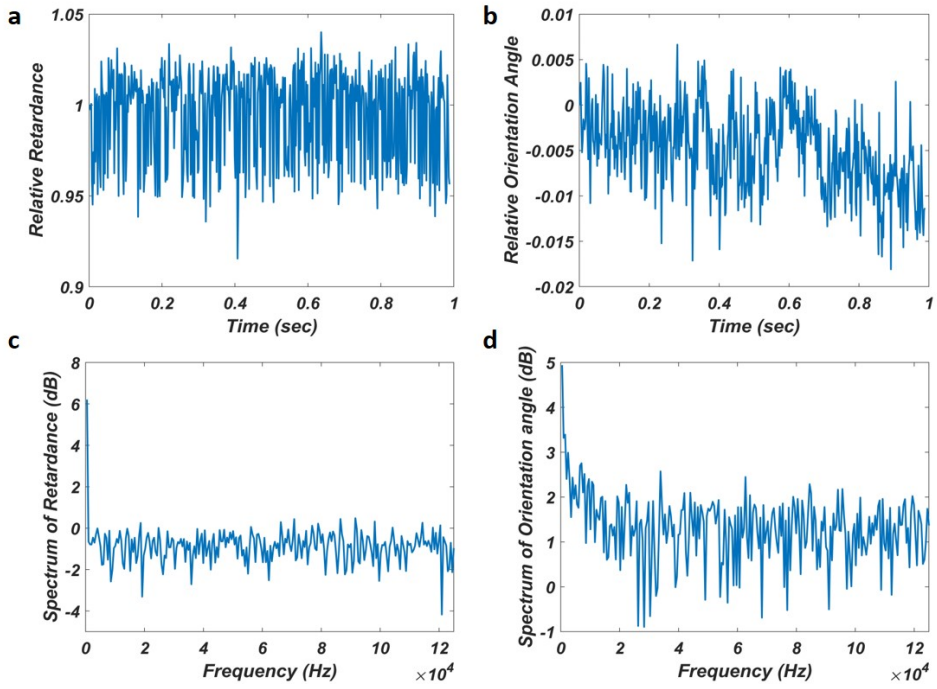

Figure 3-5: **The experiment data for temporal sensitivity analysis.** (a) the time sequence of retardance, where the values of amplitude are picked from one specific pixel in the field of view; (b) the time sequence of orientation, where the values are processed in the same way; (c) the logarithm of the Fourier transform of retardance sequence; (d) the logarithm of the Fourier transform of orientation angle sequence.

633 nm and the bandwidth is 10 nm). The relative large spectrum range of the laser source will decrease the coherence length and reduce the speckle noise effectively. We captured two full interfrogram frames, retrieved the amplitude and phase for both of them. Then we divided these two amplitudes as our 'relative amplitude' that are to be analyzed, while we also subtracted the two phases to obtain the 'relative phase' that will be analyzed. In this way, we can eliminated the influence of the sample and the halo of the phase. Then we used our polarization retrieval algorithm and retrieved the retardance and orientation angle maps. We crop a 250 × 250 area of both retardance and orientation angle maps, which are shown in Figs. 3-6 (a) and (b), and then calculated their standard deviation over the full frames. The standard deviation of retardance is 0.017 rad , and the standard deviation for the phase is 0.223 deg (0.0039 rad). The histograms of both the amplitude and phase are also shown

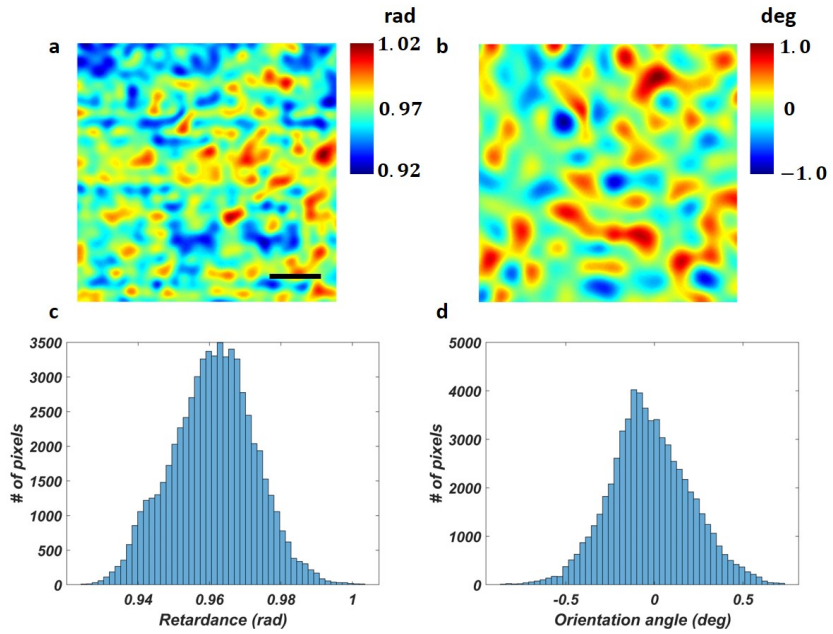

Figure 3-6: **The experiment data for spatial sensitivity analysis.** (a) the map of retardance distribution in radian; (b) the map of orientation angle distribution in degree; (c) the histogram of the retardance map as a function of retardance values; (d) the histogram of the orientation angle map as a function of orientation angle values. The scale bar in (a) and (b) denotes 10 μm.

in Figs. 3-6(c) and (d). This result is very close to our theoretical analysis for the temporal sensitivity, which means that the major source here for spatial noise is shot noise. Therefore, the spatial sensitivity of our PSIM system is validated to be low and our imaging system is able to provide a high quality quantitative imaging of the flowing liquid crystals.

3.3 Analysis of Disodium Cromoglycate (DSCG) flow in microfluidic channels

3.3.1 Polarization parameters of DSCG flow measured by PSIM

Due to the single-shot nature of PSIM, we can quantitatively image the flow behavior of nematic fluids inside the microfluidic channel with high imaging speed. We inject aqueous solutions of the nematic liquid crystal disodium cromoglycate (DSCG) at

$13wt\%$ into a microfluidic device of length $L = 50mm$, width $W = 15mm$, and thickness $b = 6 \pm 1\mu m$, as shown in Fig. 3-7(a). To ensure a well-controlled initial condition of the liquid crystal, we use a protocol of surface rubbing which induces a planar alignment of DSCG along the direction of the flow. We allow the sample to fully relax before starting the flow. The flow is induced by injecting DSCG at a precise volumetric flow rate set by a syringe pump (Harvard PHD 2000). Once the flow has reached a steady-state, we image the sample at a frame rate of 506 fps in a $252 \times 252\mu m^2$ region far from the inlet to avoid artifacts due to the injection protocol. Note that the birefringence of $13wt\%$ DSCG is ~ -0.015 at a wavelength of 633 nm [129, 130] which leads to a maximum retardance of $\sim 0.98 \pm 0.15$ rad, well within the maximum measurable value of PSIM, which is $\pi/2$.

The measured retardance and orientation angle maps are related to the collective behavior of the director field of liquid crystal molecules (aggregates) in DSCG flows, as shown in Fig. 3-7 (a). The measured orientation angle ϕ denotes the averaged in-plane orientation angle along the z-direction, which describes how the LC molecules oriented in x-y plane. In the meanwhile, the retardance Δ is the integrated phase difference between the projected extraordinary and ordinary axes of the liquid crystal. Different flow rates induce different 3D orientational heterogeneity in DSCG LC resulting in different patterns of the retrieved retardance and orientation angle maps.

In this paper, a time-lapse video of the DSCG flow is acquired with PSIM at an imaging speed of 506 fps, while both the retardance and orientation angle maps are retrieved for each frame. In Fig. 3-7 (b), we demonstrated the mapping and quiver plot of the retardance, and orientation angle retrieved by PSIM under a flow rate of 1 $\mu l/min$. The direction of flow is from left to right in the image. The quantitative polarization images of the DSCG flow are represented as a colormap of retardance and a quiver plot of the orientation angle, where the colors represent the magnitude of retardance, and the direction of the rods denotes the orientation angles. The length of the rods further denotes the retardance value.

In ref. [107], the authors have carefully investigated the physics of static patterns of the retardance and orientation angle maps of DSCG flow in the microfluidic channel

under different flow rates. However, limited by the imaging speed of the polarization imaging techniques, the high-speed quantitative polarization imaging of the DSCG flow's dynamics is still missing. Thanks to the large FOV and high imaging speed of PSIM, we can perform quantitative temporal dynamics analysis of the DSCG flow in microfluidic channels for the first time. Firstly, we quantify the temporal evolution of retardance and orientation angle maps at different frames by computing their Pearson Correlation Coefficient (PCC) with the first frame at a time interval of 2 ms within a time span of 40 ms. The curves of retardance and orientation angle maps' PCC values as functions of time are shown in Fig. 3-7 (c), from which we can observe a clear trend of linear drop over time. To observe the temporal evolution of the polarization parameters' patterns more clearly, we extract small patterns (100×100 pixels) of retardance and orientation angle out of the whole FOV and tracking their evolution over time. The mapping and quiver plots of the selected patterns' polarization parameters are embedded in Fig. 3-7 (c), with the time interval of 8 ms. The positions of the selected patterns are centered at the low-retardance regions (< 0.2), which are of great interests for the study of DSCG flow's dynamical properties. More specific and detailed physical analysis of the dynamical behaviors of DSCG flows in microfluidic channels based on PSIM measurements will be elaborated in the following sections.

3.3.2 Characterization of patterns of DSCG flows*

To quantify the structures of DSCG flow, we determine the characteristic size of the domains of varying retardance by calculating the normalized 2D spatial autocovariance in the x- and y-directions, C_x and C_y, as shown in Fig. 3-8 (a),(b) [129]. The observed decrease in domain size with increasing flow rate is reflected in a decay of the autocovariance at increasingly smaller Δx and Δy. For the two lowest and the highest flow rates probed, C_x and C_y exhibit a two-step decay suggesting a coexistence of structures of two characteristic sizes. We use a double compressed exponential fit to access the characteristic length scales L_{x_1}, L_{x_2}, L_{y_1} and L_{y_2}, characterizing the

average sizes of structures along the x- and y-direction. For the intermediate range of flow rates, we can fit C_x and C_y with a single compressed exponential function, which yields L_x and L_y. Remarkably, L_x and L_y decrease systematically with the average shear rate $\bar{\dot{\gamma}} = \frac{q}{wb^2}$ for $4\text{s}^{-1} < \bar{\dot{\gamma}} < 500\text{s}^{-1}$, where q is the flow rate, and w and b the width and the thickness of the channel, as shown in Fig. 3-8 (c). The average characteristic size, defined as $L = \sqrt{L_x L_y}$, exhibits a power law dependence with the shear rate, $L \propto \bar{\dot{\gamma}}^{-0.19}$. The domains are elongated in the flow direction, with an approximately constant aspect ratio $L_x/L_y = 1.8 \pm 0.3$, as shown in Fig. 3-8 (d). A decrease or an increase in shear rate leads to different characteristics of the domain sizes and the aspect ratio, and we will first focus our discussion on the intermediate range of shear rates.

3.3.3 Characterization of temporal evolution of DSCG flows*

To characterize the temporal evolution, we calculate the normalized spatiotemporal autocovariance, C_t. As the flow velocity varies across the channel, we subtract the contribution of different flow velocities across the gap, V_f, to the dynamics by using a Lagrangian framework, where we move the region of interest by $\Delta x = V_f \Delta t$ at each time lag Δt. For example, when V_f is equal to the average velocity $\bar{V}$ under differenet average shear rates, the normalized spatiotemporal autocovariance is shown in Fig. 3-9 (a). We then find the best-fit of the C_t in the range of intermediate average shear rates at different V_f with a stretched/compressed exponential function, which yields a timescale, which characterizes the fast dynamics related to one dominant mode. Also, the timescale monotonically decreases with shear rates. When the average shear rates transition to be lower or higher, C_t again exhibits a two-step decay which can be fitted by a double-stretched/compressed and which yields two time scales corresponding to two deformation modes.

We here focus on the temporal evolution in the special range of intermediate average shear rates, where the characteristic time are obtained from the spatiotemporal autocovariance, τ, reflects the combined effect of the relaxation time related to the fluctuation of defects induced by shear stress, τ_1, and the time scale related to the

translation of defects controlled by flow velocity, τ_2. τ obtained from the fitting of spatiotemporal autocovariance on different reference frames moving with velocities, V_f, is shown in Fig. 3-9 (b). τ is controlled by both the average shear rate and $V_f/\bar{V}$. With the increase of average shear rate, the inverse of τ, τ^{-1}, systematically increase. However, τ^{-1} demonstrates a non-linear dependence on $V_f/\bar{V}$: τ^{-1} decreases with the increase of $V_f/\bar{V}$ and approaches a minimum when $V_f/\bar{V}$ is between 1 and 1.5; with further increase of $V_f/\bar{V}$, τ^{-1} increases. The contribution of τ_1 and τ_2 to the total time scale of fast dynamics τ can be seen in a simple analysis of the spatiotemporal autocorrelation by assuming exponential decays for both spatial and time autocorrelation and by taking into account a reference frame moving at the same velocity as the central mass of defects, V^*, which gives rise to the relation: $\frac{1}{\tau} = \frac{1}{\tau_1} + \frac{\left|V^* - V_f\right|}{L_x}$. V_f corresponding to the lowest τ^{-1} reflects the central mass velocity of defects, V^*. We find that V^* is in between 1 and 1.5 times of the $\bar{V}$. This demonstrates that most defects stay in the bulk of flow rather than near the boundaries. Fitting τ yields a characteristic time τ_1 related to the fluctuation of defects and characteristic length scale along x-direction, as shown in Fig. 3-9 (c). The length scale fairly well agrees with the experiment results in Fig. 3-8 (c). This agreement validates the relation among τ_1, τ_2 and τ. Moreover, τ_1 decreases with the average shear rate with the power law of -1.17. The fluctuation of defects can be reasonably scaled by $\tau_2 \propto L/\bar{V}$. Combining the dependence of L on the average velocity as obtained in Fig. 3-8(c) yields $\tau \propto V^{-1.19}$, in agreement with the experiment results.

3.4 Conclusions & Discussions

In this section, I discussed the proposed novel single-shot polarization microscopy techniques motivated by the studies of liquid crystal flows. Compared with QPIM which is proposed several years ago, PSIM has larger Field-of-View (FoV) and more straightforward retrieval algorithm that is more suitable for the quantitative imaging of the dynamics of nematic liquid crystals. The imaging concept and the polarization

retrieval algorithms have been fully described and derived. The retrieval accuracy and efficiency have been validated with a sample of rotating wave plate and bovine tendon slices. Thanks to the single-shot nature and satisfactory imaging performance, PSIM provides a powerful tool to quantitatively probe the director field of anisotropic materials at an imaging speed of over 500 fps. Furthermore, the retardance map's patterns of DSCG flow under different flow rates captured by PSIM reveal domain structures and topological defects in pressure-driven flow of nematic DSCG. We particularly develop quantitative understanding of a special range in intermediate average shear rates. Therefore, PSIM is believed to open up the avenue for more comprehensive study of DSCG flow's dynamical properties. We believe that PSIM is a powerful tool to observe dynamics of anisotropic materials, and there will be more exciting discoveries with PSIM in the future.

However, even if PSIM can provide with fast and highly accurate polarization imaging, the retardance and orientation angle maps it provided are still in 2D. In the future, we are planning to improve the PSIM system by adding optical sectioning ability via using a broadband light source and dynamic speckle illumination. This new system may enable the 3D imaging of LC flow and other anisotropic specimens. In this way, we can envision the PSIM method with 3D imaging will become essential for many applications in material inspection and biomedical research.

** these sections credit to Qing Zhang, prof. Irmgard Bischofberger and prof. Rui Zhang*

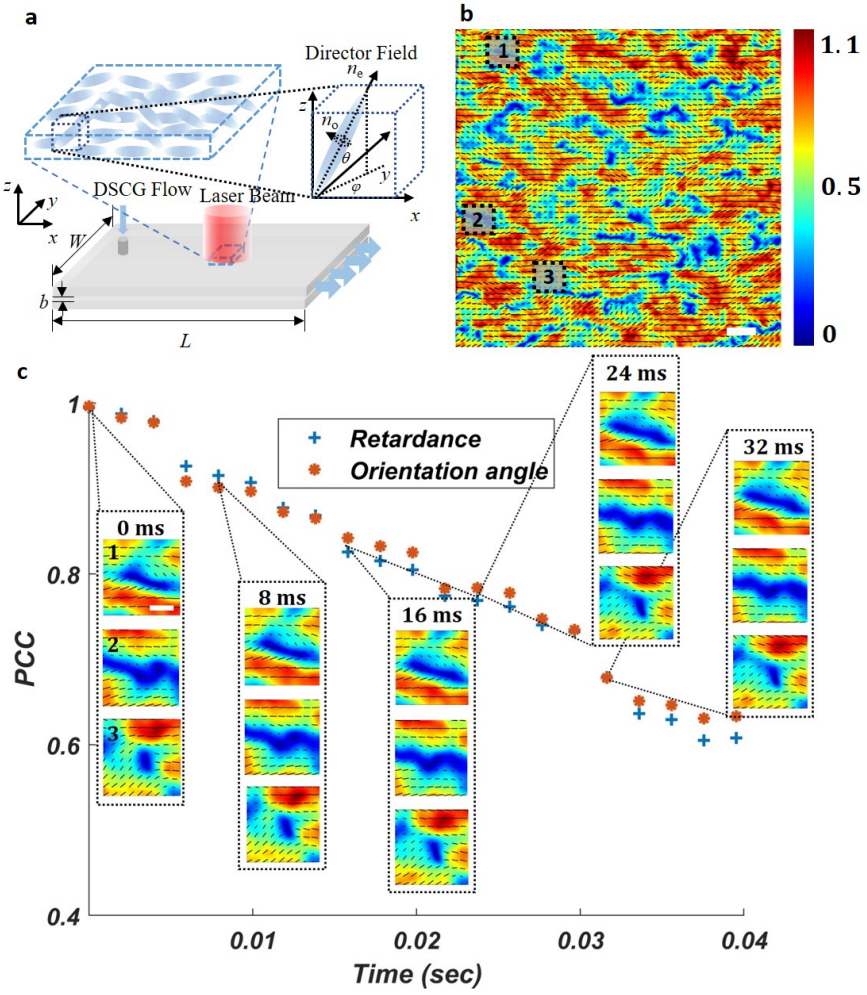

Figure 3-7: **The temporal evolution the retardance and orientation angle maps of LC flow measured by PSIM.** (a) Schematics of DSCG flow inside the microfluidics channel with a geometry of $L = 50mm$, $W = 15mm$, $b = 6\mu m$. The director field of a single LC aggregate is also shown. (b) The retardance and orientation angle maps measured by PSIM under a flow rate of $1\mu l/min$. The color and the length of the rods represent the magnitude of retardance, the direction of the rods denotes the orientation angle. Three patterns with size of 100×100 pixels which will be carefully investigated in (c) are labeled and numbered. (c) the curve of Pearson Correlation Coefficient (PCC) of retardance and orientation angle maps on the dependence of time. The temporal evolution of the selected patterns in (b) are also embedded. The imaging speed is 506 fps, and the picked time points in (c) are 0, 8, 16, 24, 32 ms. The scale bars in (b) and (c) denote $20\mu m$ and $10\mu m$, respectively.

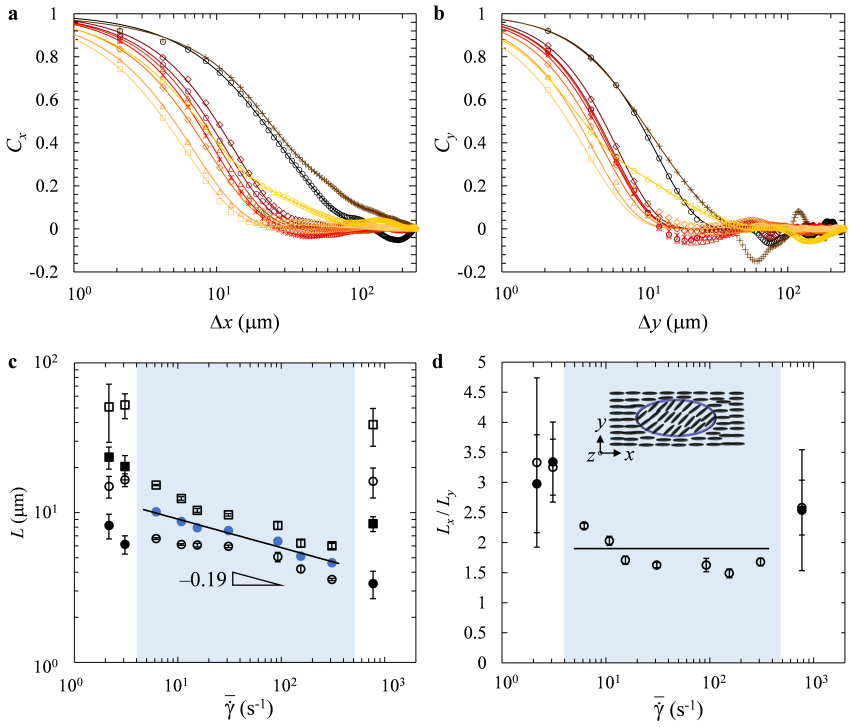

Figure 3-8: **Characteristic size of structures in flowing DSCG controlled by average shear rate.** (a,b) Normalized 2D spatial autocovariance along x-direction (a) and along y-direction (b). The solid lines denote compressed single or double exponential fits. (c) The characteristic domain sizes along x-direction ((□) and (■)), along y-direction ((○) and (●)), and average over x- and y-directions (○) versus average shear rate $\bar{\dot{\gamma}}$. The black line denotes $L \propto \bar{\dot{\gamma}}^{-0.19}$. (d) Aspect ratio L_x/L_y. The black line indicates $L_x/L_y \propto K_3/K_1 = 1.9$. Inset: Schematics of a pure twist disclination loop.

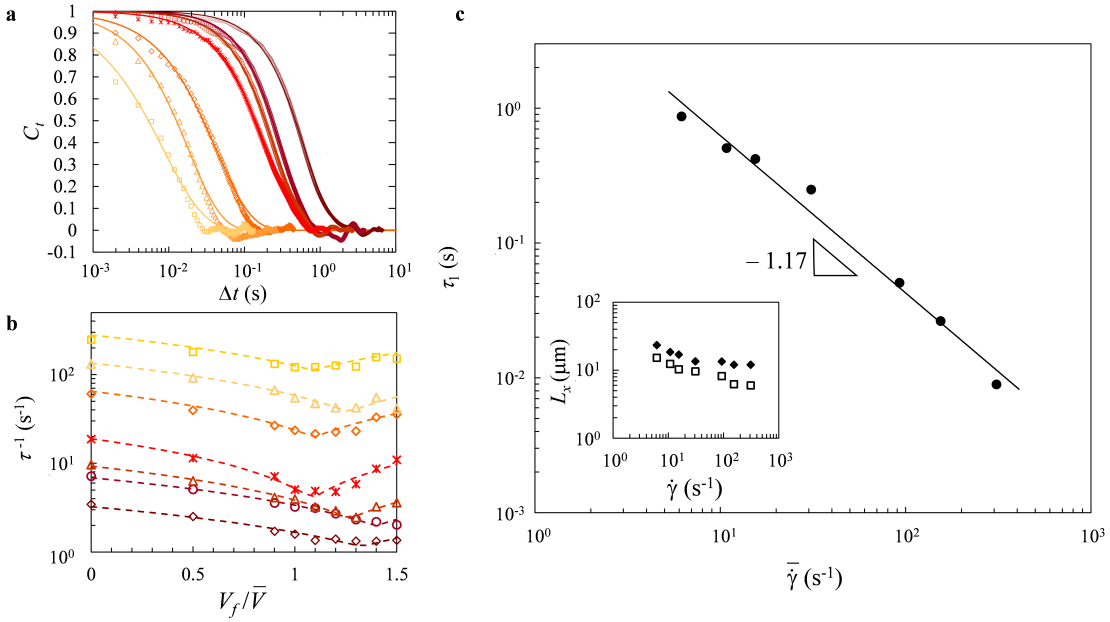

Figure 3-9: **Temporal evolution of disclination loops.** (a) Normalized spatiotemporal autocovariance obtained by moving the window of interest by $\Delta x = V_f \Delta t$ at each time lag Δt and by setting V_f equal to the average velocity $\bar{V}$ at different average shear rates(maroon ◇): 0.2 μl/min, (burgundy ○): 0.35 μl/min, (dark red △): 0.5 μl/min, (red ∗): 1 μ/min, (reddish orange ◇): 3 μl/min, (orange △): 5 μl/min, (amber □): 10 μl/min. The lines denote compressed exponential fits. (b) Inverse characteristic time, τ^{-1}, versus $V_f/\bar{V}$ at different average shear rates: (maroon ◇): 0.2 μl/min, (burgundy ○): 0.35 μl/min, (dark red △): 0.5 μl/min, (red ∗): 1 μ/min, (reddish orange ◇): 3 μl/min, (orange △): 5 μl/min, (amber □): 10 μl/min. The dashed lines denote best-fits to $\tau^{-1} = {\tau_1}^{-1} + |V^* - V_f|/L_x$. V^* is the central mass velocity of defects and τ_1 is the time scale characterizing the fluctuation of defects. (c) τ_1 decreases with increasing average shear rates (●). The black line denotes $\tau_1 \propto \bar{\dot{\gamma}}^{-1.17}$. Bottom inset: Comparison between L_x from fitting τ^{-1} (⧫) and L_x from fitting the normalized spatial autocovariance (□).

Chapter 4

Single-shot 3D optical imaging of biological cells with deep-learning approach

In this chapter, I report my PhD work on developing a single-frame quantitative cell tomography technique, termed deep-learning single-shot optical diffraction tomography (DS-ODT) that realized 3D cell imaging at speed over 10,000 frame per second with submicron spatial resolution. DS-ODT is based on an angle-multiplexed interferometric imaging system and a deep-learning based image reconstruction model. Using DS-ODT, we demonstrated 3D imaging of red blood cell deformations in 3D sheared by flow in microfluidic channels and high throughput 3D cell imaging at over 5000 cells/second. With unprecedented imaging speed while keeping submicron resolution, we envision DS-ODT will find a wide range of applications in biology and medicine.

4.1 Introduction

Cellular imaging is central for biological research and medical diagnosis. In particular, the observation of cellular dynamic processes, such as cell migration [14], neural action potential [2], membrane fluctuation [3, 4], and fast-moving cells in flow cy-

tometers [5], are increasingly attracting researchers' attention. To resolve these fast cellular dynamic process (usually happened in milliseconds with spatial features in micrometers), the priority is to improve the optical microscopes' temporal resolution. Recently, a multitude of novel high-speed optical imaging techniques have been proposed. First of all, optical time-stretch imaging techniques, such as serial time-coded amplified microscopy (STEAM) [1, 131, 132] and compressed ultrafast photography (CUP) [133–136], provided an effective strategy to break the speed limit of the image sensors and pushed the frame rate to over 10^6 fps. However, these techniques are mainly 2D, has limited spatial resolution and provide mostly qualitative imaging. Even if some recent works have partly addressed part of the problem [137,138], based on lines-canning and asymmetric-detection, they still cannot provide 3D information of cells.

Reconstructing 3D structure of biological cells is critical for resolving cellular dynamical events. However, conventional 3D imaging techniques [139–141] requires multiple measurements of angle-scanning or depth-scanning, which are time-consuming. By incorporating novel high-speed light scanning and photon detection hardware [142,143], these techniques' 3D imaging speed could reach several fps [144–147]. Lately, several single-frame 3D fluorescence imaging techniques have been developed [148, 149] and a single-frame label-free tomographic imaging technique based on optical coherence microscopy (OCM) has been inplemented [150], which improved the 3D image speed to a camera-acquisition-limited level. However, the poor spatial resolution and lack of quantitative information still limited their applications to the imaging of cellular dynamic scenes.

In recent decades, the emergence of quantitative label-free imaging opens up new avenues for cell imaging, since it overcomes the limitations of photobleaching and phototoxicity while providing, qualitative imaging [12]. In particular, the 3D quantitative label-free imaging techniques, such as optical diffraction tomography (ODT), simultaneously provides with 3D morphology and intrinsic biophysical/biochemical marker's distribution (RI map) of biological cells [32, 36, 42, 45, 151, 152]. However, ODT, based on widefield microscopy, is inherently high-speed compared to many

3D imaging techniques and high-speed angle scanning hardware, such as digital micromirror device (DMD), has been adopted to ODT can further boosting imaging speed [43, 47]. Many faster cellular dynamic events or characterizing a large cell population, still require higher throughput ODTs. In the following sections, I will firstly introduce the basics of physical-model based ODT and deep-learning based computational imaging, which are the key building blocks for developing DS-ODT that has demonstrated unprecedented 3D imaging speed.

4.1.1 Physical model based Optical Diffraction Tomography (ODT)

Here I introduce the physical principles and mathematical framework for reconstructing 3D RI maps with angle scanning ODT. It worth noticing that this section is important since even if we use data-driven method to improve imaging performance (spatial resolution, imaging speed, etc) in DS-ODT, the ground truth RI maps we used for the training dataset still require accurate physical modeling of the ODT imaging process. Firstly, we can formularize the forward model for reconstructing a three-dimensional refraction index (RI) map with angle-scanning captured holograms as following:

$$g_m = S_m(\mathbf{x}) \tag{4.1}$$

where g_m is the measured complex field of the m-th illumination, while $\mathbf{x}$ is the 3D refractive index (RI) map we want to solve. S is the operator we can map the refraction index to the measured field, which could be formulated with different physical theories. Then the inverse problem of Eqn. (4.1) can be described as following:

$$\hat{\mathbf{x}} = argmin_{\mathbf{x}} \sum_{m=1}^{N} \|S_m(\mathbf{x}) - g_m\|_2^2 \tag{4.2}$$

where $\hat{\mathbf{x}}$ is the estimated refractive index (RI) map using N illumination angles. The forward model S is nonlinear, therefore, directly solving Eqn. (4.2) is quite difficult. One of the solutions is to linearize Eqn. (4.2) with proper approximations. For

examples, to image biological cells, we usually apply first-order Rytov approximation [42], which could simplify Eqn. (4.1) to be as following:

$$S_m(\mathbf{x}) = A_m\mathbf{x} = \int_V \mathbf{x}(\mathbf{r}')e^{-i(\mathbf{k}-\mathbf{k}_m)\cdot\mathbf{r}'}d\mathbf{r}' \tag{4.3}$$

where A_m is the linear model generated by Rytov approximation for the m-th illumination angle, which is basically mapping the 3D refraction index into a 2D Fourier space. $\mathbf{r}'$ is a spatial coordinate of a point in spatial domain, while $\mathbf{k}$ is a wave vector in frequency domain, which can be written as $\mathbf{k} = (k_x, k_y)$. $\mathbf{k}_m$ is the wave vector of the m-th illumination angle, which could be expanded as $\mathbf{k}_m = k\mathbf{s}_m = k(s_x^{(m)}, s_y^{(m)}, s_z^{(m)})$. The left hand side of Eqn. (4.1) could be rewritten as:

$$g_m = \frac{ks_z^m}{2\pi i}\int\int_{-\infty}^{\infty} U_0^{(m)}(\mathbf{r}')\ln\frac{U(\mathbf{r})}{U_0^{(m)}(\mathbf{r})}e^{-i(ks_x^{(m)}x+ks_y^{(m)}y)}dxdy \tag{4.4}$$

where $U_0^{(m)}(\mathbf{r})$ is the m-th illumination field, and $U(\mathbf{r})$ is the summation of the illumination electric field $U_0(\mathbf{r})$ and the field scattered by the sample $U_s(\mathbf{r})$. Similar to Eqn. (4.3), it also maps the electric field to a 2D Fourier space. In this way, we can linearize the forward model, however, the inverse problem is still difficult to solve since it may amplify the noise and the missing cone problem (missing axial frequency support at low lateral frequencies of the k-space) still exists [32,44]. To mitigate those problems, we usually introduce a regularization term in Eqn. (4.2) and the inverse problem becomes:

$$\hat{\mathbf{x}} = argmin_{\mathbf{x}}\sum_{m=1}^{N}\|A_m\mathbf{x} - g_m\|_2^2 + \alpha R(\mathbf{x}) \tag{4.5}$$

where α is the regularization coefficient, while $R(\mathbf{x})$ is the regularization term. This method is called regularized Rytov ODT.

It is important to note that the linear model presented is still inaccurate for most cases because it still assumes single scattering in the specimen. In order to account for multiple scattering, proper nonlinear forward models are needed to address the

multiple scattering problem. Beam propagation method (BPM) is a well-known approach that slices the 3D refractive index (RI) of a volume along z directions into $k = 1, 2, ..., K$ layers, resembling the structures of neural networks [45, 151]. The electric field between layers is propagated via linear mapping:

$$S_k(\mathbf{x}) = diag(p_k(x_k))HS_{k-1}(\mathbf{x}) \tag{4.6}$$

where $S_k(\mathbf{x})$ is the optical field of the k-th layer, and $diag(\cdot)$ is the operator to turn a vector into a diagonal matrix. H is diffraction operator that is simplified by Fresnel propagation, while $p_k(x_k) = \exp(ikx_k)\delta z$describes the refraction taking place in the k-th layer, where x_k is the refraction index map at the k-th layer and δz denotes the interval between layers. Then the inverse problem can be formulated as:

$$\hat{\mathbf{x}} = argmin_{\mathbf{x}} \sum_{m=1}^{N} \left\| S_K^{(m)}(\mathbf{x}) - g_m \right\|_2^2 \tag{4.7}$$

The strategy to solve this problem is based on gradient descent and back-propagation. Firstly, we calculated the gradient of the loss function by iterating along different layers, then we update the RI values of different layers $(x_k, k = 1, 2, ..., K)$ by applying TV regularization. This method is quite similar to training a neural network, therefore, the method is called Learning Tomography based on Beam Propagation Method (LT-BPM).

Among these ODT reconstruction algorithm, LT-BPM can retrieve the 3D RI maps with good accuracy. Here we reconstruct the 3D RI map of a polystyrene bead (RI ~ 1.595, diameter $\sim 10\mu m$) with Rytov ODT, Rytov ODT with regularization and LT-BPM, respectively, and evaluate their performances. The microbeads were immersed in the medium of oil with the RI of 1.56 and sandwiched with two No.1 coverslips. The 3D RI maps are reconstructed based on the interferograms acquired from 49 illumination angles by a home-built optical diffraction tomography system. Note that, LT-BPM method is initialized with Rytov ODT reconstruction results to accelerate the convergence. The comparison of the reconstruction results is shown

in Figs. 4-1 (a), (b) and (c), respectively. Noticeably, in regularized Rytov ODT and LT-BPM, the value of regularization coefficient α can be adjusted to balance between the data-fidelity term and the regularization term to denoise and to mitigate the missing-cone issues. Usually, this parameter tuning process is empirical. To fairly compare the 3D RI maps, the regularization coefficient α for both regularized Rytov ODT and LT-BPM is chosen to be 5×10^{-5}, and each algorithm (Rytov with regularization and LT-BPM) iterates for 50 timesteps.

In Figs. 4-1(d) – (e), we compared the lateral and axial cross-sections of the beads' RI profiles reconstructed by the three approaches. We see that Rytov ODT method without any regularization, despite its fast speed, incur two major artifacts: first, some of the region in the reconstruction has RI values lower than 1.56, which is impossible in real cases; second, the RI reconstructions incur visible elongation along the axial direction and the reconstructed RI values are smaller than they should be. We found that non-negativity constraint in Rytov or LT-BPM is sufficient to resolve the first type of artifacts. However, LT-BPM is better than the regularized ODT at mitigating that axial elongation artifact , as indicated in Fig. 4-1 (e). Since the regularized Rytov ODT and LT-BPM share the same regularization coefficient, we conclude that the improved performance resulted from the introduction of the nonlinear scattering model (beam propagation method). To further justify our claim, we imaged 100 polystyrene beads and calculated the MAE and RMSE between the ground truth and the RI maps reconstructed by the proposed three methods, and demonstrated the results in Figs. 4-1 (f) & (g), where we see for both MAE and RMSE, LT-BPM outperforms the other methods. Therefore, we are confident that LT-BPM is a more reliable approach for reconstructing the ground truth RI maps for composing the training dataset in DS-ODT.

4.1.2 Deep learning based computational imaging

To push ODT's imaging speed limit even further, data-driven approaches are perhaps necessary to compensate the severe information deficit of the reducing illumination

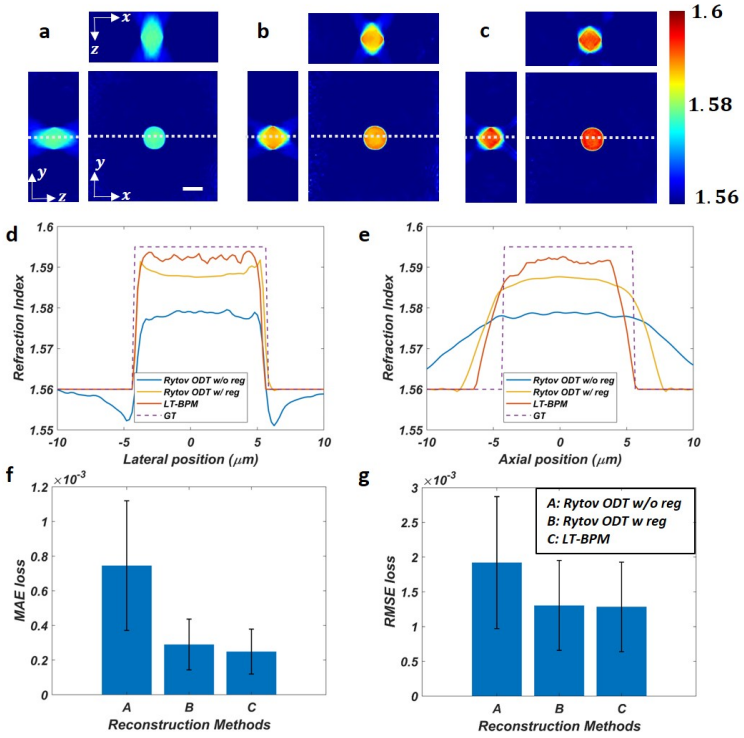

Figure 4-1: **The evaluation of micro-beads' RI maps reconstructed with different approaches.** We demonstrated 3D RI maps of a polystyrene bead reconstructed with (a) Rytov ODT approach, (b) Rytov ODT approach with TV regularization, and (c) LT-BPM, respectively. The plots of the 3D RI maps along (d) x-axis and (e) z-axis, respectively, of different reconstruction methods and the ground truth RI map. The quantitative evaluations of the (f) MAE, and (g) RMSE of the ground RI maps, and the ones obtained with different reconstruction methods' performance. The scale bar in (a) denotes 10 μm, while the while dashed lines show the positions where we plot the curves in (d) and (e).

angles. In particular, deep learning [153] has gained tremendous popularity in various applications of computational imaging, due to its versatility and fast inference when the machine learning model has been trained [154–157]. Recently, deep learning is also widely used in quantitative optical imaging as an important auxiliary method to solve inverse scattering problem, as shown in ref. [154]. These algorithms, typically in the supervised manner, during the training stage, learn from the examples the underlying relationship algorithms under many circumstances. During the testing stage, the trained machine learning engine is used to predict the unseen test examples from the test inputs. Some classical machine learning frameworks are often used for imaging- related applications, including U-Net [158], ResNet [159], etc.

One of the important imaging problems that deep learning approaches could solve is the phase retrieval problem under low-photon circumstances [160]. A multitude of phase retrieve methods can be used to recover the phase maps from defocused intensity measurements, such as the Gerchberg-Saxton (GS) and the gradient descent method. However, they may fail quickly when we decrease the illumination power. Another method is to train a DNN, which is based on U-Net and residual blocks as discussed, to directly predict the phase map from a noisy intensity measurements (end-to-end). However, in this case, the DNN will not only overcome the shot noise, but would also be required to learn the Fresnel propagation law, which may require a lot of data and many training epochs. The most efficient way is to use GS algorithm to generate an approximant of the phase map, then pairing this approximant and the ground truth phase maps and feed to the DNN for the training, which is also called phase-informed method. Examples [161] have also shown that physics-informed deep learning algorithms, where the known physics knowledge has been incorporated into the machine learning algorithm, typically as a pre-processing step, are generally much more efficient than the physics-blind counterparts, where the machine learning engine is used as a black-box to directly learn the map from the input to the output.

Similarly, in the development of high-speed ODT, one of the most efficient methods is reducing the illumination angles. However, fewer illumination angles will cause the information deficit, which deteriorates the imaging quality of 3D RI maps. The missing information could be learned from training dataset with deep learning approach, however, the end-to-end approach will require a lot of data and many training epochs. Therefore, physical-informed deep-learning approach is applied here by implementing a crude phase estimation step, in order to increase the training efficiency. The details of this technique will be elaborated in following sections.

4.2 Principles of Deep-learning Single-shot Optical Diffraction Tomography (DS-ODT)

Based on the aforementioned ODT techniques with angle-multiplexing hardware and a deep-learning based image reconstruction model, we developed DS-ODT that achieves high-resolution single-frame 3D cell imaging. The principles of DS-ODT will be elaborated in this section, and more details will be covered in our coming publications.

4.2.1 Overall pipeline

The overall pipeline of Deep-learning Single-shot Optical Diffraction Tomography (DS-ODT) is introduced and shown in Fig.4-2. As in Fig.4-2(a), the four-angle-multiplexed interferogram captured by an angle-multiplexing ODT system incorporating a high-speed CMOS camera (over 10,000 fps) is input to DS-ODT algorithm for 3D RI map reconstruction. Firstly, the crude phase maps are estimated from the interferogram based on spectral filtering; then 3D RI map is predicted from the crude phase maps using the trained Machine Learning engine (ML engine).

The training of the ML engine is elaborated in Fig.4-2(b). We prepare a training dataset, where the input is the crude phase maps estimated from the four-angle-multiplexed interferograms; while the ground truth RI maps are produced by LT-BPM [45,151], based on the 49 true phase maps, each extracted from the single-angle interferogram corresponding to each illumination angle.

The main architecture of Machine Learning engine (ML engine) is the generalization of the Learning to Synthesize by DNN (LS-DNN) [162] to 3D, which is intended to improve the spatial resolution of the output 3D RI maps. Moreover, to better preserve the fine features, the Negative Pearson Correlation Coefficient (NPCC) [161] is used as our training loss function. After the ML engine has been trained, it is used to predict RI maps from the multiplexed interferograms of unseen cell samples.

Thanks to the use of angle-multiplexing ODT system, high-speed CMOS camera and deep learning, DS-ODT achieves the 3D imaging speed that few existing method

could rival, still with submicron spatial resolution. Single-frame 3D imaging is realized by angle-multiplexing ODT technique combining four illumination angles in one snapshot interferogram, while the trained ML engine learned the missing information from the training data so that the four-angle RI reconstruction could have similar performance as their counterparts reconstructed with ~ 50 angles. The utilization of high-speed CMOS camera further pushes the 3D imaging speed to over 10,000 fps; at the same time, the inference time of our ML engine is negligible. The details of angle-multiplexing ODT hardware along with the crude phase estimation and machine learning engine that constitutes DS-ODT algorithm will be elaborated in following sections.

4.2.2 Angle-multiplexing ODT

DS-ODT utilizes a novel optical system design multiplexing multiple illumination angles in one interferogram, which is termed angle-multiplexing ODT. Angle multiplexing is achieved by overlapping multiple Lee hologram patterns on the first DMD (D1), as shown in Fig. 4-3. As we have validated our deep learning-based algorithm can learn the missing information from the training data so that the four-angle RI reconstruction could have similar performance as their counterparts reconstructed with ~ 50 angles, we overlapped four incident angles' Lee hologram patterns on DMD. TThe angle multiplexed interferogram generated by the four incident light beams can be transformed to the spatial frequency domain as shown in Fig. 4-3(b).

The detailed optical system design of angle-multiplexing ODT is shown in Fig.4-3. A 532 nm laser (Changchun New Industries Optoelectronics Technology, MGL-III-532-300mW) is used as the illumination source and the laser beam is divided into two beams by a 1×2 single-mode fiber coupler (SMFC), of which one beam is used as the sample beam, while the other serves as the reference for interferometric detection. The sample beam is collimated by a lens L1 (f1 = 200 mm), then impinging onto DMD D1 (Texas Instruments Inc., DLP LightCrafter 9000) which is programmed for displaying Lee hologram patterns to generate multiple illumination angles. Lens L2 (f2 = 150 mm) enables these reflected beams to form a series of diffraction spots at the Fourier

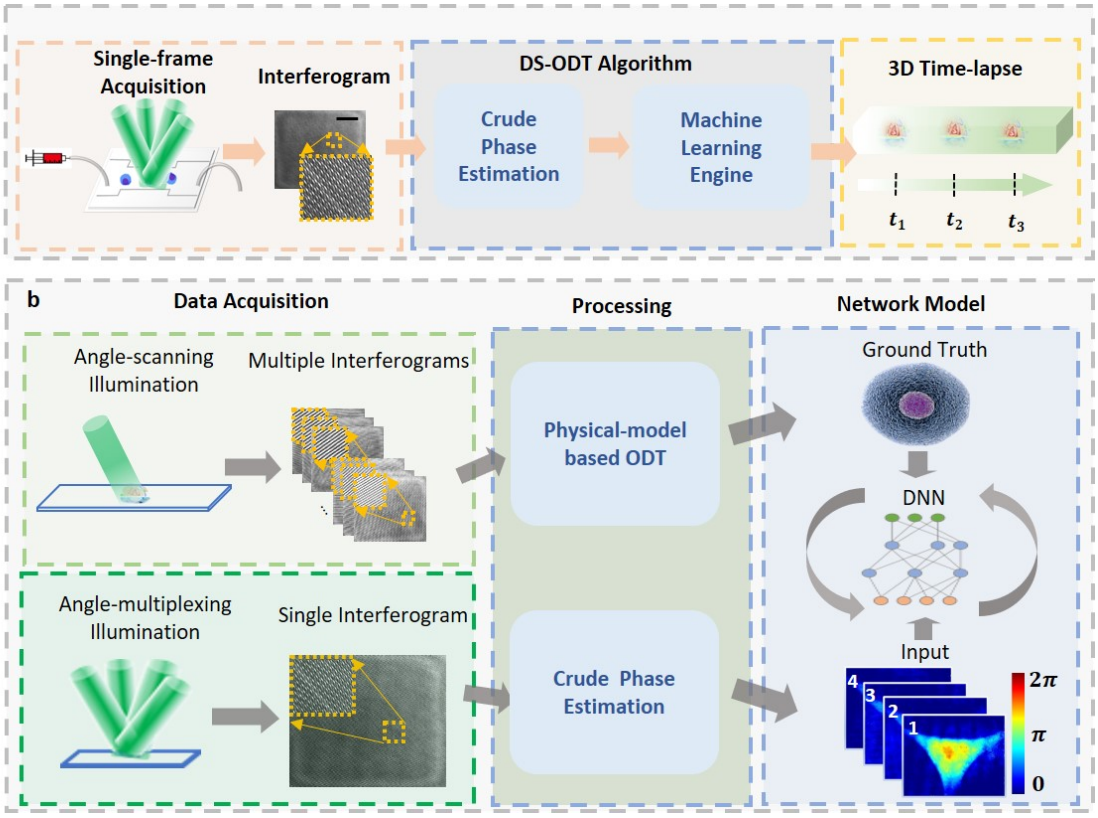

Figure 4-2: **The pipeline of DS-ODT.** (a). The pipeline of 3D RI time-lapse video reconstruction with DS-ODT algorithm, which consists of the following two primary steps: crude phase estimation and inference with trained machine learning engine. (b). The training process of the machine learning engine. The upper part demonstrates the preparation of ground truth RI maps: the RI maps are produced by the physical-based ODT reconstruction algorithm (LT-BPM) from all 49 interferograms captured with angle-scanning illumination. The lower part of (b) shows the input to the training is the four crude phase maps estimated from the angle-multiplexed interferogram of the same training sample.

plane, where the second DMD2 (Texas Instruments Inc., DLP LightCrafter 6500) is placed. The filter mask patterns shown in the inset 1 of figure is loaded onto DMD2 to block the extraneous diffraction orders and only allow the desired 1^{st} diffraction order to pass along the excitation path. Next, the filtered beam is reflected by mirror M1 and collimated by lens L3 (f3 = 200 mm). Followed by a 4f system composed of a tube lens L4 (f4 = 300 mm) and objective lens OL1 (Zeiss, 63X/1.3, water immersion) which used to magnify the angle range of the sample beam. Afterward, the sample beam illuminates the sample to generate the scattered light which carries the sample

structural information and collected by the objective lens OL2 (Zeiss, 63X/1.25, oil immersion) and lens L5 (f5 = 150 mm). A beam splitter (BS) is put behind the lens L5 to combine the sample and the reference beam for forming the interferogram which is recorded by a high-speed camera (Photron, Fastcam SA-X2) after passing through the last 4f system consists of lens L6 (f6 = 60 mm) and L7 (f7 = 400 mm).

4.2.3 Crude phase map estimation

After the four-angle-multiplexed interferogram is captured, the next step is retrieving the phase maps of each illumination angle with spectral filtering method. This step informs physical model information to the deep-learning model and is essential for improving the training efficiency and decreasing the size of dataset. It worth noticing that the scattered fields' information of each incident angle is coupled together, therefore, the direct linear filtering inevitably causes frequency missing or aliasing. That is why we called the phase maps retrieved after this spectral filtering step as 'crude phase maps'. The specific procedure for crude phase estimation is elaborated below. We applied the spatial Fourier transform to the angle-multiplexed interferogram, and the amplitude of the Fourier space is shown in Fig. 4-3 (c). In the 0^{th} order (the center region of the Fourier space), we can see nine bright spots, where the center one is the DC term, while the other 8 spots come from the interference between sample beams from different illumination angles. In the $+1^{st}$ and -1^{st} orders (diagonal regions of left-down and right-up), the four bright spots are originated from the interference between the four sample beams coming from each incident beam and the reference beam and are labeled with red spots in Fig. 4-3 (b). To extract the phase maps of the 4 illumination angles separately, four spectral filters matching the four angles are applied to the $+1^{st}$ order, as shown in Fig. 4-3 (c). The gray region denotes the contour of $+1^{st}$ order that has been shifted to the center of the Fourier domain; the unfiltered regions that correspond to each incident angle, are labeled white in each spectral filter. The retrieved crude phase maps are also shown in Fig. 4-3(c).

Balancing between the needs to retain high-frequency components and to minimize

the spectral aliasing,the pass bands of the spectral filters are carefully adjusted. Here we use the size of the numerical aperture of the objective (NA) on the Fourier space as the unit to calculate the size of our spectral filters. The numerical aperture of the objective is 1.2, which means the spatial frequency of 1 NA on the Fourier space is $1.2/\lambda$. In Figs. 4-3 (d)-(e), we show the PCC, MAE of the crude phase maps and true phase maps when the filter size equals 0.3 NA, 0.5 NA and 0.8 NA, respectively. We can see the relatively larger filter size will deteriorate the accuracy of the crude phase maps, due to the aliasing problem. However, the retrieval accuracy of 0.5 NA filters is just slightly better than that of 0.3 NA filters, which means the percentage of the high frequency components of our specific imaged samples is not significant. Here we choose the filter size to be 0.5 NA.

To describe our crude phase estimation method more rigorously, the procedures of decoupling crude phase maps from the multiplexed interferograms can be mathematically formularized as following. The interference between the multiplexed N-angle illuminated sample beam and the reference beam satisfies :

$$\begin{aligned} I_{multiplex} &= \left| \sum_{m=1}^{N} E_S^{(m)} + E_R \right|^2 \\ &= |E_R|^2 + \sum_{m=1}^{N} \left| E_S^{(m)} \right|^2 + \sum_{m=1}^{N} \left\langle E_S^{(m)}, E_R \right\rangle + \sum_{i,j(i\neq j)} \left\langle E_S^{(i)}, E_S^{(j)} \right\rangle \end{aligned} \tag{4.8}$$

where E_R is the reference electric field, which is actually a plane wave and $E_S^{(m)}$ is the electric field scattered by the sample with the m-th illumination angle. Here, the bracket $\langle \cdot \rangle$ denotes the correlation function, which could explain the interference between electric fields. In the second row of Eqn. (4.8), the third term denotes the interference between the scattered beam and the reference beam, which is shown in the $+1^{st}$ and -1^{st} order in the Fourier domain. If we expand this term, we can obtain the following expression.

$$\sum_{m=1}^{N} \left\langle E_S^{(m)}, E_R \right\rangle = \sum_{m=1}^{N} \left| E_S^{(m)}(\mathbf{r}) \right| |E_R| \cos\left((\mathbf{k}_S^{(m)} + \mathbf{k}_R) \cdot \mathbf{r} + \Delta\phi^{(m)}(\mathbf{r}) \right). \tag{4.9}$$

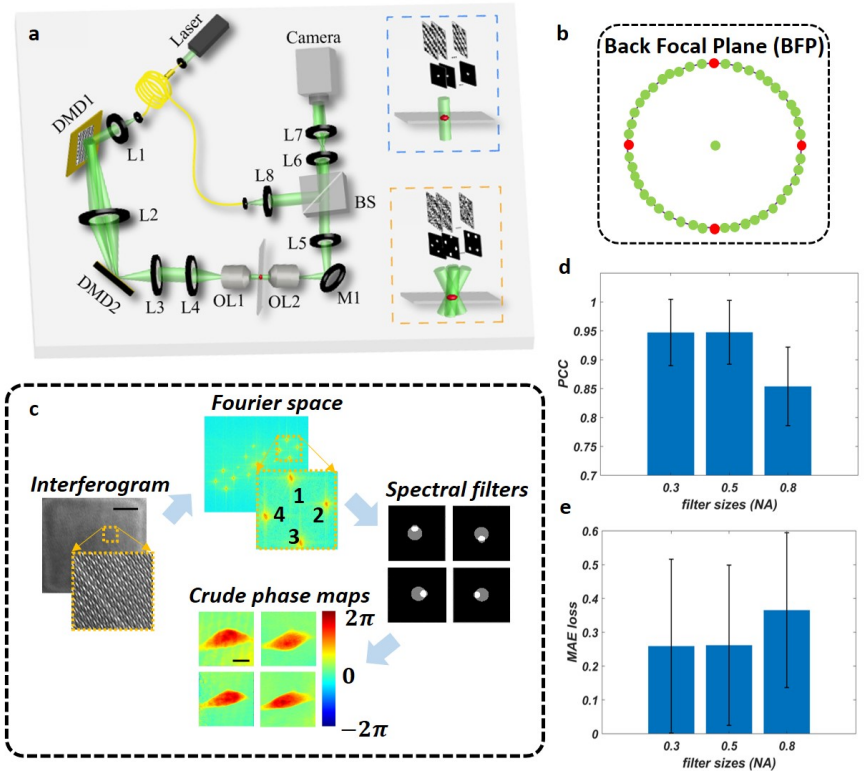

Figure 4-3: **The system design of DS-ODT, and the estimation of the crude phase maps (spectral filtering method).** (a) The schematic diagram of our experimental setup of the DMD-based ODT system. (b) the demonstration of the illumination angles' pattern on the back focal plane (BFP) of the objective. The green dots show the illumination angles for angle-scanning scheme, while the red dots show the illumination angles used for angle-multiplexing scheme. (c) The pipeline of the spectral filtering method. (d)-(e), the PCC and MAE of the crude phase maps (according to the true phase maps), respectively. The scale bar denotes 20 μm.

where $\mathbf{k}_S^{(m)}$ is the wave-vector of the scattered field of the m-th illuminated angle, while $\mathbf{k}_R$ is wave vector of the reference beam. Taking only the $+1^{st}$ order and performing the spatial Fourier transform:

$$\tilde{I}_{+1}(\mathbf{k}) = |E_R| \sum_{m=1}^{N} \Im \left[\left| E_S^{(m)}(\mathbf{r}) \right| \exp\left(i\Delta\phi^{(m)}(\mathbf{r})\right) \right] * \delta(\mathbf{k} - \mathbf{k}_S^{(m)} - \mathbf{k}_R) \tag{4.10}$$

where $\tilde{I}_{+1}(\mathbf{k})$ denotes the $+1^{st}$ order in Fourier domain, while $\Im[\cdot]$ is the Fourier transform operator, and $*$ denotes 2D convolution. For the m-th illumination angle,

the original point in k-space is shifted to the position $\mathbf{k}_S^{(m)} - \mathbf{k}_R$. 'Therefore, we can see four bright points on the 1^{st} order of the Fourier domain. However, in the actual measurement, the numerical aperture of objective lens is limited, so we need to add a pupil function before Eqn. (4.10). Then we can obtain the Fourier domain of the real measurement:

$$\tilde{I}_m(\mathbf{k}) = P(\mathbf{k} - \mathbf{k}_R) \cdot \tilde{I}_{+1}(\mathbf{k}) \tag{4.11}$$

where $P(\mathbf{k}-\mathbf{k}_R)$ is the pupil function defined as following: $P(\mathbf{k}) = 1$ when $|\mathbf{k} - \mathbf{k}_R| \leq k_c$; and$P(\mathbf{k}) = 0$ when $|\mathbf{k} - \mathbf{k}_R| > k_c$, where $k_c = \frac{2\pi}{\lambda} NA$ is the cutoff frequency of the pupil function, and λ is the wavelength and NA is the numerical aperture of the objective. The frequency domain profiles of the total N illumination angles are overlapped, and cannot be completely separated by linear fitting. However, if the distributions of the N illumination angles are represented in the frequency domain, the contributions from the different angles may still separable without severe aliasing (if N is not too large). For the m-th illumination angle, the filtering process satisfies:

$$\begin{aligned} \hat{E}_S^{(m)}(\mathbf{r}) &= \left| \hat{E}_S^{(m)}(\mathbf{r}) \right| \exp\left(i(\Delta\hat{\phi}^{(m)}(\mathbf{r}) + (\mathbf{k}_R + \mathbf{k}_S^{(m)}) \cdot \mathbf{r}) \right) \\ &= \Im^{-1}\left[p^{(m)}(\mathbf{k} - \mathbf{k}_R - \mathbf{k}_S^{(m)}) \cdot \tilde{I}_m(\mathbf{k}) \right]. \end{aligned} \tag{4.12}$$

where $\hat{E}_S^{(m)}(\mathbf{r})$ is the estimated complex field, and $\Im^{-1}$ is the inverse Fourier transform. $p^{(m)}(\mathbf{k} - \mathbf{k}_R - \mathbf{k}_S^{(m)})$ is the linear filter which could decouple the information of the m-th illumination angle, which is defined by $p^{(m)}(\mathbf{k}) = 1$, when $\left| \mathbf{k} - \mathbf{k}_R - \mathbf{k}_S^{(m)} \right| < k_f$, where k_f is the cutoff frequency of the filter. The choice of k_f represents a trade-off: a larger k_f value could improve the resolution of the retrieved phase map, while introducing more severe aliasing; whereas, a smaller k_f helps reduce aliasing at the cost of more loss on high spatial frequencies. With an additional measurement of the background, the same field of view without sample, (its Fourier transform of the $+1^{st}$ order is represented as $\tilde{I}_{BG}(\mathbf{k})$), the retrieved phase maps of the m-th illumination

angle can be calibrated as:

$$\begin{aligned}\Delta\hat{\phi}^{(m)}(\mathbf{r}) = &\angle\left[\Im^{-1}\left[p^{(m)}(\mathbf{k}-\mathbf{k}_R-\mathbf{k}_S^{(m)})\cdot\tilde{I}_m(\mathbf{k})\right]\right] \\ &-\angle\left[\Im^{-1}\left[p^{(m)}(\mathbf{k}-\mathbf{k}_R-\mathbf{k}_S^{(m)})\cdot\tilde{I}_{BG}(\mathbf{k})\right]\right]\end{aligned} \tag{4.13}$$

where $\angle$ denotes the phase of a complex field. These phase maps retrieved from multiplexed illumination angles are termed 'crude phase maps'. In our angle-multiplexing ODT system, we choose the total number of multiplexed illumination angles to be $N = 4$, which are uniformly distributed along the outer circle on the back focal plane (BFP) of the objective lens. These four angles have the same titling angle (60°), and the azimuthal angle interval between the adjacent two illuminations angles is 90 degree. This arrangement is designed to minimize the aliasing between the illumination angles. As we discussed before, in our work, the value of k_f is chosen to be $0.5k_c = 0.5 \times \frac{2\pi}{\lambda} \times NA$, as it best keeps the balance between preserving high-frequencies and avoiding aliasing. However, even if there is information loss, the crude phase estimation still provides with enough prior physical information for efficient training efficiency improvement and will be discussed further in following sections.

4.2.4 Machine learning engine

After the crude phase maps are estimated with spectral filtering method, they will be fed to our trained machine learning engine (ML engine) as input to predict the output 3D RI map, as shown in Fig. 4-2 (a). While providing physical information via the crude phase map estimation can improve training efficiency, the training strategy itself is also critical. The training dataset is consisted of 900 pairs of inputs (four crude phase maps estimated from a single-shot interferogram) and ground truth (3D RI map reconstructed from 49 true phase maps with LT-BPM) of NIH/3T3 cells, from which we took 5% data as validation dataset. Besides, we took another $\sim$ 40 pairs of inputs and ground truths for testing. This training dataset is not large, however,

with our physical-informed deep learning approach and proper training strategies, it could still acquire good testing performance and generality, which we will elaborate in following sections.

The basic architecture of our machine learning engine is the residual U-Net block shown in Figs. 4-4 (a) & (b), where we see that canonical U-Net consists of multiple down residual blocks (DRB), gradually extracting features from the input, followed by several up residual blocks (URB) to scale the feature maps up to the correct size. Skip connections are proven beneficial for the spatial resolution of the reconstructions. In the meanwhile, we use residual blocks in the U-Net to stabilize training and avoid gradient exploding/vanishing when the network depth is large [159].

Since the task of our machine learning engine is 3D image reconstruction, the regular

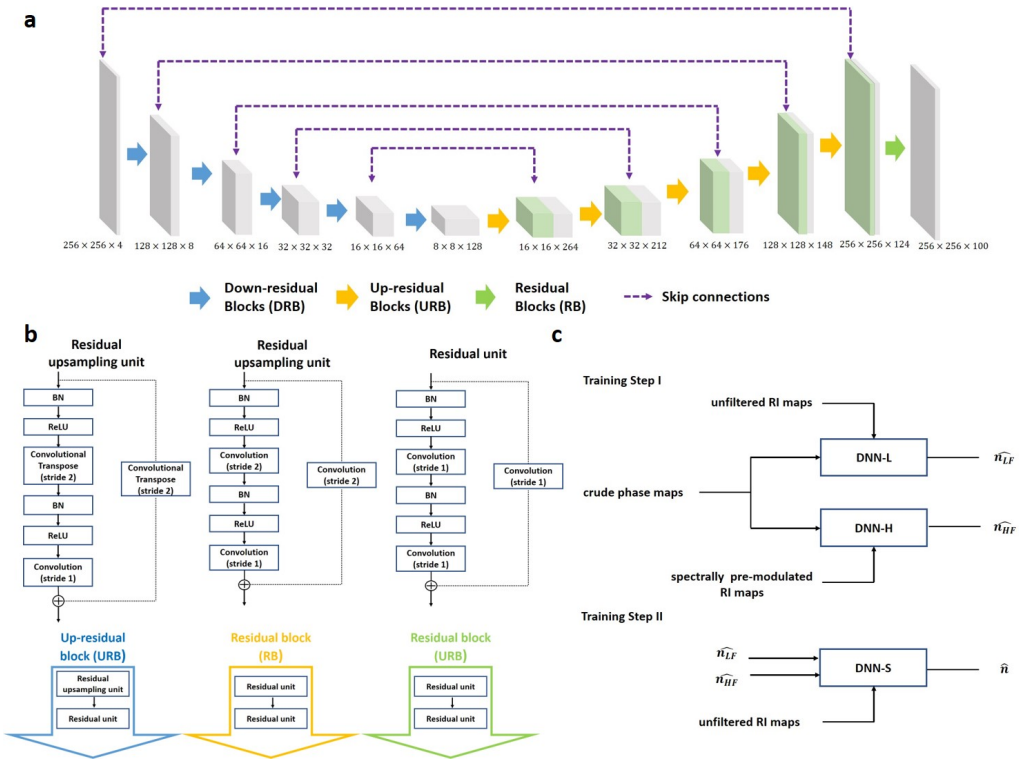

Figure 4-4: **The machine learning engine.** (a) the general structure for the residual U-Net. (b) detailed structures for Down-residual Blocks (DRB), Up-residual Blocks (URB) and Residual Blocks (RB). (c). The two-step training process for LS-DNN.

training loss functions, i.e., mean square error (MSE), mean absolute error (MAE), may not able to obtain satisfactory performance as the correlation between different

pixels is ignored. Therefore, our neural network is trained with negative Pearson Correlation Coefficients (NPCC), defined as

$$NPCC(y,\hat{y}) = -\frac{\sum_{i=1}^{N}(y_i-\bar{y})(\hat{y}_i-\bar{\hat{y}})}{\sqrt{\sum_{i=1}^{N}(y_i-\bar{y})^2\sum_{i=1}^{N}(\hat{y}_i-\bar{\hat{y}})}} \tag{4.14}$$

where y and $\hat{y}$ are the ground truth and output of the neural networks and i indexes the pixels. NPCC loss function is chosen since it is proven to be more efficient in reconstructing fine features [161], however, since NPCC is constant under any affine transformation, i.e. , $NPCC(y,\hat{y}) = NPCC(y, a\hat{y}+b)$ for all a, b. Therefore, to make sure that the reconstructions are accurate, we need to calibrate the raw output of the neural network $n_{out}(x,y)$ with the linear fitting:

$$n_{estimate}(x,y) = \alpha_1 n_{out}(x,y) + \alpha_2, \tag{4.15}$$

where $n_{estimate}$ is the estimated RI map and α_1, α_2 are the linear coefficients estimated from the minimum mean-square-error linear fitting of the raw output of the machine learning engine with the ground truth, based on the validation database. To further justify our choice of training loss function, we compare the testing loss of NPCC and MAE loss functions, in terms of quantitative metrics (PCC, MAE and RMSE) in Fig. 4-5. We see that, all others factors being same, NPCC as the training loss function gives us the best reconstructions. Therefore, the use of NPCC as the training loss function, despite the need for a further step of linear fitting, is justified.

It is worth noticing that the testing loss of RBCs are even worse than the results of other species when the ML engines is trained with both loss functions. That is because the training data set only has the images of NIH/3T3 cells, which is an eukaryotic cell species; however, the RBCs don't have any intracelluar structures, such as nuclei, organelles, etc. However, even so, the PCC test loss of RBCs are still larger than 0.85, which still validate that our DS-ODT method is reliable.

However, even if the aforementioned training method can obtain satisfactory quantitative evaluation results, as shown in Figs. 4-5 and 4-6, the deficiency of high frequen-

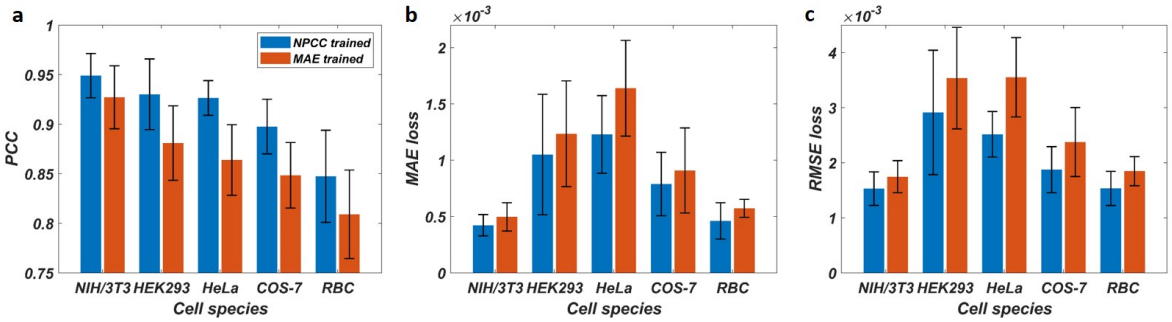

Figure 4-5: **Quantitative evaluation of DS-ODT's reconstruction with different training loss metrics.** (a)-(c), the PCC, MAE loss, and RMSE loss of the ground truth RI map (LT-BPM reconstruction with 49 angles) and the RI map reconstructed with our trained DNN on the dependence of different cell species, respectively. The DNN model used for producing the RI map is trained with dataset of NIH/3T3 cells. The blue bars show the results of the DNN trained with NPCC loss function, while the red bars demonstrate the results of the MAE loss function trained DNN model.

cies in the reconstructions is still observed, as the reconstructions of many machine learning algorithms. This phenomenon will reduce the reconstructed image's spatial resolution and jeopardize the visualization of many intracellular structures. To compensate for this deficiency, we adopted the training strategy called Learning-to-synthesize by DNN (LS-DNN) [162] and extend it to 3D case.

The first step is pre-modulating the ground truth 3D RI maps to extract their high-frequency bands. We empirically choose the high frequency band of the training examples in the following manner: let $n(x, y, z)$ be the 3D refractive index profile with the understanding that z is the distance to the middle of the computational window in z direction. In DS-ODT, the ground truth RI map reconstructed by LT-BPM have 100 layers along z-direction in total, and the interval between layers is $\sim 0.2\mu m$. The central layer is the focal plane where we denote as $z = 0$, and the cell is usually located in the region near the focal plane (i.e $|z| \leq 40$ layers or $8\mu m$). In the cell region, most of the organelles are located at layers $|z| \leq 30$, where we have both low frequencies and high frequencies; and at layers $30 < |z| \leq 40$, we have the boundaries (membranes) between the cell and medium, where contains more high frequencies. In the layers $|z| > 40$, we don't have any useful information, so the modulation is not necessary. The boundary locations (i.e $z = 30, z = 40$) are based on

our observation of the ground truth dataset, and empirically selected to maximize the high-frequency band recovery. Thereafter we let $F(n(x,y,z))$ be the Fourier transform of $n(x,y,z)$. We specially design the high-pass filters $M(k_x,k_y;z)$ per our prior knowledge about the ground truth RI map, and the filtered examples $\tilde{n}(x,y,z)$ have Fourier transform $F(\tilde{n}(x,y,z)) = F(n(x,y,z))M(k_x,k_y;z)$,where the spectral filter $M(k_x,k_y;z)$ satisfies:

1. $M(k_x,k_y;z) = (k_x^2+k_y^2)^{1.5}$ for $|z| \leq 30$;

2. $M(k_x,k_y;z) = (k_x^2+k_y^2)^{0.8}$ for $30 < |z| \leq 40$;

3. $M(k_x,k_y;z) = 1$ for $|z| > 40$.

Thereafter, we trained two additional DNNs. As shown in Fig. 4-4(c), along one bench, a DNN is trained to emphasize high frequency signal, i.e. DNN-H, which is trained with spectrally pre-modulated examples where the high frequencies are amplified. This results in reconstructions of the high-frequency band to be reliable, but not the low-frequency band. On the other hand, in the low-frequency branch, where DNN-L, or DNN-low, is trained with unfiltered examples and therefore the reconstructions are reliable in the low-frequency band but not the high-frequency band. At the second step in training, we use a third DNN, termed DNN-S, or DNN-synthesizing, to learn to synthesize the preliminary reconstructions from DNN-L and DNN-H, so that the final reconstruction is of high fidelity in all frequencies [162, 163]. After applying LS-DNN strategy, our reconstructed 3D RI maps not only have great quantitative evaluation results, but also manifests enough details and fine structures in 3D, as shown in Fig. 4-7 and Fig. 4-8.

4.3 Validations for Deep-learning Single-shot Optical Diffraction Tomography (DS-ODT)

4.3.1 Quantitative evaluations based on different schemes

After demonstrating the principles of DS-ODT, we need to evaluate its performance. To quantitatively demonstrate the effectiveness of the DS-ODT algorithm, we first compare the reconstruction quality and the time-cost, of the following three schemes: LT-BPM, Multi-frame Deep-learning ODT (MDODT), and the DS-ODT. LT-BPM is a physical-model based ODT algorithm; MDODT is deep learning based ODT but not using angle-multiplexing; DS-ODT is our proposed method that combining angle-multiplexing ODT system and deep learning algorithm. The time-cost is evaluated with acquisition time that is indicated by the number of image acquisitions, denoted by K, while the reconstruction quality is manifested with the Pearson Correlation Coefficient (PCC), Mean Absolute Error (MAE) and Root Mean Square Error (RMSE) compared against 49-angle LT-BPM reconstructions (ground truth), as shown in Fig. 4-6 (a). Noting that usually K acquisitions are based on K illumination angles that are individually captured. The only exception is in LT-BPM and DS-ODT, when K equals 1, it corresponds to one interferogram that is multiplexed with four illumination angles.

The details of each 3D RI reconstruction scheme will be elaborated as following.

Firstly, LT-BPM reconstructions based on K acquisitions. In this scheme, interferograms based on K illumination angles are individually captured. The LT-BPM algorithm takes in these K phase maps, where each is extracted from the corresponding single-angle interferogram, and produces the final reconstructions iteratively. Since the phase estimation from the single angle interferograms is highly reliable, we will refer to phase maps thus estimated as true phase maps.

Multi-frame deep-learning ODT (MDODT) with K illumination angles. The data acquisition process is identical to that in the scheme I, but a machine learning engine is trained to map K true phase maps to 3D refractive index (RI) maps. It costs the

same acquisition time as that of LT-BPM for the same K. Though the training may take a few hours, the inference time is negligible once the network has been trained. Note that here, for K = 1, it refers to the scenario where only the normal incident illumination is used.

DS-ODT, where the input to the pipeline is the single-shot angle-multiplexed interferogram based on 4 uniformly spaced illumination angles (but only 1 acquisition). The machine learning engine is trained to produce 3D RI maps from the crude estimation of the four individual phase maps.

From Fig. 4-6 (a), we see that the reconstruction quality of LT-BPM degrades significantly as K, or equivalently, the acquisition time decreases; whereas in MDODT, this bottleneck is largely overcome by the introduction of machine learning – the reconstructions based on K = 4 is almost indistinguishable from that of K = 32. Therefore, the use of machine learning, besides its advantage in inference speed, is well justified as it enables as good reconstructions with much fewer number of illumination angles, and thereby, much shorter acquisition time. Moreover, in DS-ODT, the further reduction of acquisition time does not sacrifice the reconstruction quality much; namely, the DS-ODT reconstruction is close to that of MDODT when K = 4, while reducing the acquisition time by a factor of 4; and it outperforms MDODT for K = 1 (the normal incident as the only illumination angle), where the data acquisition time is the same. Based on the above comparison, we conclude that DS-ODT achieves the best compromise between imaging speed and reconstruction quality.

Subsequently, we evaluated the generalization ability of the DS-ODT algorithm, where the DS-ODT model trained on $\sim$ 900 NIH/3T3 cells is used to predict the RI maps of other cell species. Quantitative evaluations, where predicted RI maps are compared to the ground truth produced by the 49-angle LT-BPM, are conducted and shown in Fig. 4-6 (b). From the test results, we can see even if the training dataset only contains one cell species (900 input-ground truth pairs), the generalization performance on other eukaryotic cell species (HEK293T, HeLa, COS-7 cells) is quite good and therefore, we are confident in the generalization ability of the DS-ODT algorithm.

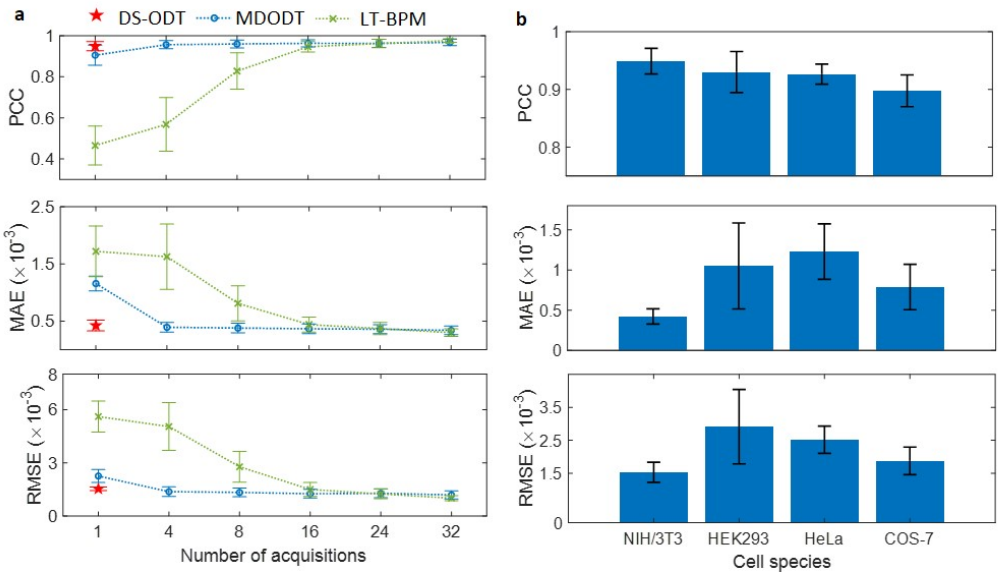

Figure 4-6: **Quantitative evaluation of DS-ODT's performance.** (a), the comparison of the performance (PCC, MAE, and RMSE) of LT-BPM, MDODT and DS-ODT as the function of the number of acquisitions K. (b) the generalization performance (PCC, MAE and RMSE) of the DS-ODT model trained on NIH-3T3 on various cell species.

4.3.2 Visualized results of other species of cells

In Fig. 4-7, we show examples of the predicted 3D RI maps of various cell species by our Learning-to-Synthesize (LS) enhanced DS-ODT trained on NIH/3T3. Specifically, the center x-y cross-section, the x-y sections that are $\pm 1\mu m$ apart from the center x-y cross-section and the y-z section are shown, along with the 3D rendering of the RI map. From Fig. 4-7, the chromosomes, the nuclei's boundaries, and other organelle's profiles are readily distinguishable from the focal plane of the reconstructed 3D RI map, indicating high spatial resolution and good reconstruction quality. of NIH/3T3 cells, HEK293T cells, and COS-7 cells are shown.

In Fig. 4-8, we show further comparison of reconstructions by LT-BPM with the same four illumination angles, DS-ODT, LS-DNN enhanced DS-ODT and the ground truth (generated by LT-BPM with all 49 illumination angles). From the comparison, we can clearly see that LS-DNN enhanced DS-ODT enables best reconstructions for all classes of cells.

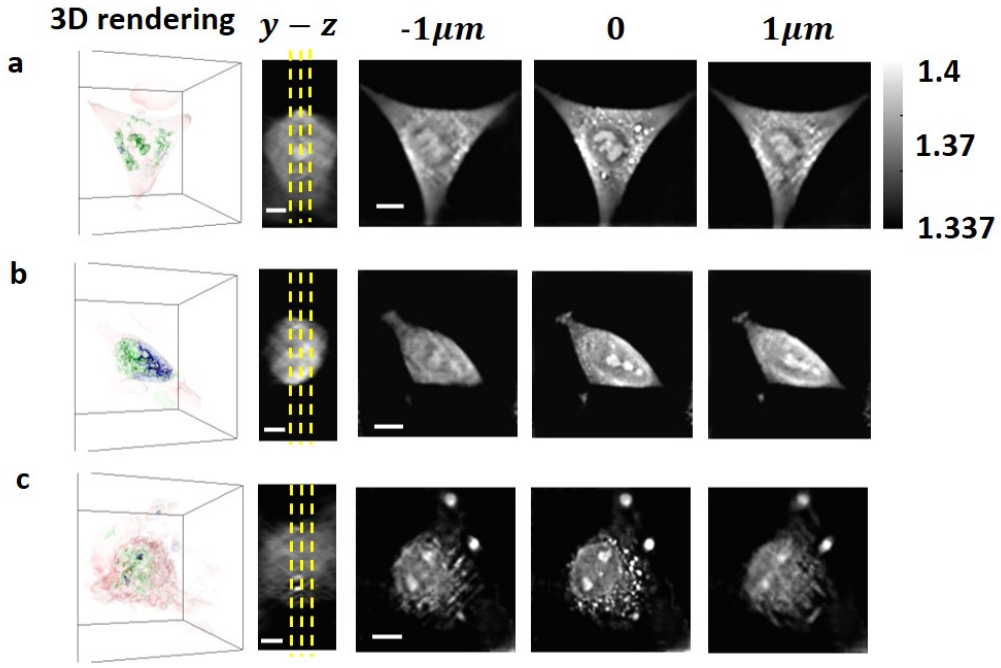

Figure 4-7: **The visualized comparison of trained Machine Learning engine's predicted RI maps of (a) NIH/3T3 cells, (b) HEK293T cells, and (c) COS-7 cells.** The 3D rendering of the RI maps is shown in the first column, where the RI value of the surfaces labeled with red, green, and purple equals 1.345, 1.370, and 1.389, respectively. The second column shows the y-z cross-sections of the 3D RI map; and the z locations of $z_0 - 1\mu m$, z_0 and $z_0 + 1\mu m$ are also shown with yellow dashed lines, where z_0 indicates the focal plane. The x-y cross-sections at different z locations are shown in the 3^{rd}, 4^{th}, and 5^{th} columns. The scale bar in the x-y plane is $10\mu m$ and the scale bar along z axis is $2\mu m$.

4.4 Imaging cellular dynamic events with DS-ODT

4.4.1 Visualization of red blood cell (RBC) demonstration

After validations in the previous sections, we demonstrate DS-ODT in more challenging applications by observing deformation of RBCs in microfluidics channels under high flow rate. In particular, observing the red blood cells' (RBCs) shape change dynamically in a high shear region in a microfluidic channel could reveal the mechanical properties of the RBCs that are important as biophysical biomarkers for studying the etiology of several blood diseases [164, 165]. Because most of the previous RBC studies used 2D phase imaging with only a few exceptions, morphological changes of RBC during shear flow have not been previously explored. In this section, we

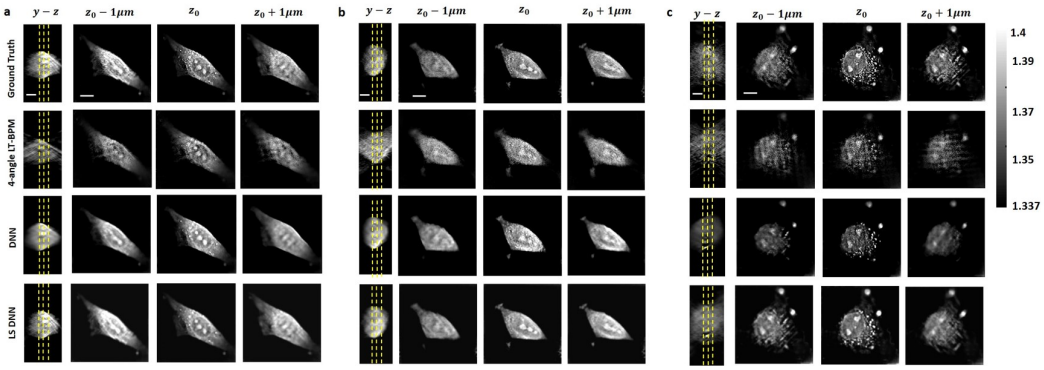

Figure 4-8: **Comparison of visualized results with different reconstruction methods.** The y-z cross-sections, and the x-y cross-sections at the z locations of$z_0 - 1\mu m$, z_0 and $z_0 + 1\mu m$ of (a)NIH/3T3 cells, (b) HEK293 cells and (c) COS-7 cells are shown, where z_0 indicates the focal plane. The different z locations are also labeled with yellow dashed lines in y-z cross-sections. The scale bar in the x-y plane is $10\mu m$ and the scale bar along z axis is $2\mu m$.

demonstrate the 3D imaging of red blood cells' (RBCs) deformations in a custom designed microfluidic channel. The single-frame 3D imaging of RBCs' deformation in a custom designed microfluidic channel is shown in Fig. 4-9. Fig. 4-9 (a) displays the specially designed microfluidic channel whose width in x-y dimension changes from wide to narrow, so that the shear rate is turning from low to high when the cells flow through it. With a 2 $\mu l/min$ flow rate and 10,000 fps acquisition speed, the entire process of RBC deformation in the transition part is captured, and the time-lapse video of 3D RI maps are reconstructed with our DS-ODT algorithm. In Fig. 4-9(b), we show the 3D volumetric rendering of the deformed RBCs' RI maps, along with the transition part of the microfluidic channel, at selected time points. To quantitatively analyze the 3D deformation of the RBCs flowing through the transition part, we firstly used an ellipsoid to fit the 3D morphology of the RBC, whose lengths of principal axes are defined as a, b and c, and a is the length of the longest principal axis. We define 3D eccentricity as $\eta = a/\sqrt{a^2 + b^2}$. In Fig.4-9 (c), we demonstrate the 3D eccentricity's variation of a particular cell example over time in the transition region of the microfluidic channel. The 3D volumetric rendering of this cell's RI map evolution is also quantified at several time points. From the rendered 3D shape of the RBC sample, we see that it is slightly elongated along its principal axis, and that its

longest principal axis changes from y-axis to x-axis. In the meanwhile, the increase of the 3D eccentricity also indicates the elongation of the cell when it flows through the transition region with the increasing of shear rate, and it is stabilized when the cell enters the narrow channel. To our best knowledge, this is the first 3D imaging of the RBC's morphology and RI map in a high-speed flow. Furthermore, with proper physical modeling, we can extract biomechanical parameters out of the temporal evolution of the RBC's 3D morphology, which could serve as important biomarkers for physiology and pathological studies.

4.4.2 High-throughput cytometer for NIH/3T3 cells

Another important application of DS-ODT is high-throughput 3D image cytometer. There are many seminal recent work such as optical time-stretch imaging that has pushed the 2D quantitative image cytometer's cytometer to over 10,000 cells/sec [137, 138]. Similarly high speed 3D cytometric imaging that can recover high resolution morphology and RI map remains to be demonstrated. There are also many other 3D image cytometers based on other contrast mechanism [166] that can offer richer biochemical information of the cells but have more limited throughput. Here, we demonstrate a 3D image cytometer based on the DS-ODT with a throughput of over 5,000 cells in one second with submicron resolution and rich 3D morphological and chemical information. We inject NIH/3T3 cells into the microfluidic channel (rectangular shape), shown in Fig. 4-10 (a), with a flow rate of $50\mu l/min$; subsequently we reconstructed the 3D RI maps of the cells in the microfluidic channel at an imaging speed of 12,500 frames per second. In our current system, we choose a flow rate ($50\mu l/min$) and exposure time ($15\mu s$), which allows each cell to appear in two adjacent frames. In Fig. 4-10(b), we show 3D rendering of the flowing NIH/3T3 cells' RI maps at different time points, from which we can clearly recognize the cell boundaries and nucleus. We acquired a time-lapse video with a duration of 160 ms, from which we segmented 3D RI maps of 936 flowing NIH/3T3 cells. Namely, we can count and analyze about 5580 cells per second with our 3D flow cytometer based on DS-ODT method. Besides, we calculated the mean refraction index, volume, surface

area and dry mass of each cell we imaged, whose histograms, mean values and standard deviations are shown in Figs. 4-10 (c) (d), (e) and (f). These parameters will give us more comprehensive phenotypes of the observed biological cells, which may lead to faster and more accurate clinical diagnosis in the future.

4.5 Discussions

In our study, single-frame quantitative label-free 3D mapping of refractive index is realized by a new technique called DS-ODT with both optical instrumentation innovations and a novel 3D reconstruction algorithm. On the one hand, the 3D RI map reconstructs by DS-ODT provides rich quantitative information of the measured cells, not only the cell shape, but also biophysical parameters, i.e. dry mass density, bending, and shearing moduli of the membrane, etc. On the other hand, the over 10,000 fps 3D imaging speed of DS-ODT gives access to large-scale cell characterization for image cytometer. Therefore, one envisions that DS-ODT may become a powerful tool for cell biological investigations and for clinical diagnosis.

As future work, the proposed DS-ODT algorithm opens many avenues for a more efficient optical tomographic microscope system. First, it greatly simplifies optical tomographic microscopy hardware and procedire, which only requires four multiplexed illumination angles without any scanning. Moreover, the four-angle multiplexing can be realized with 1x4 fiber optic couplers in principle, which may provide the possibilities for miniature label-free optical tomographic microscopes in the future. Finally, we have demonstrated satisfactory ability of DS-ODT algorithm to generalize across different cell types. However, instead of direct generalization, one can apply transfer learning [167] to transfer the knowledge learned from the source domain to the target domain, with only minimum training. The source domain and target domain could mean different species of cells and/or different optical systems. This adaption may lead to even better prediction performance in a disjoint domains and increases the versatility of the DS-ODT algorithm for biomedical research.

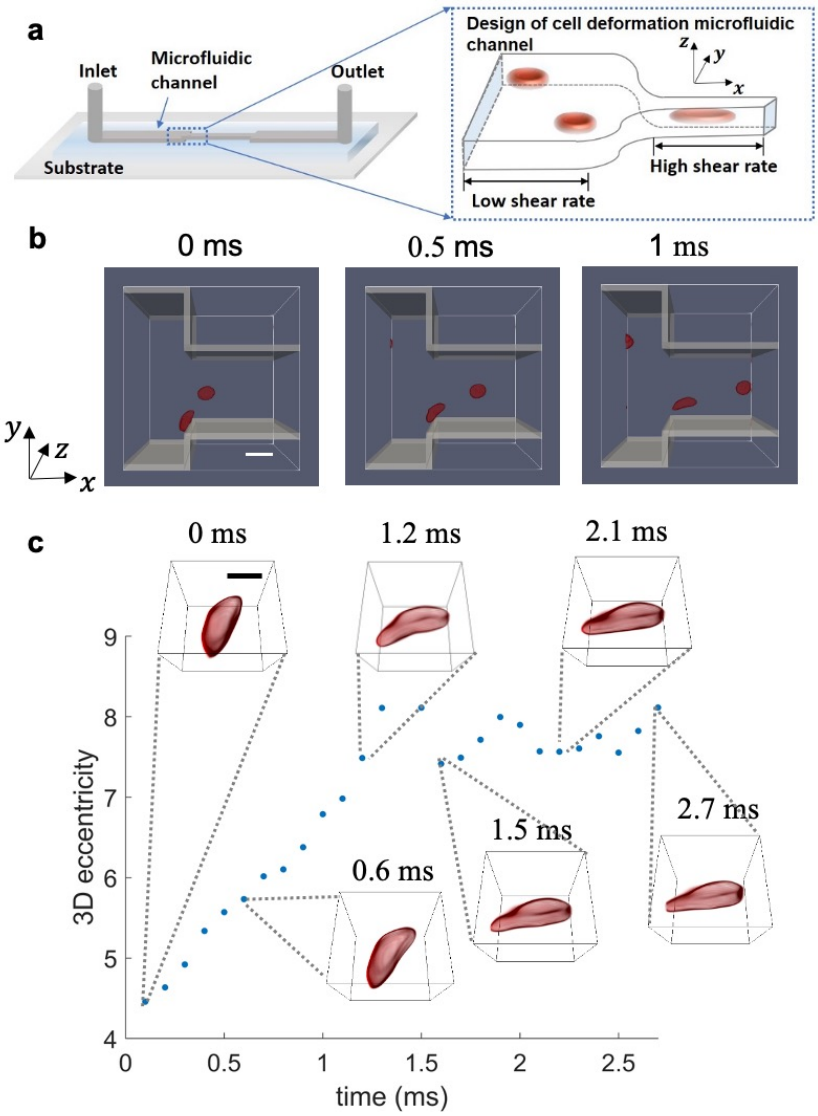

Figure 4-9: **Single-shot 3D imaging of RBC deformation in microfluidic channels.** (a) The design of the microfluidic channel. The left region is wider, where the shear rate of the cell is lower; while the right region is narrower with a higher shear rate. (b) the 3D rendering of the microfluidic channel and the flowing RBCs at time points of 0, 0.5 and 1ms. The scale bar denotes $20\mu m$. (c) the variation of the 3D eccentricity of one single cell over time (0∼2.7 ms). The 3D rendering of the selected cell's RI maps at 0, 0.6, 1.2, 1.5, 2.1 and 2.7 ms are embedded into this figure. The scale bar here denotes $10\mu m$.

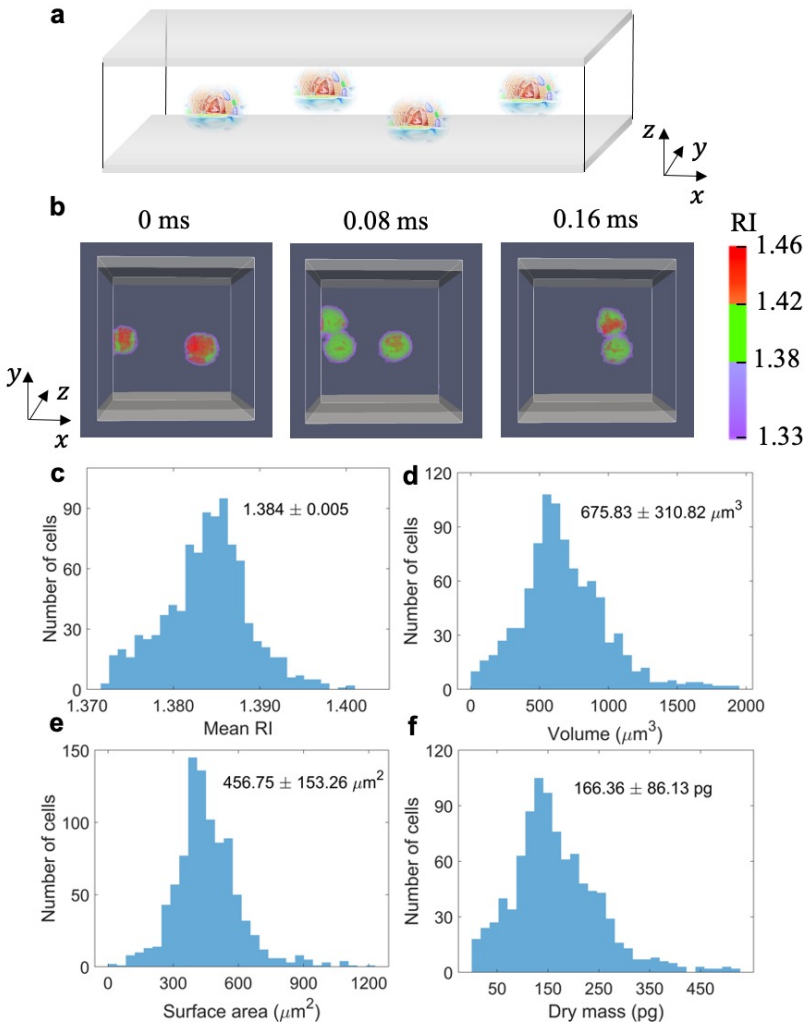

Figure 4-10: **Single-shot 3D imaging of RBC deformation in microfluidic channels.** The demonstration of single-shot 3D flowing cytometer in microfluidic channels. (a) The design of the microfluidic channel. (b) the 3D rendering of the microfluidic channel and the flowing NIH/3T3 cells at different time points. The flow rate of the NIH/3T3 cells is $50\mu l/min$, while the imaging speed is 12.5 fps. The scale bar denotes $20\mu m$. The histograms of the NIH/3T3 cells' (c) mean refraction index, (d) volume, (e) surface area and (f) dry mass which is imaged by our 3D flowing cytometer within 160 ms.

Chapter 5

Discussions and Future work

5.1 Story of the thesis

In Chapter 1 of this thesis, I introduced the demands of studying millisecond and micrometer-scale dynamical events in biomedical research and material inspections which motivates the development of novel optical imaging techniques. Thereafter, some representative quantitative label-free imaging techniques, and several recent progress in high-speed optical imaging are elaborated. However, these edge-cutting optical imaging assays are still not suitable for studying the aforementioned dynamical events, due to their limitations in imaging speed, spatial resolution, or non-quantitative imaging. Therefore, novel imaging instruments that provide high-speed, quantitative and label-free images without much loss in spatial resolution are still needed, which is the main topic of my PhD studies.

The main content of this Ph.D. dissertation focuses on developing single-shot, quantitative interferometric microscopy techniques, including single-shot quantitative amplitude and phase microscopy, single-shot quantitative polarization imaging and single-shot optical diffraction tomography. Technically, all of these novel imaging techniques are based on off-axis interferometry, where the interference between the two light beams (usually the sample and reference beams) generates interference fringes over space. With Hilbert transform or Fourier transform, we can quantitatively extract the optical field scattered by the specimen from the fringes with a single-shot full-

field acquisition. Therefore, incorporating off-axis interferometry with other optical systems (microscope, polarimeter, etc) paves the way for high-speed quantitative optical imaging with an imaging speed mostly limited by the frame rate of the camera (up to 10-100 kHz), while maintaining a submicron resolution. Further, this strategy extracts far more quantitative information (amplitude & phase, cell height & hemoglobin concentration, retardance & orientation angle, etc) than traditional microscopes.

Thanks to the aforementioned advantages, our novel imaging techniques are potentially powerful tools for studying millisecond, micrometer-scale dynamical events, paving the way for more insightful foundamentals in cell biology investigations and material sciences. Further, more comprehensive information about the cells could be extracted with our imaging methods at higher throughput for identidying cell's physiology and pathology in the diagnosis of many diseases. For example, in Chapter 2, I introcued that single-shot quantitative amplitude and phase microscopy may find applications in clinical diagnosis and drug screening of blood diseases, such as malaria and sickle cell disease, which require the quantitative imaging of RBCs, from which we can extract the RBCs' morphological, molecular and mechanical properties. By combining diffraction phase microscopy (DPM) with the engineering of the cell culture medium's optical properties, we realized single-shot quantitative amplitude and phase microscopy to simultaneously measure RBCs' shape, hemoglobin concentration and biomechanical parameters.

Single-shot quantitative polarization imaging is motivated by studies of the rheology of aniostropic materials, such as liquid crystals. The study of liquid crystals attracts interests of many scientists due to their expanding applications, especially for lytropic chromatic liquid crystals (LCLCs). However, the current quantitative polarization imaging techniques often requires scanning or multiple intensity images that limits their imaging speed and are unable to quantitatively extract the dynamical information of flowing LC. Here we combine the polarization sensitive microscope with off-axis shearing interferometry, realizing the single-shot quantitative imaging of LCLC flow with an imaging speed of over 500 fps. Furthermore, based on the

quantitative, high-speed imaging of the LC flow in microfluidic channel, a physical characterization of the LC flow in microfluidic channels is performed by our collaborators, which provide with more insights to the rheology of anisotropic materials; furthermore, these improvements may even enable the development of novel microfluidic devices that takes the anisotropic fluids instead of their isotropic counterparts.

Finally, single-shot optical diffraction tomography was developed, which is termed Deep-learning Single-shot Optical Diffraction Tomography (DS-ODT), as we consider how to fully exploit the potential of off-axis interferometric microscope, to push the imaging speed of 3D cell imaging. We have the goal of developing a 3D imaging flow cytometer which could be used for cell biology study, drug screening and clinical diagnosis. The 3-D structure of the cell could provide with more comprehensive information than their 2-D counterparts. By illuminating the cell with four angles simultaneously, and taking advantage of deep learning approach to extract the prior knowledge from the training dataset, we realized the single-shot 3D cell imaging and pushed its imaging speed to over 10,000 fps. Once incorporated with microfluidic channels, a 3D image cytometer could be made with an unprecedented 3D throughput of over 5,000 cells/sec, which could provide with far more information (morphology, dry mass, Hb concentration of RBC, etc) that are essential for large-scale cell characterization in clinical diagnosis.

However, even if some substantial progress have been made, there are still limitations of our new imaging techniques. First of all, the single-shot interferometric microscopy design can only push the imaging speed to a level limited by the camera frame rate (temporal resolution in millisecond). Even if this imaging speed is enough for observing cellular dynamic events (i.e. action potential, membrane fluctuation) and LC microfluidics, there are still many dynamic phenomena with faster time scales. Secondly, while the imaging speed is limited partly by the camera, it is also restricted by image signal to noise level that is related to the number of photons detected by each pixel. Furthermore, in the DS-ODT system, the angle-scanning is acquired with non-common-path off-axis interferometry resulting in mechanically induced temporal noise and narrow band laser source resulting in spatial speckle noise. Finally, in

DS-ODT, the incorporating of deep-learning dramatically enhance the imaging performance, however, over-fitting will incur if the image specimen has distinct features from the training dataset. Even if these problems have been greatly suppressed using physical-informed training strategy, the overfitting still need to be considered if we push the application of DS-ODT to broader application areas.

5.2 Future works

Driven by the needs of many biomedicine and clinical diagnosis applications, optical imaging approaches with higher throughput will continuously become more important. Therefore, it is quite interesting to continue my PhD work to push these novel techniques become more robust and reliable for research and clinical applications that may eventually lead to commercialization. Firstly, in the near future, we can continue the work of iPAM with absorptive medium and perfect this method by engineering the medium's osmotic pressure more carefully. After this method becomes more reliable, we can extend the imaging speed and throughput of this method by using faster CMOS camera, and combining it with flow cytometers. In this way, we can realize large-scale molecular, morphological and mechanical RBC analysis, which is potentially useful in the staging of sickle cell disease.

A second promising direction is to extend the applications of single-shot quantitative polarization imaging techniques (QPIM and PSIM). Since one of the limitations of current single-shot quantitative polarization techniques is that it is based on 2D imaging, where the retrieved retardance and orientation angle maps are the integrated values along the optical axis, which is not capable of resolving the 3D structure of the optically anisotropic samples (such as LC molecule's director field). Therefore, one of our future research directions is to offer PSIM 3D sectioning ability by using broadband light sources or confocal optical design, which could extend its capability to resolve the 3D configurations of the liquid crystals, active nematics and other anisotropic biological tissues. This advance may provide more insights into the optical anisotropic materials, or may offer new clinical diagnosis methods.

As we discussed in the last session in Chapter 4, the single-shot 3-D cell imaging realized by DS-ODT could potentially simplify the system design of current optical diffraction tomography (ODT) by removing mechanical scanning. This modification will significantly reduce the device cost and will allow easy adoption by many laboratories. Furthermore, although the generalization ability of DS-ODT algorithm has already been satisfactory, instead of direct generalization, one can apply transfer learning algorithms [167] to transfer the knowledge learned from one species of cells/imaging system to another species of cells/optical system, with only minimum additional training. This strategy will greatly mitigate the overfitting problem, when we extend the principles of DS-ODT to other applictaions and other imaging tools. Since high-speed 3-D imaging offers the possibility to study the molecular, morphological and mechanical parameters complex cells (and not only RBCs), DS-ODT should greatly extend the adoption of quantitative label-free microscopy in biomedical applications with integration in flow cytometer being especially promising.

Appendix A

Theoretical analysis of quantitative interferometric microscope's temporal sensitivity

In this part, we analyzed the temporal sensitivity of quantitative interferometric microscope system theoretically. The fundamental assumption of this theoretical analysis is that the main source of detection noise comes from shot noise, which is originated from the Poisson distribution of the photons received by the camera over time. The similar analysis has been done by Hosseini et.al [128]. However, they only analyzed the ideal scenario when the dynamic range of the camera pixel is fully used. In my thesis, this assumption is not valid since the amplitude and phase are measured simultaneously, which indicates the fringe contrast (amplitude) is not always at maximum. Here, we will try to figure out how the absolute value of contrast of the interference fringes, will influence the sensitivity of amplitude and phase measurement in off-axis interferometric microscopy. Here we define the modulus of the interference fringes over space as amplitude, and denote it as E in our following mathematical framework.

The interferogram of quantitative interferometric microscope can be express as following:

$$I = I_0[1 + E\cos(\phi + \phi_0)], \tag{A.1}$$

where E is the amplitude modulation of the interference term, ϕ is the phase distribution of the sample, and I_0 is the averaged intensity of the interferogram, ϕ_0 denotes the phase modulation of the measured intensity, which could be accomplished temporally (phase shifting) or spatially (off-axis interferometry). If we use the spatial phase modulation and take four pixels to sample one period of the intereference fringe, as shown in Fig. A-1, we can measure the intensities at the four lateral positions x_1, x_2, x_3 and x_4, where the value of ϕ_0 is 0, $\pi/2$, π and $3\pi/2$, and we denote them as I_1, I_2, I_3, I_4. If we measure these intensities over a long time, the temporal averages of I_1, I_2, I_3, I_4 can be expressed as:

$$\begin{aligned}
\bar{I_1} &= I_0[1 + E\cos\phi], \\
\bar{I_2} &= I_0[1 + E\cos(\phi + \frac{\pi}{2})] = I_0[1 - E\sin\phi], \\
\bar{I_3} &= I_0[1 + E\cos(\phi + \pi)] = I_0[1 - E\cos\phi], \\
\bar{I_4} &= I_0[1 + E\cos\phi + \frac{3\pi}{2}] = I_0[1 + E\sin\phi].
\end{aligned} \tag{A.2}$$

Here, E and ϕ are the true values of amplitude and phase distribution of the samples. I_0 is the spatial average of the intensities. It should be uniform (ignore the spatial uncertainties), and the absolution value of it is related to the power of the illumination and the quantum efficiency of the detector.

From the measured intensities(I_1, I_2, I_3, I_4), we can retrieve the DC term, amplitude and phase maps with the following algorithm. The estimated DC term $\hat{A}$ can be expressed by:

$$\hat{A} = \frac{1}{4}(I_1 + I_2 + I_3 + I_4), \tag{A.3}$$

In the meanwhile, we can express the estimated values of amplitude $\hat{E}$ and phase $\hat{\phi}$ as:

$$\hat{E} = \frac{2\sqrt{(I_1 - I_3)^2 + (I_2 - I_4)^2}}{I_1 + I_2 + I_3 + I_4}, \tag{A.4}$$

and

$$\hat{\phi} = \arctan\left(\frac{I_4 - I_2}{I_1 - I_3}\right) \tag{A.5}$$

Since we assume that the uncertainties of the measured intensities only come from the shot noise, the variance of the intensity measurements over time should be equal to their temporal average, which could be expressed as following:

$$\delta^2 I_1 = \bar{I_1}, \delta^2 I_2 = \bar{I_2}, \delta^2 I_3 = \bar{I_3}, \delta^2 I_4 = \bar{I_4}. \tag{A.6}$$

According to the error propagation principle, the uncertainties of the measured intensities will propagate to the retrieved DC term, amplitude and phase. Then we can have the uncertainties of each retrieved components as following

$$\begin{aligned}
\delta\hat{A} &= \sqrt{\bar{I_1} + \bar{I_2} + \bar{I_3} + \bar{I_4}}, \\
\delta\hat{E} &= \sqrt{2\left(\frac{(\bar{I_1} - \bar{I_3})^2(\bar{I_1} + \bar{I_3}) + (\bar{I_2} - \bar{I_4})^2(\bar{I_2} + \bar{I_4})}{[(\bar{I_1} - \bar{I_3})^2 + (\bar{I_2} - \bar{I_4})^2](\bar{I_1} + \bar{I_2} + \bar{I_3} + \bar{I_4})^2} + \frac{(\bar{I_1} - \bar{I_3})^2 + (\bar{I_2} - \bar{I_4})^2}{(\bar{I_1} + \bar{I_2} + \bar{I_3} + \bar{I_4})^3}\right)} \\
\delta\hat{\phi} &= \sqrt{\frac{\bar{I_2} + \bar{I_4}}{(\bar{I_1} - \bar{I_3})^2} + \frac{(\bar{I_2} - \bar{I_4})^2(\bar{I_1} + \bar{I_3})}{(\bar{I_1} - \bar{I_3})^4}}.
\end{aligned} \tag{A.7}$$

Plug Eqn. (A.2) to Eqn. (A.7), we can rewrite the expressions for the uncertainties of amplitude and phase as:

$$\begin{aligned}
\delta\hat{E} &= \sqrt{2\left(\frac{2I_0((2I_0E\cos\phi)^2 + (2I_0E\sin\phi)^2)}{((2I_0E\cos\phi)^2 + (2I_0E\sin\phi)^2)\cdot(4I_0)^2} + \frac{((2I_0E\cos\phi)^2 + (2I_0E\sin\phi)^2)}{(4I_0)^3}\right)} \\
&= \sqrt{1 + \frac{E^2}{2}} \cdot \frac{1}{2\sqrt{I_0}},
\end{aligned} \tag{A.8}$$

and

$$\begin{aligned}
\delta\hat{\phi} &= \sqrt{\frac{2I_0 \cdot ((2I_0E\cos\phi)^2 + (2I_0E\sin\phi)^2}{(2I_0E\cos\phi)^4}} \\
&= \frac{1}{E\cos^2\phi} \cdot \frac{1}{\sqrt{2I_0}}.
\end{aligned} \tag{A.9}$$

Here we need to make several assumptions. Firstly, we assume that the phase signal here is weak since we are usually observe weakly scattering specimen ($\phi << 1$ and

$\cos\phi \approx 1$). Further, to maximize the detection signal to noise ratio (SNR), and avoid the saturation of the measured intensities, we assume here the average intensity I_0 is the half of the full well depth of the CMOS camera's pixels N, that is $I_0 = N/2$. Therefore, we can rewrite the expression of the detection uncertainties as:

$$\begin{aligned} \delta\hat{E} &= \sqrt{1 + \frac{E^2}{2}} \cdot \frac{1}{\sqrt{2N}}, \\ \delta\hat{\phi} &= \frac{1}{E} \cdot \frac{1}{\sqrt{N}}. \end{aligned} \tag{A.10}$$

Then we can analyze two extreme cases: if the contrast of the fringes is approaching the maximum ($E \to 1$), we will have:

$$\begin{aligned} \delta\hat{E} &\to \frac{1}{\sqrt{2N}} \\ \delta\hat{\phi} &\to \frac{1}{\sqrt{N}} \end{aligned} \tag{A.11}$$

If the interefernce fringes' contrast is very low and approaching 0, the uncertainties of amplitude and phase become:

$$\begin{aligned} \delta\hat{E} &\to \frac{\sqrt{3}}{2\sqrt{N}} \\ \delta\hat{\phi} &\to \infty \end{aligned} \tag{A.12}$$

In summary, with the change of the amplitude value E, the uncertainty of the amplitude varies from $0.707/\sqrt{N}$ to $0.866/\sqrt{N}$, that are all smaller than $1/\sqrt{N}$. Therefore, in the sensitivity analysis sections in Chapter 2 and Chapter 3, we just assume $\delta\hat{E} \sim 1/\sqrt{N}$ to obtain the 'upper bound' of the retrieved parameters' uncertainties and avoid cumbersome calculations. For the uncertainty of phase $\delta\hat{\phi}$, it is quite clear that it is inversely proportional to the amplitude magnitude E, which is $\delta\hat{\phi} \sim (1/E)(1/\sqrt{N})$.

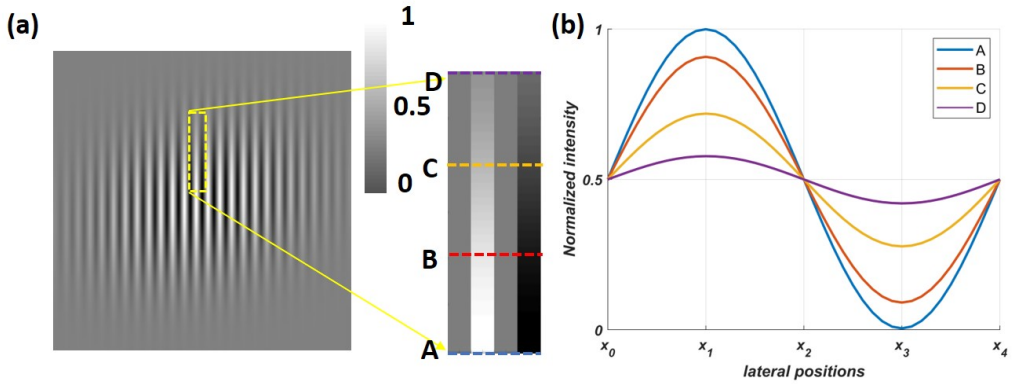

Figure A-1: **Sketch of the model used for the theoretical analysis of temporal sensitivity.** (a) the simulation of the interferogram whose fringe contrast(amplitude) is not uniform. One period of the fringes that the contrast decays along y-axis direction is zoomed in and shown separately. (b) the normalized intensity as a function of lateral positions of 'A', 'B', 'C' and 'D' labeled in (a).

Bibliography

[1] K Goda, KK Tsia, and B Jalali. Serial time-encoded amplified imaging for real-time observation of fast dynamic phenomena. *Nature*, 458(7242):1145–1149, 2009.

[2] Tong Ling, Kevin C Boyle, Valentina Zuckerman, Thomas Flores, Charu Ramakrishnan, Karl Deisseroth, and Daniel Palanker. High-speed interferometric imaging reveals dynamics of neuronal deformation during the action potential. *Proceedings of the National Academy of Sciences*, 117(19):10278–10285, 2020.

[3] YongKeun Park, Catherine A Best, Kamran Badizadegan, Ramachandra R Dasari, Michael S Feld, Tatiana Kuriabova, Mark L Henle, Alex J Levine, and Gabriel Popescu. Measurement of red blood cell mechanics during morphological changes. *Proceedings of the National Academy of Sciences*, 107(15):6731–6736, 2010.

[4] Poorya Hosseini, Sabia Z Abidi, E Du, Dimitrios P Papageorgiou, Youngwoon Choi, YongKeun Park, John M Higgins, Gregory J Kato, Subra Suresh, Ming Dao, et al. Cellular normoxic biophysical markers of hydroxyurea treatment in sickle cell disease. *Proceedings of the National Academy of Sciences*, 113(34):9527–9532, 2016.

[5] Sung Hwan Cho, Jessica M Godin, Chun-Hao Chen, Wen Qiao, Hosuk Lee, and Yu-Hwa Lo. Recent advancements in optofluidic flow cytometer. *Biomicrofluidics*, 4(4):043001, 2010.

[6] Misha Rahman. Introduction to flow cytometry. *AbD serotec*, 7, 2006.

[7] Deng-Ke Yang and Shin-Tson Wu. *Fundamentals of liquid crystal devices*. John Wiley & Sons, 2014.

[8] Shuang Zhou. *Lyotropic Chromonic Liquid Crystals: From Viscoelastic Properties to Living Liquid Crystals*. Springer, 2017.

[9] Anupam Sengupta, Uroš Tkalec, Miha Ravnik, Julia M Yeomans, Christian Bahr, and Stephan Herminghaus. Liquid crystal microfluidics for tunable flow shaping. *Physical review letters*, 110(4):048303, 2013.

[10] Anupam Sengupta. Topological constraints in a microfluidic platform. *Liquid Crystals*, 41(3):290–301, 2014.

[11] Jeff W Lichtman and José-Angel Conchello. Fluorescence microscopy. *Nature methods*, 2(12):910–919, 2005.

[12] YongKeun Park, Christian Depeursinge, and Gabriel Popescu. Quantitative phase imaging in biomedicine. *Nature photonics*, 12(10):578–589, 2018.

[13] Gabriel Popescu. *Quantitative phase imaging of cells and tissues*. McGraw-Hill Education, 2011.

[14] Douglas A Lauffenburger and Alan F Horwitz. Cell migration: a physically integrated molecular process. *Cell*, 84(3):359–369, 1996.

[15] Gabriel Popescu, YoungKeun Park, Niyom Lue, Catherine Best-Popescu, Lauren Deflores, Ramachandra R Dasari, Michael S Feld, and Kamran Badizadegan. Optical imaging of cell mass and growth dynamics. *American Journal of Physiology-Cell Physiology*, 295(2):C538–C544, 2008.

[16] YongKeun Park, Catherine A Best, Thorsten Auth, Nir S Gov, Samuel A Safran, Gabriel Popescu, Subra Suresh, and Michael S Feld. Metabolic remodeling of the human red blood cell membrane. *Proceedings of the National Academy of Sciences*, 107(4):1289–1294, 2010.

[17] Renjie Zhou, Chris Edwards, Amir Arbabi, Gabriel Popescu, and Lynford L Goddard. Detecting 20 nm wide defects in large area nanopatterns using optical interferometric microscopy. *Nano letters*, 13(8):3716–3721, 2013.

[18] Katherine Creath. V phase-measurement interferometry techniques. In *Progress in optics*, volume 26, pages 349–393. Elsevier, 1988.

[19] Zhuo Wang, Larry Millet, Mustafa Mir, Huafeng Ding, Sakulsuk Unarunotai, John Rogers, Martha U Gillette, and Gabriel Popescu. Spatial light interference microscopy (slim). *Optics express*, 19(2):1016–1026, 2011.

[20] Tan H Nguyen and Gabriel Popescu. Spatial light interference microscopy (slim) using twisted-nematic liquid-crystal modulation. *Biomedical optics express*, 4(9):1571–1583, 2013.

[21] Gabriel Popescu, Lauren P Deflores, Joshua C Vaughan, Kamran Badizadegan, Hidenao Iwai, Ramachandra R Dasari, and Michael S Feld. Fourier phase microscopy for investigation of biological structures and dynamics. *Optics letters*, 29(21):2503–2505, 2004.

[22] Takahiro Ikeda, Gabriel Popescu, Ramachandra R Dasari, and Michael S Feld. Hilbert phase microscopy for investigating fast dynamics in transparent systems. *Optics letters*, 30(10):1165–1167, 2005.

[23] Gabriel Popescu, Takahiro Ikeda, Ramachandra R Dasari, and Michael S Feld. Diffraction phase microscopy for quantifying cell structure and dynamics. *Optics letters*, 31(6):775–777, 2006.

[24] Rudolf Oldenbourg. Polarized light microscopy: principles and practice. *Cold Spring Harbor Protocols*, 2013(11):pdb–top078600, 2013.

[25] Tristan Colomb, Florian Dürr, Etienne Cuche, Pierre Marquet, Hans G Limberger, René-Paul Salathé, and Christian Depeursinge. Polarization microscopy by use of digital holography: application to optical-fiber birefringence measurements. *Applied optics*, 44(21):4461–4469, 2005.

[26] Rudolf Oldenbourg. A new view on polarization microscopy. *Nature*, 381(6585):811–812, 1996.

[27] Rudolf Oldenbourg et al. Polarization microscopy with the lc-polscope. *Live cell imaging: A laboratory manual*, pages 205–237, 2005.

[28] Michael Shribak and Rudolf Oldenbourg. Techniques for fast and sensitive measurements of two-dimensional birefringence distributions. *Applied Optics*, 42(16):3009–3017, 2003.

[29] Rudolf Oldenbourg. Analysis of edge birefringence. *Biophysical journal*, 60(3):629–641, 1991.

[30] Shinya Inoué and Rudolf Oldenbourg. Microtubule dynamics in mitotic spindle displayed by polarized light microscopy. *Molecular biology of the cell*, 9(7):1603–1607, 1998.

[31] Rudolf Oldenbourg, ED Salmon, and PT Tran. Birefringence of single and bundled microtubules. *Biophysical journal*, 74(1):645–654, 1998.

[32] Di Jin, Renjie Zhou, Zahid Yaqoob, and Peter TC So. Tomographic phase microscopy: principles and applications in bioimaging. *JOSA B*, 34(5):B64–B77, 2017.

[33] Youngwoon Choi, Poorya Hosseini, Wonshik Choi, Ramachandra R Dasari, Peter TC So, and Zahid Yaqoob. Dynamic speckle illumination wide-field reflection phase microscopy. *Optics letters*, 39(20):6062–6065, 2014.

[34] Zahid Yaqoob, Toyohiko Yamauchi, Wonshik Choi, Dan Fu, Ramachandra R Dasari, and Michael S Feld. Single-shot full-field reflection phase microscopy. *Optics express*, 19(8):7587–7595, 2011.

[35] Toyohiko Yamauchi, Hidenao Iwai, and Yutaka Yamashita. Label-free imaging of intracellular motility by low-coherent quantitative phase microscopy. *Optics express*, 19(6):5536–5550, 2011.

[36] Wonshik Choi, Christopher Fang-Yen, Kamran Badizadegan, Seungeun Oh, Niyom Lue, Ramachandra R Dasari, and Michael S Feld. Tomographic phase microscopy. *Nature methods*, 4(9):717–719, 2007.

[37] Florian Charrière, Anca Marian, Frédéric Montfort, Jonas Kuehn, Tristan Colomb, Etienne Cuche, Pierre Marquet, and Christian Depeursinge. Cell refractive index tomography by digital holographic microscopy. *Optics letters*, 31(2):178–180, 2006.

[38] Kimberly L Cooper, Seungeun Oh, Yongjin Sung, Ramachandra R Dasari, Marc W Kirschner, and Clifford J Tabin. Multiple phases of chondrocyte enlargement underlie differences in skeletal proportions. *Nature*, 495(7441):375–378, 2013.

[39] Taewoo Kim, Renjie Zhou, Mustafa Mir, S Derin Babacan, P Scott Carney, Lynford L Goddard, and Gabriel Popescu. White-light diffraction tomography of unlabelled live cells. *Nature Photonics*, 8(3):256–263, 2014.

[40] Tan H Nguyen, Mikhail E Kandel, Marcello Rubessa, Matthew B Wheeler, and Gabriel Popescu. Gradient light interference microscopy for 3d imaging of unlabeled specimens. *Nature communications*, 8(1):1–9, 2017.

[41] Mikhail E Kandel, Chenfei Hu, Ghazal Naseri Kouzehgarani, Eunjung Min, Kathryn Michele Sullivan, Hyunjoon Kong, Jennifer M Li, Drew N Robson, Martha U Gillette, Catherine Best-Popescu, et al. Epi-illumination gradient light interference microscopy for imaging opaque structures. *Nature communications*, 10(1):1–9, 2019.

[42] Yongjin Sung, Wonshik Choi, Christopher Fang-Yen, Kamran Badizadegan, Ramachandra R Dasari, and Michael S Feld. Optical diffraction tomography for high resolution live cell imaging. *Optics express*, 17(1):266–277, 2009.

[43] Di Jin, Renjie Zhou, Zahid Yaqoob, and Peter TC So. Dynamic spatial filtering using a digital micromirror device for high-speed optical diffraction tomography. *Optics express*, 26(1):428–437, 2018.

[44] JooWon Lim, KyeoReh Lee, Kyong Hwan Jin, Seungwoo Shin, SeoEun Lee, YongKeun Park, and Jong Chul Ye. Comparative study of iterative reconstruction algorithms for missing cone problems in optical diffraction tomography. *Optics express*, 23(13):16933–16948, 2015.

[45] Ulugbek S Kamilov, Ioannis N Papadopoulos, Morteza H Shoreh, Alexandre Goy, Cedric Vonesch, Michael Unser, and Demetri Psaltis. Learning approach to optical tomography. *Optica*, 2(6):517–522, 2015.

[46] Francesco Merola, Pasquale Memmolo, Lisa Miccio, Roberto Savoia, Martina Mugnano, Angelo Fontana, Giuliana D'ippolito, Angela Sardo, Achille Iolascon, Antonella Gambale, et al. Tomographic flow cytometry by digital holography. *Light: Science & Applications*, 6(4):e16241–e16241, 2017.

[47] Seungwoo Shin, Kyoohyun Kim, Jonghee Yoon, and YongKeun Park. Active illumination using a digital micromirror device for quantitative phase imaging. *Optics letters*, 40(22):5407–5410, 2015.

[48] F Brochard and JF Lennon. Frequency spectrum of the flicker phenomenon in erythrocytes. *Journal de Physique*, 36(11):1035–1047, 1975.

[49] Gang Bao and Subra Suresh. Cell and molecular mechanics of biological materials. *Nature materials*, 2(11):715–725, 2003.

[50] DE Discher, N Mohandas, and EA Evans. Molecular maps of red cell deformation: hidden elasticity and in situ connectivity. *Science*, 266(5187):1032–1035, 1994.

[51] H Engelhardt, H Gaub, and E Sackmann. Viscoelastic properties of erythrocyte membranes in high-frequency electric fields. *Nature*, 307(5949):378–380, 1984.

[52] RM Hochmuth, KL Buxbaum, and EA Evans. Temperature dependence of the viscoelastic recovery of red cell membrane. *Biophysical journal*, 29(1):177–182, 1980.

[53] Christina Kelemen, Shu Chien, and GM Artmann. Temperature transition of human hemoglobin at body temperature: effects of calcium. *Biophysical journal*, 80(6):2622–2630, 2001.

[54] HeeSu Byun, Timothy R Hillman, John M Higgins, Monica Diez-Silva, Zhangli Peng, Ming Dao, Ramachandra R Dasari, Subra Suresh, and YongKeun Park. Optical measurement of biomechanical properties of individual erythrocytes from a sickle cell patient. *Acta biomaterialia*, 8(11):4130–4138, 2012.

[55] YongKeun Park, Monica Diez-Silva, Gabriel Popescu, George Lykotrafitis, Wonshik Choi, Michael S Feld, and Subra Suresh. Refractive index maps and membrane dynamics of human red blood cells parasitized by plasmodium falciparum. *Proceedings of the National Academy of Sciences*, 105(37):13730–13735, 2008.

[56] Tan H Nguyen, Mikhail Kandel, Haadi M Shakir, Catherine Best-Popescu, Jyothi Arikkath, Minh N Do, and Gabriel Popescu. Halo-free phase contrast microscopy. *Scientific reports*, 7(1):1–10, 2017.

[57] Moritz Friebel and Martina Meinke. Model function to calculate the refractive index of native hemoglobin in the wavelength range of 250-1100 nm dependent on concentration. *Applied optics*, 45(12):2838–2842, 2006.

[58] SA Prahl. Tabulated molar extinction coefficient for hemoglobin in water. *http://omlc. ogi. edu/spectra/hemoglobin/summary. html*, 1999.

[59] Jennifer L Gregg, Karen M McGuire, Daniel C Focht, and Michael A Model. Measurement of the thickness and volume of adherent cells using transmission-through-dye microscopy. *Pflügers Archiv-European Journal of Physiology*, 460(6):1097–1104, 2010.

[60] Ethan Schonbrun, Roy Malka, Giuseppe Di Caprio, Diane Schaak, and John M Higgins. Quantitative absorption cytometry for measuring red blood cell hemoglobin mass and volume. *Cytometry Part A*, 85(4):332–338, 2014.

[61] Valerio Lucarini, Jarkko J Saarinen, Kai-Erik Peiponen, and Erik M Vartiainen. *Kramers-Kronig relations in optical materials research*, volume 110. Springer Science & Business Media, 2005.

[62] Heung-Shik Park, Shin-Woong Kang, Luana Tortora, Yuriy Nastishin, Daniele Finotello, Satyendra Kumar, and Oleg D Lavrentovich. Self-assembly of lyotropic chromonic liquid crystal sunset yellow and effects of ionic additives. *The Journal of Physical Chemistry B*, 112(51):16307–16319, 2008.

[63] Matthew P Renshaw and Iain J Day. Nmr characterization of the aggregation state of the azo dye sunset yellow in the isotropic phase. *The Journal of Physical Chemistry B*, 114(31):10032–10038, 2010.

[64] John Lydon. Chromonic liquid crystalline phases. *Liquid Crystals*, 38(11-12):1663–1681, 2011.

[65] Shuang Zhou, Yu A Nastishin, MM Omelchenko, L Tortora, VG Nazarenko, OP Boiko, T Ostapenko, T Hu, CC Almasan, SN Sprunt, et al. Elasticity of lyotropic chromonic liquid crystals probed by director reorientation in a magnetic field. *Physical review letters*, 109(3):037801, 2012.

[66] Shuang Zhou, Krishna Neupane, Yuriy A. Nastishin, Alan R. Baldwin, Sergij V. Shiyanovskii, Oleg D. Lavrentovich, and Samuel Sprunt. Elasticity, viscosity, and orientational fluctuations of a lyotropic chromonic nematic liquid crystal disodium cromoglycate. *Soft Matter*, 10:6571–6581, 2014.

[67] Peter J Collings, Joshua N Goldstein, Elizabeth J Hamilton, Benjamin R Mercado, Kenneth J Nieser, and Margaret H Regan. The nature of the assembly process in chromonic liquid crystals. *Liquid Crystals Reviews*, 3(1):1–27, 2015.

[68] SV Shiyanovskii, OD Lavrentovich, T Schneider, T Ishikawa, II Smalyukh, CJ Woolverton, GD Niehaus, and KJ Doane. Lyotropic chromonic liquid crystals for biological sensing applications. *Molecular Crystals and Liquid Crystals*, 434(1):259–587, 2005.

[69] Tatiana Sergan, Tod Schneider, Jack Kelly, and OD Lavrentovich. Polarizing-alignment layers for twisted nematic cells. *Liquid Crystals*, 27(5):567–572, 2000.

[70] Suk-Wah Tam-Chang, Wonewoo Seo, Kyle Rove, and Sean M Casey. Molecularly designed chromonic liquid crystals for the fabrication of broad spectrum polarizing materials. *Chemistry of materials*, 16(10):1832–1834, 2004.

[71] VG Nazarenko, OP Boiko, MI Anisimov, AK Kadashchuk, Yu A Nastishin, AB Golovin, and OD Lavrentovich. Lyotropic chromonic liquid crystal semiconductors for water-solution processable organic electronics. *Applied Physics Letters*, 97(26):284, 2010.

[72] Fei Guo, Amartya Mukhopadhyay, Brian W Sheldon, and Robert H Hurt. Vertically aligned graphene layer arrays from chromonic liquid crystal precursors. *Advanced materials*, 23(4):508–513, 2011.

[73] H. S. Park and O. D. Lavrentovich. *Liquid crystals beyond displays: chemistry, physics, and applications*. John Wiley & Sons, 2012.

[74] Shuang Zhou, Andrey Sokolov, Oleg D Lavrentovich, and Igor S Aranson. Living liquid crystals. *Proceedings of the National Academy of Sciences*, 111(4):1265–1270, 2014.

[75] Andrew Masters. Chromonic liquid crystals: more questions than answers. *Liquid Crystals Today*, 25(2):30–37, 2016.

[76] Mikhail M Genkin, Andrey Sokolov, Oleg D Lavrentovich, and Igor S Aranson. Topological defects in a living nematic ensnare swimming bacteria. *Physical Review X*, 7(1):011029, 2017.

[77] Andrey Sokolov, Ali Mozaffari, Rui Zhang, Juan J De Pablo, and Alexey Snezhko. Emergence of radial tree of bend stripes in active nematics. *Physical Review X*, 9(3):031014, 2019.

[78] Peter C Mushenheim, Rishi R Trivedi, Susmit Singha Roy, Michael S Arnold, Douglas B Weibel, and Nicholas L Abbott. Effects of confinement, surface-induced orientations and strain on dynamical behaviors of bacteria in thin liquid crystalline films. *Soft Matter*, 11(34):6821–6831, 2015.

[79] Chenhui Peng, Taras Turiv, Yubing Guo, Qi-Huo Wei, and Oleg D Lavrentovich. Command of active matter by topological defects and patterns. *Science*, 354(6314):882–885, 2016.

[80] Shuang Zhou, Oleh Tovkach, Dmitry Golovaty, Andrey Sokolov, Igor S Aranson, and Oleg D Lavrentovich. Dynamic states of swimming bacteria in a nematic liquid crystal cell with homeotropic alignment. *New Journal of Physics*, 19(5):055006, 2017.

[81] I Janossy, P Pieranski, and E Guyon. Poiseuille flow in nematics: experimental study of the instabilities. *Journal de Physique*, 37(10):1105–1113, 1976.

[82] DJ Graziano and MR Mackley. Shear induced optical textures and their relaxation behaviour in thermotropic liquid crystalline polymers. *Molecular Crystals and Liquid Crystals*, 106(1-2):73–93, 1984.

[83] PT Mather, DS Pearson, and RG Larson. Flow patterns and disclination-density measurements in sheared nematic liquid crystals i: Flow-aligning 5cb. *Liquid crystals*, 20(5):527–538, 1996.

[84] RG Larson and DW Mead. The ericksen number and deborah number cascades in sheared polymeric nematics. *Liquid crystals*, 15(2):151–169, 1993.

[85] Jörg A Müller, Richard S Stein, and H Henning Winter. Rotation of liquid crystalline macromolecules in shear flow and shear-induced periodic orientation patterns. *Rheologica acta*, 35(2):160–167, 1996.

[86] Jean-Bernard Riti, MT Cidade, MH Godinho, AF Martins, and Patrick Navard. Shear induced textures of thermotropic acetoxypropylcellulose. *Journal of Rheology*, 41(6):1247–1260, 1997.

[87] Alejandro D Rey and Morton M Denn. Dynamical phenomena in liquid-crystalline materials. *Annual Review of Fluid Mechanics*, 34(1):233–266, 2002.

[88] Jan Vermant, Paula Moldenaers, SJ Picken, and Joannes Mewis. A comparison between texture and rheological behaviour of lyotropic liquid crystalline polymers during flow. *Journal of non-newtonian fluid mechanics*, 53:1–23, 1994.

[89] D Harley Klein, L Gary Leal, Carlos J García-Cervera, and Hector D Ceniceros. Three-dimensional shear-driven dynamics of polydomain textures and disclination loops in liquid crystalline polymers. *Journal of Rheology*, 52(3):837–863, 2008.

[90] Sumesh P Thampi, Ramin Golestanian, and Julia M Yeomans. Driven active and passive nematics. *Molecular Physics*, 113(17-18):2656–2665, 2015.

[91] DJ Graziano and MR Mackley. Disclinations observed during the shear of mbba. *Molecular crystals and liquid crystals*, 106(1-2):103–119, 1984.

[92] Anupam Sengupta, Benjamin Schulz, Elena Ouskova, and Christian Bahr. Functionalization of microfluidic devices for investigation of liquid crystal flows. *Microfluidics and nanofluidics*, 13(6):941–955, 2012.

[93] Zongdai Liu, Dan Luo, and Kun-Lin Yang. Flow-driven disclination lines of nematic liquid crystals inside a rectangular microchannel. *Soft matter*, 15(28):5638–5643, 2019.

[94] Anupam Sengupta, Uroš Tkalec, and Christian Bahr. Nematic textures in microfluidic environment. *Soft Matter*, 7(14):6542–6549, 2011.

[95] Benjamin S Hsiao, Richard S Stein, Klaus Deutscher, and H Henning Winter. Optical anisotropy of a thermotropic liquid-crystalline polymer in transient shear. *Journal of Polymer Science Part B: Polymer Physics*, 28(9):1571–1588, 1990.

[96] T De'Nève, P Navard, and M Kleman. Nature of the flow-induced worm texture of thermotropic polymers. *Macromolecules*, 28(5):1541–1546, 1995.

[97] Masao Doi, Samuel Frederick Edwards, and Samuel Frederick Edwards. *The theory of polymer dynamics*, volume 73. oxford university press, 1988.

[98] Giuseppe Marrucci and Francesco Greco. Flow behavior of liquid crystalline polymers. *Advances in chemical physics*, 86:331–404, 1993.

[99] Ronald G Larson. *The structure and rheology of complex fluids*, volume 150. Oxford university press New York, 1999.

[100] G Sgalari, GL Leal, and JJ Feng. The shear flow behavior of lcps based on a generalized doi model with distortional elasticity. *Journal of non-newtonian fluid mechanics*, 102(2):361–382, 2002.

[101] Y-G Tao, Wouter K den Otter, and Willem J Briels. Kayaking and wagging of liquid crystals under shear: Comparing director and mesogen motions. *EPL (Europhysics Letters)*, 86(5):56005, 2009.

[102] Hakam Agha and Christian Bahr. Connecting and disconnecting nematic disclination lines in microfluidic channels. *Soft Matter*, 12(18):4266–4273, 2016.

[103] Luca Giomi, Žiga Kos, Miha Ravnik, and Anupam Sengupta. Cross-talk between topological defects in different fields revealed by nematic microfluidics. *Proceedings of the National Academy of Sciences*, 114(29):E5771–E5777, 2017.

[104] Tadej Emeršič, Rui Zhang, Žiga Kos, Simon Čopar, Natan Osterman, Juan J De Pablo, and Uroš Tkalec. Sculpting stable structures in pure liquids. *Science advances*, 5(2):eaav4283, 2019.

[105] Simon Čopar, Žiga Kos, Tadej Emeršič, and Uroš Tkalec. Microfluidic control over topological states in channel-confined nematic flows. *Nature communications*, 11(1):1–10, 2020.

[106] Tomohiro Ouchi, Koki Imamura, Kanta Sunami, Hiroyuki Yoshida, Masanori Ozaki, et al. Topologically protected generation of stable wall loops in nematic liquid crystals. *Physical review letters*, 123(9):097801, 2019.

[107] Hend Baza, Taras Turiv, Bing-Xiang Li, Ruipeng Li, Benjamin M Yavitt, Masafumi Fukuto, and Oleg D Lavrentovich. Shear-induced polydomain structures of nematic lyotropic chromonic liquid crystal disodium cromoglycate. *Soft Matter*, 16(37):8565–8576, 2020.

[108] Anshul Sharma, Irvine Lian Hao Ong, and Anupam Sengupta. Time dependent lyotropic chromonic textures in microfluidic confinements. *Crystals*, 11(1):35, 2021.

[109] Shuang Zhou, Sergij V Shiyanovskii, Heung-Shik Park, and Oleg D Lavrentovich. Fine structure of the topological defect cores studied for disclinations in lyotropic chromonic liquid crystals. *Nature Communications*, 8(1):1–7, 2017.

[110] Karthik Nayani, Rui Chang, Jinxin Fu, Perry W Ellis, Alberto Fernandez-Nieves, Jung Ok Park, and Mohan Srinivasarao. Spontaneous emergence of chirality in achiral lyotropic chromonic liquid crystals confined to cylinders. *Nature communications*, 6(1):1–7, 2015.

[111] Zoey S Davidson, Louis Kang, Joonwoo Jeong, Tim Still, Peter J Collings, Tom C Lubensky, and AG Yodh. Chiral structures and defects of lyotropic chromonic liquid crystals induced by saddle-splay elasticity. *Physical Review E*, 91(5):050501, 2015.

[112] Luana Tortora and Oleg D Lavrentovich. Chiral symmetry breaking by spatial confinement in tactoidal droplets of lyotropic chromonic liquid crystals. *Proceedings of the National Academy of Sciences*, 108(13):5163–5168, 2011.

[113] Geonhyeong Park, Simon Copar, Ahram Suh, Minyong Yang, Uros Tkalec, and Dong Ki Yoon. Periodic arrays of chiral domains generated from the self-assembly of micropatterned achiral lyotropic chromonic liquid crystal. *ACS central science*, 6(11):1964–1970, 2020.

[114] Oleg D Lavrentovich. Design of chiral domains by surface confinement of liquid crystals, 2020.

[115] KV Kaznatcheev, P Dudin, OD Lavrentovich, and AP Hitchcock. X-ray microscopy study of chromonic liquid crystal dry film texture. *Physical Review E*, 76(6):061703, 2007.

[116] Eugene Chang, Young-Cheol Lee, Jin Ku Cho, and Seunghan Shin. Polarization efficiency enhancement of anisotropic films cast from yellow lyotropic chromonic liquid crystal using its coupled core structure. *Thin Solid Films*, 589:798–804, 2015.

[117] Takuya Suzuki and Yuko Kojima. Structural evolution during drying process in lyotropic chromonic liquid crystal. *Molecular Crystals and Liquid Crystals*, 648(1):29–34, 2017.

[118] Takuya Suzuki and Yuko Kojima. Direct structural observation of the alignment and elongation in lyotropic chromonic liquid crystals under shear flow. *Molecular Crystals and Liquid Crystals*, 648(1):162–167, 2017.

[119] Yun Jeong Cha, Min-Jun Gim, Hyungju Ahn, Tae Joo Shin, Joonwoo Jeong, and Dong Ki Yoon. Orthogonal liquid crystal alignment layer: templating speed-dependent orientation of chromonic liquid crystals. *ACS applied materials & interfaces*, 9(21):18355–18361, 2017.

[120] Ivan I Smalyukh, SV Shiyanovskii, and OD Lavrentovich. Three-dimensional imaging of orientational order by fluorescence confocal polarizing microscopy. *Chemical Physics Letters*, 336(1-2):88–96, 2001.

[121] Taewoo Lee, Bohdan Senyuk, Rahul P Trivedi, and Ivan I Smalyukh. Optical microscopy of soft matter systems. *Fluids, Colloids and Soft Materials-An Introduction to Soft Matter Physics, edited by Alberto Fernandez-Nieves Antonio Manuel Puertas (John Wiley & Sons)*, pages 165–185, 2016.

[122] OD Lavrentovich. Fluorescence confocal polarizing microscopy: Three-dimensional imaging of the director. *Pramana*, 61(2):373–384, 2003.

[123] Huafeng Ding, Zhuo Wang, Xing Liang, Stephen A Boppart, Krishna Tangella, and Gabriel Popescu. Measuring the scattering parameters of tissues from quantitative phase imaging of thin slices. *Optics letters*, 36(12):2281–2283, 2011.

[124] Zhuo Wang, Larry J Millet, Martha U Gillette, and Gabriel Popescu. Jones phase microscopy of transparent and anisotropic samples. *Optics letters*, 33(11):1270–1272, 2008.

[125] Seungwoo Shin, KyeoReh Lee, Zahid Yaqoob, Peter TC So, and YongKeun Park. Reference-free polarization-sensitive quantitative phase imaging using single-point optical phase conjugation. *Optics express*, 26(21):26858–26865, 2018.

[126] Baoliang Ge, Renjie Zhou, Yu Takiguchi, Zahid Yaqoob, and Peter TC So. Single-shot optical anisotropy imaging with quantitative polarization interference microscopy. *Laser & photonics reviews*, 12(8):1800070, 2018.

[127] Richard M Goldstein, Howard A Zebker, and Charles L Werner. Satellite radar interferometry: Two-dimensional phase unwrapping. *Radio science*, 23(4):713–720, 1988.

[128] Poorya Hosseini, Renjie Zhou, Yang-Hyo Kim, Chiara Peres, Alberto Diaspro, Cuifang Kuang, Zahid Yaqoob, and Peter TC So. Pushing phase and amplitude sensitivity limits in interferometric microscopy. *Optics letters*, 41(7):1656–1659, 2016.

[129] Yu A Nastishin, H Liu, T Schneider, V Nazarenko, Rk Vasyuta, SV Shiyanovskii, and OD Lavrentovich. Optical characterization of the nematic lyotropic chromonic liquid crystals: Light absorption, birefringence, and scalar order parameter. *Physical Review E*, 72(4):041711, 2005.

[130] LK Varga, F Mazaleyrat, J Kovac, and JM Greneche. Structural and magnetic properties of metastable fe1-xsix ($0.15< x< 0.34$) alloys prepared by a rapid-quenching technique. *Journal of Physics: Condensed Matter*, 14(8):1985, 2002.

[131] Keisuke Goda and Bahram Jalali. Dispersive fourier transformation for fast continuous single-shot measurements. *Nature Photonics*, 7(2):102–112, 2013.

[132] Ali Fard, Ata Mahjoubfar, Keisuke Goda, and Bahram Jalali. Nomarski serial time-encoded amplified microscope for high throughput imaging of transparent media. In *CLEO: Science and Innovations*, page CThW1. Optical Society of America, 2011.

[133] Liang Gao, Jinyang Liang, Chiye Li, and Lihong V Wang. Single-shot compressed ultrafast photography at one hundred billion frames per second. *Nature*, 516(7529):74–77, 2014.

[134] Jinyang Liang, Peng Wang, Liren Zhu, and Lihong V Wang. Single-shot stereo-polarimetric compressed ultrafast photography for light-speed observation of high-dimensional optical transients with picosecond resolution. *Nature communications*, 11(1):1–10, 2020.

[135] Peng Wang, Jinyang Liang, and Lihong V Wang. Single-shot ultrafast imaging attaining 70 trillion frames per second. *Nature communications*, 11(1):1–9, 2020.

[136] Jinyang Liang and Lihong V Wang. Single-shot ultrafast optical imaging. *Optica*, 5(9):1113–1127, 2018.

[137] Kelvin CM Lee, Maolin Wang, Kathryn SE Cheah, Godfrey CF Chan, Hayden KH So, Kenneth KY Wong, and Kevin K Tsia. Quantitative phase imaging flow cytometry for ultra-large-scale single-cell biophysical phenotyping. *Cytometry Part A*, 95(5):510–520, 2019.

[138] Kelvin CM Lee, Andy KS Lau, Anson HL Tang, Maolin Wang, Aaron TY Mok, Bob MF Chung, Wenwei Yan, Ho C Shum, Kathryn SE Cheah, Godfrey CF Chan, et al. Multi-atom: Ultrahigh-throughput single-cell quantitative phase imaging with subcellular resolution. *Journal of biophotonics*, 12(7):e201800479, 2019.

[139] DA Peterson. Confocal microscopy. 2010.

[140] Warren R Zipfel, Rebecca M Williams, and Watt W Webb. Nonlinear magic: multiphoton microscopy in the biosciences. *Nature biotechnology*, 21(11):1369–1377, 2003.

[141] David Huang, Eric A Swanson, Charles P Lin, Joel S Schuman, William G Stinson, Warren Chang, Michael R Hee, Thomas Flotte, Kenton Gregory, Carmen A Puliafito, et al. Optical coherence tomography. *science*, 254(5035):1178–1181, 1991.

[142] M Hillebrand, N Stevanovic, BJ Hosticka, JE Santos Conde, A Teuner, and M Schwarz. High speed camera system using a cmos image sensor. In *Proceedings of the IEEE Intelligent Vehicles Symposium 2000 (Cat. No. 00TH8511)*, pages 656–661. IEEE, 2000.

[143] Baotan Jiang, Zhibin Pan, and Yuehong Qiu. Study on the key technologies of a high-speed cmos camera. *Optik*, 129:100–107, 2017.

[144] Takeo Tanaami, Shinya Otsuki, Nobuhiro Tomosada, Yasuhito Kosugi, Mizuho Shimizu, and Hideyuki Ishida. High-speed 1-frame/ms scanning confocal microscope with a microlens and nipkow disks. *Applied Optics*, 41(22):4704–4708, 2002.

[145] Chen Bai, Xianghua Yu, Tong Peng, Chao Liu, Junwei Min, Dan Dan, and Baoli Yao. 3d imaging restoration of spinning-disk confocal microscopy via deep learning. *IEEE Photonics Technology Letters*, 32(18):1131–1134, 2020.

[146] Samantha Stehbens, Hayley Pemble, Lyndsay Murrow, and Torsten Wittmann. Imaging intracellular protein dynamics by spinning disk confocal microscopy. *Methods in enzymology*, 504:293–313, 2012.

[147] Egidijus Auksorius, Dawid Borycki, Patrycjusz Stremplewski, Kamil Liżewski, Slawomir Tomczewski, Paulina Niedźwiedziuk, Bartosz L Sikorski, and Maciej Wojtkowski. In vivo imaging of the human cornea with high-speed and high-resolution fourier-domain full-field optical coherence tomography. *Biomedical Optics Express*, 11(5):2849–2865, 2020.

[148] Kyrollos Yanny, Nick Antipa, William Liberti, Sam Dehaeck, Kristina Monakhova, Fanglin Linda Liu, Konlin Shen, Ren Ng, and Laura Waller. Miniscope3d: optimized single-shot miniature 3d fluorescence microscopy. *Light: Science & Applications*, 9(1):1–13, 2020.

[149] Jesse K Adams, Vivek Boominathan, Benjamin W Avants, Daniel G Vercosa, Fan Ye, Richard G Baraniuk, Jacob T Robinson, and Ashok Veeraraghavan. Single-frame 3d fluorescence microscopy with ultraminiature lensless flatscope. *Science advances*, 3(12):e1701548, 2017.

[150] Rishyashring R Iyer, Mantas Žurauskas, Qi Cui, Liang Gao, R Theodore Smith, and Stephen A Boppart. Full-field spectral-domain optical interferometry for snapshot three-dimensional microscopy. *Biomedical optics express*, 11(10):5903–5919, 2020.

[151] Ulugbek S Kamilov, Ioannis N Papadopoulos, Morteza H Shoreh, Alexandre Goy, Cedric Vonesch, Michael Unser, and Demetri Psaltis. Optical tomographic image reconstruction based on beam propagation and sparse regularization. *IEEE Transactions on Computational Imaging*, 2(1):59–70, 2016.

[152] JaeHwang Jung, Kyoohyun Kim, Jonghee Yoon, and YongKeun Park. Hyperspectral optical diffraction tomography. *Optics express*, 24(3):2006–2012, 2016.

[153] Yann LeCun, Yoshua Bengio, and Geoffrey Hinton. Deep learning. *nature*, 521(7553):436–444, 2015.

[154] George Barbastathis, Aydogan Ozcan, and Guohai Situ. On the use of deep learning for computational imaging. *Optica*, 6(8):921–943, 2019.

[155] Hongda Wang, Yair Rivenson, Yiyin Jin, Zhensong Wei, Ronald Gao, Harun Günaydın, Laurent A Bentolila, Comert Kural, and Aydogan Ozcan. Deep learning enables cross-modality super-resolution in fluorescence microscopy. *Nature methods*, 16(1):103–110, 2019.

[156] Yichen Wu, Yair Rivenson, Hongda Wang, Yilin Luo, Eyal Ben-David, Laurent A Bentolila, Christian Pritz, and Aydogan Ozcan. Three-dimensional virtual refocusing of fluorescence microscopy images using deep learning. *Nature methods*, 16(12):1323–1331, 2019.

[157] Yunzhe Li, Yujia Xue, and Lei Tian. Deep speckle correlation: a deep learning approach toward scalable imaging through scattering media. *Optica*, 5(10):1181–1190, 2018.

[158] Olaf Ronneberger, Philipp Fischer, and Thomas Brox. U-net: Convolutional networks for biomedical image segmentation. In *International Conference on Medical image computing and computer-assisted intervention*, pages 234–241. Springer, 2015.

[159] Kaiming He, Xiangyu Zhang, Shaoqing Ren, and Jian Sun. Deep residual learning for image recognition. In *Proceedings of the IEEE conference on computer vision and pattern recognition*, pages 770–778, 2016.

[160] Alexandre Goy, Kwabena Arthur, Shuai Li, and George Barbastathis. Low photon count phase retrieval using deep learning. *Physical review letters*, 121(24):243902, 2018.

[161] Shuai Li and George Barbastathis. Spectral pre-modulation of training examples enhances the spatial resolution of the phase extraction neural network (phenn). *Optics express*, 26(22):29340–29352, 2018.

[162] Mo Deng, Shuai Li, Alexandre Goy, Iksung Kang, and George Barbastathis. Learning to synthesize: Robust phase retrieval at low photon counts. *Light: Science & Applications*, 9(1):1–16, 2020.

[163] Shuai Li, Mo Deng, Justin Lee, Ayan Sinha, and George Barbastathis. Imaging through glass diffusers using densely connected convolutional networks. *Optica*, 5(7):803–813, 2018.

[164] Han Sang Park, Will J Eldridge, Wen-Hsuan Yang, Michael Crose, Silvia Ceballos, John D Roback, Jen-Tsan Ashley Chi, and Adam Wax. Quantitative phase imaging of erythrocytes under microfluidic constriction in a high refractive index medium reveals water content changes. *Microsystems & nanoengineering*, 5(1):1–9, 2019.

[165] Han Sang Park, Silvia Ceballos, Will J Eldridge, and Adam Wax. Invited article: Digital refocusing in quantitative phase imaging for flowing red blood cells. *APL photonics*, 3(11):110802, 2018.

[166] Heejin Choi, Dushan N Wadduwage, Ting Yuan Tu, Paul Matsudaira, and Peter TC So. Three-dimensional image cytometer based on widefield structured light microscopy and high-speed remote depth scanning. *Cytometry Part A*, 87(1):49–60, 2015.

[167] Sinno Jialin Pan and Qiang Yang. A survey on transfer learning. *IEEE Transactions on knowledge and data engineering*, 22(10):1345–1359, 2009.